Solution-Processed Two-Dimensional Materials for Organic Optoelectronics

Kumulative Dissertation

zur Erlangang des Grades

„Doktor der Naturwissenschaften“

im Fachbereich Chemie, Pharmazie, und Geowissenschaften der

Johannes Gutenberg-Universität Mainz und in Kooperation mit dem

Max-Planck-Institut für Polymerforschung Mainz

vorgelegt von

Antonio Gaetano Ricciardulli

geboren in Atripalda / Italien

Mainz, 2018

Dekan: [redacted]

1. Berichterstatter: [redacted]

2. Berichterstatter: [redacted]

Tag der mündlichen Prüfung: 19.11.2018

Die vorliegende Arbeit wurde in der Zeit von April 2015 bis November 2018 im Max-Planck-Institut für Polymerforschung in Mainz unter der Betreuung von Prof. Dr. [redacted] durchgeführt.

Table of Contents

Chapter 1 Introduction

The last decades have witnessed an unprecedented increase of technological progress in the field of optoelectronics. The constant demand of higher performances, sustainability and latest requirements of the consumer market led to the research of novel strategies. Understanding the structure-to-properties relationships of the materials and the device architecture engineering have been crucial in the development of optoelectronic devices.

1.1 Organic semiconductors

Organic semiconductors combine the electronic behavior of semiconductors, such as electrical conductivity, absorption and emission of light, with the ease of processing and chemical tunability of either conjugated small molecules or polymers. This class of materials has attracted an increasing attention since the first reported electrical conductivity in halogen doped polyacetilene in 1977.[1] Until now, the field of organic electronics has witnessed a constant rise of the materials performances, due to the improvement of the material design and physical understanding (Figure 1.1).[2] In particular, organic optoelectronic applications like organic solar cells (OSCs) and light emitting diodes (OLEDs) have experienced a rapid growth, still on going, which has led to commercialization.[3] The success of these devices mainly relies on the combination of high performances, materials abundancy, cost-effectiveness and ease of manufacturing.

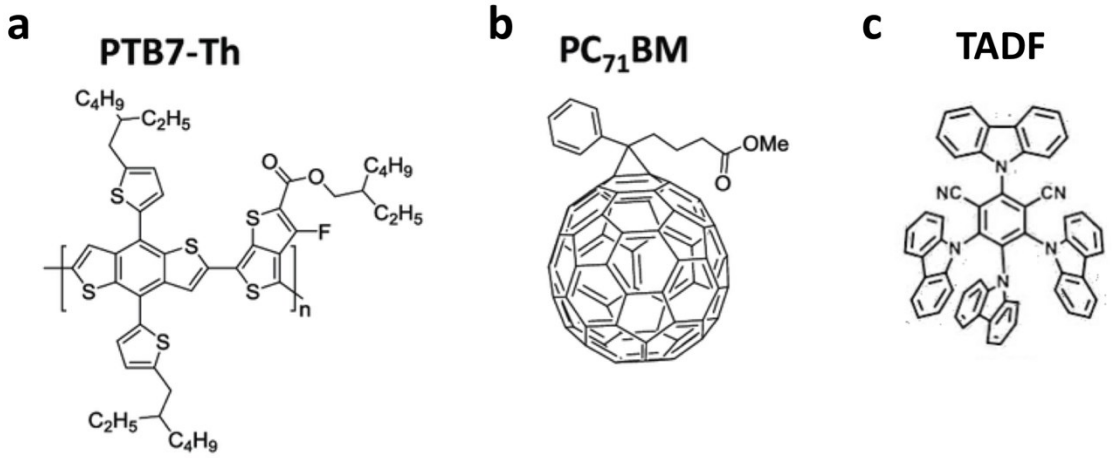

Figure 1.1 Examples of organic semiconducting materials used in the latest high-performance organic optoelectronic devices. (a) Donor and (b) acceptor in typical organic solar cell. (c) Emissive layer in organic light-emitting diode.[4]

1.2 Organic solar cells

Solar, the largest renewable energy resource, has the capability to meet the growing global energy demand, which nowadays mainly rely on fossil fuel energy reserves.[5] Currently, the most efficient and commercialized photovoltaic modules are based on inorganic materials such as silicon.[6] However, processing and cost of pure crystalline inorganic materials triggered an extensive research towards alternative solar cells. In contrast, organic photovoltaics (OPV) represent an attractive emerging technology, due to the low-cost and wide selection of the materials used in its modules. Moreover, OSCs allow compatibility with printing techniques and fabrication of semi-transparent flexible devices. Nevertheless, the actual OSCs market is hindered by power conversion efficiencies (PCE) lower than inorganic counterparts and lifetime limitations. In contrast, perovskites are low-cost, solution-processable alternatives which outperform organic active layers in solar cells.[7] However, due to stability concerns and the presence of lead,[8] researchers are still devoting many efforts to obtain stable and highly efficient OPV devices.[9] Recently, after stationary years (Figure 1.2), promising results have been achieved (PCE > 17%)[10] by molecular optimization, which makes OSCs commercialization very promising in the near future.

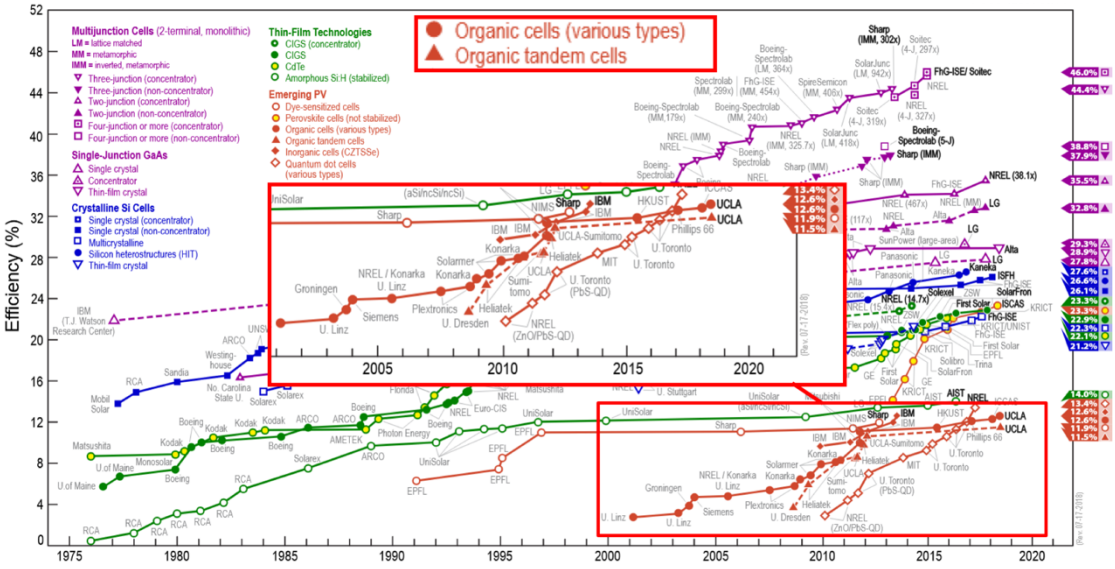

Figure 1.2 Recent progress in the organic photovoltaic field.[11]

OSCs have a vertical architecture where the active layer is sandwiched between two electrodes. The typical setup is showed in Figure 1.3. The most common transparent electrode for OSCs is indium tin oxide (ITO), deposited on a transparent substrate (quartz or flexible polymer) which allow light transmission. The metal electrode, such as aluminum, gold and silver, is generally evaporated on top of the active layer. The choice of the electrodes is based on the energy level alignment with the active layer. To optimize the charge transport, interfacial layers are often required.

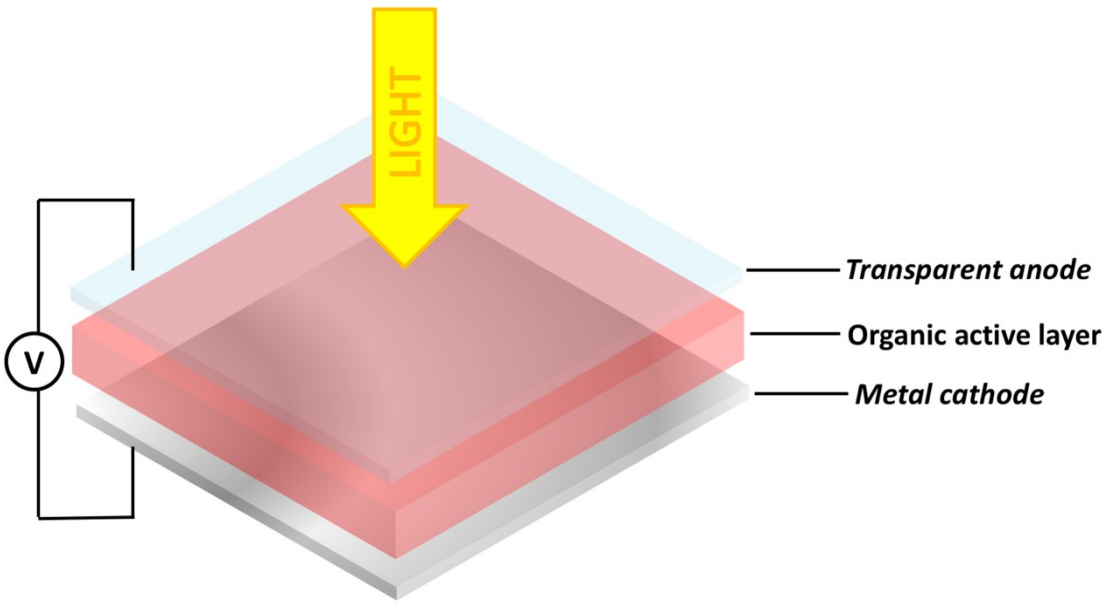

Figure 1.3 Typical setup of an OSC. The device consists of an organic layer sandwiched between a transparent anode and a metal cathode.

In bulk heterojunction (BHJ) OSC, a kind of solar cells, the active layer constitutes of intimately blended electron donating and accepting materials (Figure 1.4). This morphology is ideal for electron and hole extraction. First, the photons are absorbed either in the donor or acceptor domain. The photon then generates a tightly bound exciton (Frenkel exciton), which diffuses towards the donor-acceptor interface. In BHJ OSC, the exciton diffusion length typically amounts to a 5-10 nm, which limits the size of the donor and acceptor domains of the active layer. At the interface between donor and acceptor, charge transfer occurs and a charge-transfer (CT) exciton is formed. Subsequently, the CT exciton dissociates and the resulting free carriers, electrons and holes, can move to the electrodes, where they can be extracted. Next to charge carrier extraction also loss processes as recombination of charge-transfer excitons or electrons and holes can take place.

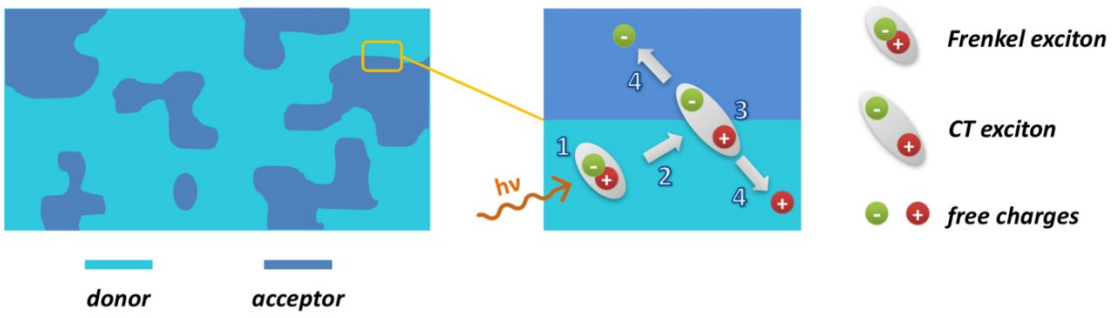

Figure 1.4 Schematic illustration of photocurrent generation mechanism in BHJ OSCs. (1) Exciton generation upon illumination is followed by (2) diffusion of exciton at the interface, where CT exciton is formed (3). Free charges are extracted (4) after successful dissociation of CT exciton.

To evaluate the performance of an OSC, a voltage is swept from negative to positive values (-1 V to +1 V) in the dark and under illumination. A current density-voltage (*J-V*) characteristic is obtained from this measurement (Figure 1.5), which provides the parameters to determine the efficiency of a solar cell, the power conversion efficiency (PCE). PCE is defined as:

$$PCE = \frac{P_{Max}}{P_{in}} = \frac{FF \times V_{OC} \times J_{SC}}{P_{in}} \qquad (1.1)$$

Where P_{in} is the incident light intensity and P_{Max} is the electrical power generated by the solar cell at the maximum power point, which is described by the product of the open circuit voltage V_{oc}, short circuit current J_{sc} and fill factor *FF*.

V_{oc} is the voltage at which the current is zero, whereas J_{sc} is the current through the solar cell at zero applied voltage. *FF* is the ideality factor, which represents the fraction of the product of V_{oc} and J_{sc} that is used to generate power, and is defined as:

$$FF = \frac{P_{Max}}{V_{OC} \times J_{SC}} \qquad (1.2)$$

The *J-V* measurements, to determine the PCE of a solar cell, are carried out under air mass 1.5 global (AM 1.5G) illumination. AM 1.5G corresponds to the solar spectrum

obtained by sunlight with an angle of incidence of 48.19°, which is the yearly average for the 48 contiguous U.S. states.[12]

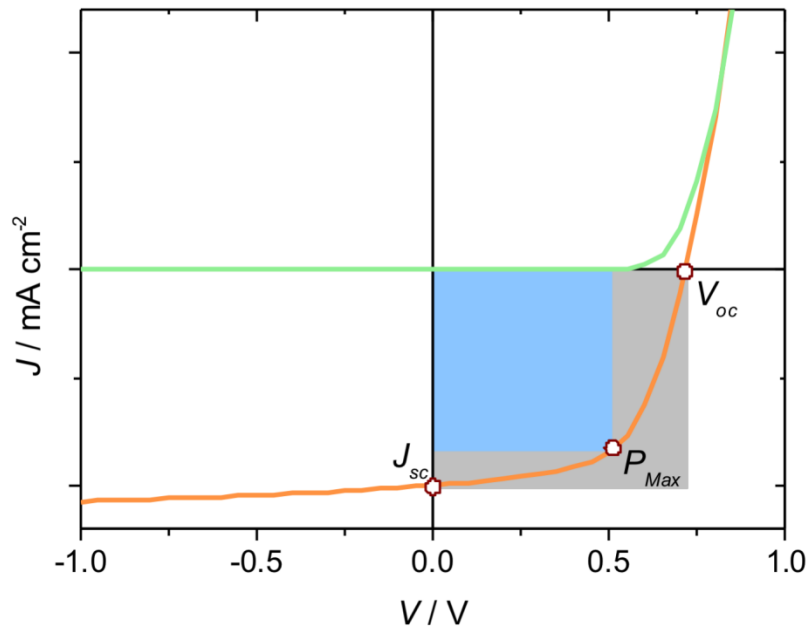

Figure 1.5 Typical *J-V* characteristic of a solar cell. The green line is the dark current, the orange plot is the measured current under illumination. Typical solar cells parameters, such as J_{sc}, V_{oc} and P_{Max}, are illustrated. *FF* is the fraction of the blue and grey areas defined by $J_{sc} \cdot V_{oc}$ and P_{Max}, respectively.

1.3 Organic light-emitting diodes

Since the invention of the cathode ray tube (CRT) by Karl Ferdinand Braun in 1887,[13] display technology has witnessed massive development. Light-emitting diodes (LEDs), semiconductor devices that emit lights upon application of a voltage, entered the display market in the 1970s. Among LEDs, organic materials based devices show superior features like light weight, low power consumption, high brightness and full-color capability.[14] Three decades after the first LEDs industrial applications, Sony introduced the first OLED TV (Sony XEL-1). Nowadays, OLED panels are widely used in different consumer devices, such as televisions and smartphones. Recently, IDTechEx forecast that

the OLED market, which was valued USD 16 billion, is expected to reach USD 48.81 Billion by 2023.[15]

OLEDs, similarly to OSCs, consist of a vertical stack where the emissive layer is sandwiched between two electrodes. To enhance charge injection into the organic emitting material, injection layers are often introduced between the electrodes and the emissive layer.[16] The typical architecture is showed in Figure 1.6.

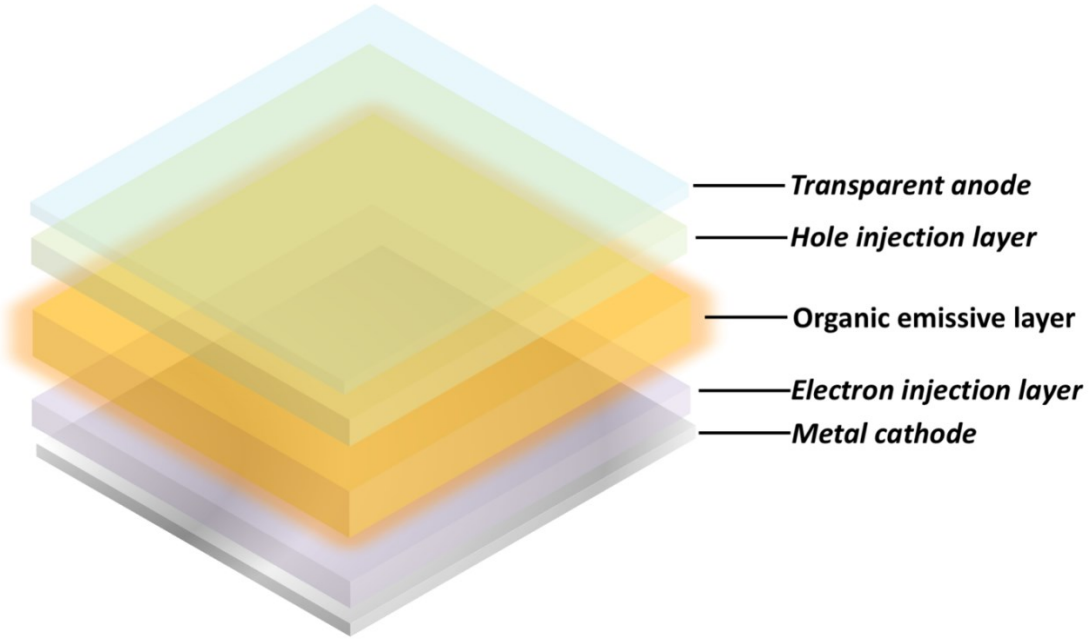

Figure 1.6 Typical setup of an OLED. The organic emitter is sandwiched between a transparent anode and a cathode. HIL and EIL can be implemented to enhance hole and electron injection into the emissive layer, respectively.

The operation of an OLED relies on three features, which are charge injection, charge transport and recombination, as shown in Figure 1.7. First, holes and electrons are injected from the electrodes into the organic semiconductors by applying voltages higher than the built-in voltage of the device. The built-in voltage (V_{bi}) is defined as the difference of the work functions of the anode (ϕ_a) and the cathode (ϕ_b), respectively:

$$V_{bi} = \frac{1}{e}(\phi_a - \phi_c) \qquad (1.2)$$

where *e* is the elementary charge.

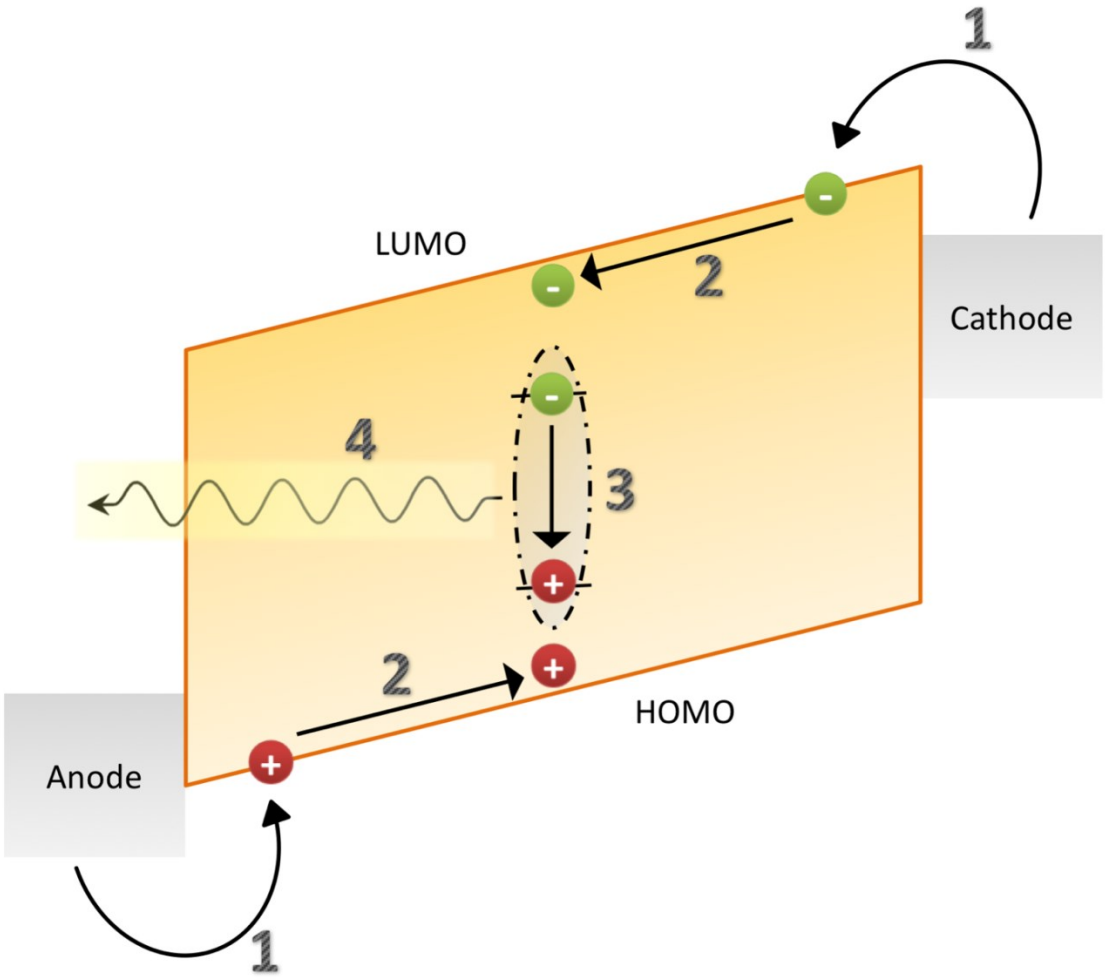

Figure 1.7 Schematic illustration of the operation of an OLED device. (1) Charge injection from the electrodes occurs upon the application of a voltage. (2) Holes and electrons are transported, respectively, towards the cathode and the anode due to the applied electric field. (3) When a hole and an electron meet they recombine to form an exciton, which decays (4) with subsequent emission of light.

Due to the applied electric field electrons and holes will drift to the opposite electrode. When the distance between a hole and an electron is close enough, they will be attracted by Coulomb interaction to form an exciton, a bound excited state between a hole and electron. Subsequently, the exciton decays radiatively to its ground state by emission of a photon for recombination of the charges. To have an efficient light emission, Ohmic

contacts have to be formed between the emissive layer and the two electrodes.[17] Therefore, the work function of the anode and cathode have to match the highest occupied molecular orbital (HOMO) and lowest unoccupied molecular orbital (LUMO) levels of the organic semiconductor, respectively. However, typical electrodes used in OLED devices, have work functions which lead to large injection barriers.[18] Hence, to ensure Ohmic contacts and facilitate carrier injection in case of high energy barrier, hole injection or electron injection layers (HIL or EIL) are introduced between the electrodes and the organic emitter (Figure 1.8).

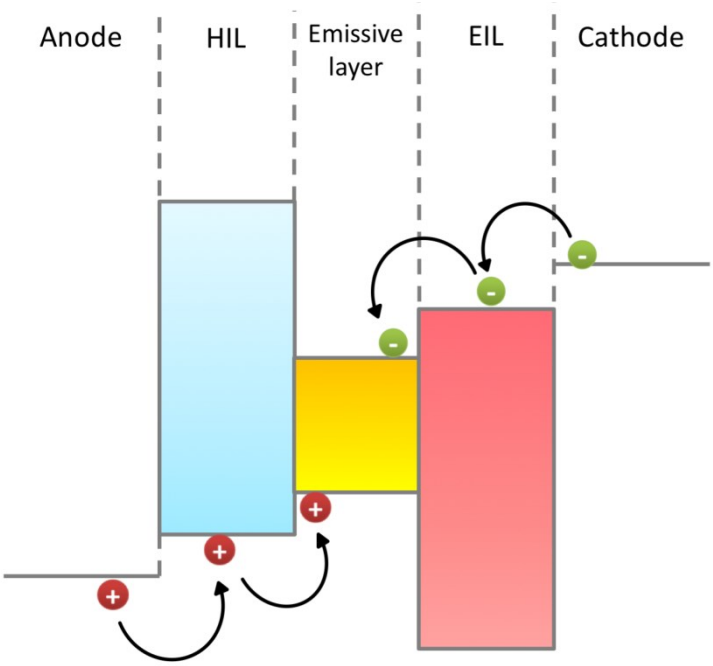

Figure 1.8 Energy band diagram of the components of a generic OLED. HIL and EIL are introduced into the device according to the energy band structure of the materials.

To evaluate the performance of OLEDs, external quantum efficiency (EQE) is mainly used. EQE is defined as the ratio between the number of emitted photons and amounted of injected carriers. In short, this parameter can be obtained from the *J-V* characteristics of an OLED, measured by sweeping the voltage from negative to positive values. Contrary to OSC, OLEDs are operated at higher voltages. The light output of the device is detected by a silicon photodiode.

1.3.1 Perovskite light-emitting diodes

Metal-halide perovskites,[19] with the general formula ABX_3 (A= organic or inorganic: $CH_3NH_3^+$, $CH(NH_2)_2^+$, etc. or Cs, Sb, etc.; B = Pb^{2+}, Sn^{2+}; X = Cl^-, Br^- or I^-), are emerging as attractive solution-processable semiconducting materials due to their remarkable optoelectronic properties, such as tunable bandgap,[20] long carrier diffusion lengths,[21] high absorption coefficients[22] and large hole and electron mobilities.[23] In addition to these features, high color purity[24] and high photoluminescence quantum yield[25] (PLQY) have contributed to the development of perovskite based LEDs. Moreover, the color emission of perovskites can be easily tuned from blue to green or red by simply changing the halide anion from Cl^- to Br^- or I^-, respectively.[26] The working principles and device structure of a LED using perovskite as emitting layer (PeLED) are similar to the ones of an OLED. Since their first examples, PeLEDs have rapidly reached EQE values as high as 14.4%.[27] Improvements have been achieved thanks to the progress of the perovskite synthetic routes with the formation of nanocrystals[28] and post-modification of perovskite film morphology, such as vapor annealing or cross-linking.[29] However, devices incorporating perovskite emitters with deep valence band (VB), as low as 5.6 eV,[30] suffer from limited hole injection, which hinder their performances. Indeed, conventional HILs (i.e. poly(3,4-ethylenedioxythiophene) polystyrene sulfonate, also known as PEDOT:PSS) used in PeLEDs typically have a work function of 5.0 eV, leading to large hole injection barriers with most of the perovskites. Therefore, research on alternative HILs or devices architectures is currently growing.[31] This topic will be further addressed in Chapter 4.

1.4 Transparent Conductive Electrodes

Transparent conductive electrodes (TCEs) are optically transparent and electrically conductive materials used in optoelectronics. This class of materials exhibits high optical transmission in the visible range, which requires large energy gaps (> 3.3 eV), and typical electrical conductivities higher than 10^3 S cm^{-1}.[32]

1.4.1 Indium Tin Oxide

The most widely used TCE for applications like OSCs and OLEDs is indium tin oxide (ITO). For commercial purposes, ITO is mainly fabricated by magnetron sputtering,[33] spray-pyrolysis[34] and sol-gel methods.[35] The success of this n-type material with large band gap (> 3.5 eV) relies on its high optical transmittance (> 90%) and conductivity (10^4 S cm^{-1}).[36] However, despite its outstanding features, which makes it the elite material up-to-date, the use of ITO as TCE in organic optoelectronics has several drawbacks.

First, indium (In) is a rare metal mainly obtained as a by-product from the extraction of sulfidic zinc ores. In 2014, the price of In reached the value of 750 $ per kg.[37] Even though In price has undergone to a considerable reduction recently,[38] its cost has always been dwindling during the past years.[37] Hence, the use of ITO in organic optoelectronics, which rely on low cost to hit the market, is critical. Second, the price for ITO is further increased by the deposition techniques on substrates. Indeed, the ITO transparent anode constitutes about 30% of the fabrication cost in a solar cell.[39] Third, physical vapor deposition techniques for high-quality ITO limit its applications in light-weight optoelectronic devices built on plastics. For instance, magnetron sputtering requires temperatures higher than 200 - 300 ˚C to output an optimal defect-free polycrystalline microstructure, which are incompatible with the use of plastic substrates such as poly(ethylene terephthalate) (upper temperature of processing of 150 ˚C).[40] In contrast, low-temperature deposition techniques typically lead to amorphous films with poor conductivity and transmittance.[41] In addition to these constraints, ITO is affected by mechanical instability.[42] ITO is a brittle oxide that cracks under mechanical stress,[43] preventing its use in devices which requires bendability and flexibility.

A recent report on the current status and perspective of transparent conductive films from IDTechEx[44] stated that even though ITO is still the most commonly used material as TCE, alternative materials, like silver nanowires (AgNWs) and metal meshes, are entering the market and their use will rapidly grow in the following years.

1.4.2 One-dimensional Materials

One-dimensional (1D) materials, like metal nanowires and carbon nanotubes, have recently emerged as potential candidates for TCEs, with transmittances greater than 80% and sheet resistances (R_s) less than 20 Ω sq^{-1}.[45] Despite promising optical and electrical properties, metal NWs films exhibit several drawbacks. For instance, 1) percolation of charges through junctions between the nanowires results in large contact resistance.[46] 2) The stacking of NWs contributes to high surface roughness,[47] which is a severe problem for applications as organic light-emitting diodes (LEDs) with an active layer thickness of only 100 nm or less. Nanowires sticking out of the electrodes penetrate through the active layer leading to electrical shorts. 3) The vacancies within the NW networks increase the series resistance that severely limits the current through stacked devices, like LEDs and solar cells. Although many strategies, such as thermal annealing,[48] high-force pressing[49] and welding techniques by different light sources (i.e. laser, flash lamps)[50], have been explored, it has been proven difficult to fully overcome the intrinsic limitations of metal NWs. Successful approaches have used composites of polymers and AgNWs. By integrating the NWs in a (conductive) polymer matrix, solar cells[51] and light-emitting diodes[52] were realized with performance matching those of the ITO based counterparts.

1.4.3 Two-dimensional materials

Two-dimensional (2D) materials are defined as substances with few or less nanometers (nm) in which both atomic organization and bond strength along a two-dimensional plane are stronger than along a third dimension.[53] Because of their unprecedented physical properties and high surface area, 2D materials are implemented in a wide range of applications, including catalysts,[54] batteries,[55] supercapacitors,[56] sensors[57] and optoelectronics.[58] 2D materials have recently emerged as novel elements for optoelectronic devices due to their exceptional and diverse optical and electrical properties. Among the large number of applications, highly conductive and transparent

graphene is used as transparent electrode in OSCs and OLEDs.[58-59] Graphene, a sp^2-hybridized carbon arranged in a honeycomb lattice, is the major representative of this class of materials.[60] Graphene exhibits remarkable properties, such as high transmittance (97.7%)[61] and high intrinsic carrier mobility (2 x 10^5 cm^2 V^{-1} s^{-1}),[62] large thermal conductivity (> 5000 W m^{-1} K^{-1}),[63] high surface area (2630 m^2 g^{-1})[64] and a Young's modulus of approximately 1 TPa.[65] These features make graphene a suitable candidate for flexible TCEs.[58, 66] For example, OSCs based on graphene made from chemical vapor deposition (CVD) delivers efficiencies comparable to those based on ITO.[67] Indeed, CVD-graphene performs high transparency (> 90%) and low series resistance (R_s) (~ 20 Ω sq^{-1}).[39a] However, CVD is not readily scalable because of its high cost, complicated process and low yield. An alternative method to produce on a large scale is reduction of graphene oxide.[68] Nevertheless, the high density of defects in reduced graphene oxide (rGO) results in poor electrical properties, and the use of harsh conditions in the graphite oxidation step makes it not the best choice for commercial production of graphene-based optoelectronic devices. Typically, rGO TCEs has high R_s in the order of 10^2-10^3 Ω sq^{-1},[69] which hamper their application in the field of commercial transparent conductors.

1.5 Synthesis of 2D materials for optoelectronic applications

Chemical and physical properties of 2D materials strongly rely on their structure. Hence, synthetic routes are critical for their characteristics.

To integrate 2D materials into organic optoelectronic devices, which rely on low cost to be competitive in the marketplace, high quality should be coupled with cost effectiveness. Thus, the choice of the 2D material synthesis plays an essential role. CVD and liquid-phase sonication are widely used techniques for production of 2D materials for optoelectronics. However, despite the extremely high quality of the materials produced by CVD, the troublesome transfer process and high operation costs hinder their real application.[66b, 70] In contrast, liquid sonication is a simple solution-processed technique with potential scalability. Unfortunately, the exfoliated products have poor thickness uniformity and moderate electronic properties.[71] Alternatively, electrochemical exfoliation of bulk layered materials is a cost-effective technique for production of 2D

materials with excellent purity and electrical properties.[72] Graphene exfoliated with this method has a high yield of thin layers (85% of 1-3 layers), high hole mobility (> 400 cm^2 V^{-1} s^{-1}) and superior solution-processability.[73] Bulk black phosphorus (BP) can be exfoliated into thin-layered BP with yield up to 78%, which exhibits high hole mobility (> 250 cm^2 V^{-1} s^{-1}).[74] First examples of electrochemically exfoliated 2D materials used in optoelectronics are shown in the following chapters of this thesis.

1.6 Thin film deposition methods for solution-processable 2D materials

Vacuum deposition is commonly used in semiconductor industry for coatings. Despite high film uniformity, stable reproducibility and possibility to perform multi-layer deposition, vacuum methods suffer from high setup costs and large material consumption.

In contrast, solution-processing methods offer several advantages like low-cost manufacturing, compatibility with flexible substrates, reduced material waste and high versatility. However, to ensure a correct film formation, it is important to choose the best strategy according to the characteristics of the material and solvent used. Some of the most common techniques will be discussed in the following paragraphs.

1.6.1 Spin-coating

Spin-coating is a quick, easy and low-cost technique to form thin films on top of substrates (Figure 1.9). An amount of the desired material, dispersed in the proper solvent, is casted on the substrate, which is then rotated at high speed. During rotation, the centripetal force spreads the liquid coating over the substrate. Ideally, upon evaporation of the solvent, the material forms an even covering on the substrate. The film thickness can be adjusted by changing dispersion concentration, rotation speed and time. Despite its advantages, spin-coating is limited to small area substrates. Moreover, the most of the dispersion is generally wasted during the rotation step.

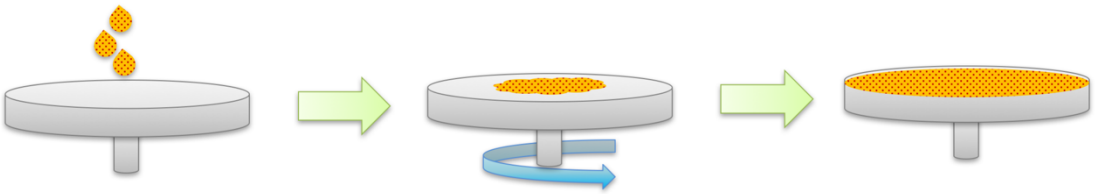

1.9 Schematic illustration of spin-coating process.

1.6.2 Drop-casting

Drop-casting is a coating method that yields films by dispensing the dispersion of a material on top of a substrate (Figure 1.10). As for spin-coating, the film is formed after evaporation of the solvent. The thickness of the film can be tuned by varying the concentration of the dispersion. Despite the ease of processing, the coating is usually uneven with a typical coffee-ring effect.

1.10 Schematic illustration of drop-casting technique for film formation.

1.6.3 Dip-coating

Deposition of a film obtained by immersion and withdrawal of a substrate into a dispersion is generally indicated as dip-coating (Figure 1.11). The coating thickness is controlled by the withdrawal speed, concentration of the dispersion, viscosity and boiling point of the solvent. Dip-coating is a cheap and simple method with no waste of raw material. However, double-side coating of bare substrates is unavoidable and uniform film formation restricted to viscous dispersions.

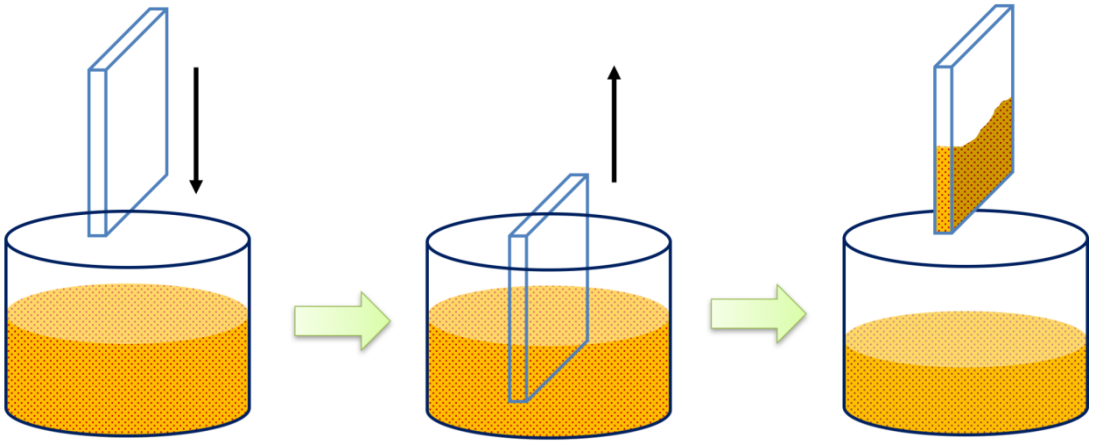

1.11 Schematic illustration of dip-coating process.

1.6.4 Suction Filtration

Materials dispersed in solvents can be filtered through either a hydrophobic or hydrophilic membrane, according to the nature of the solvent, by suction filtration, which leads to formation of a film on top of the membrane (Figure 1.12). The thickness of the film is tunable on the basis of the volume/concentration of the dispersion. Afterwards, the film is transferred onto the substrate by a mechanical press. This method requires a precise control of the membrane removal to avoid uneven coating in ultra-thin films.

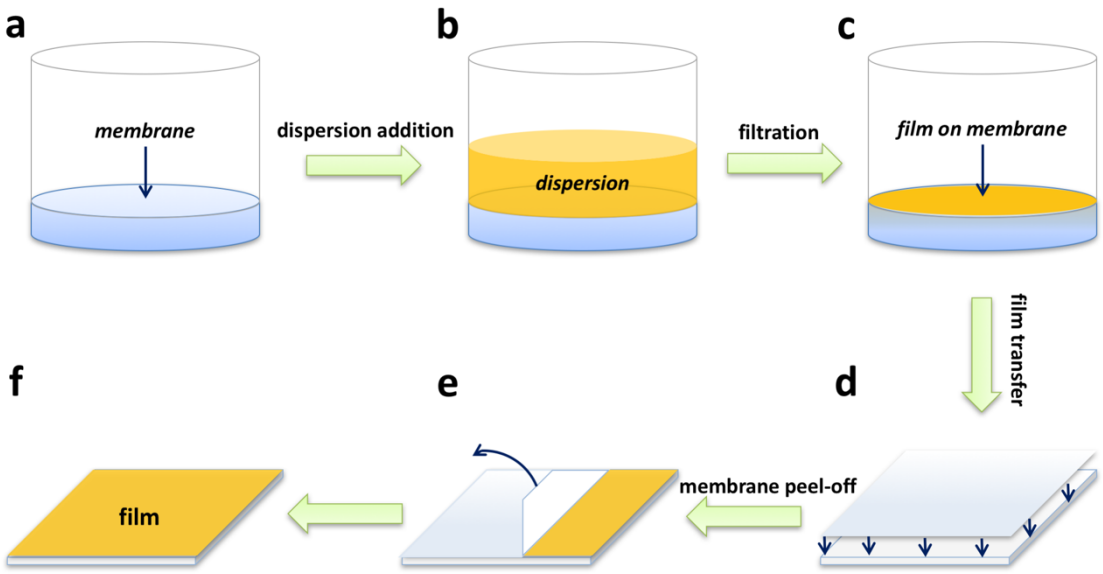

Figure 1.12 Schematic illustration of the fabrication of a generic film. The fabrication process includes a) addition of the dispersion on the top of a membrane, b) vacuum-assisted filtration c) formation of film onto the membrane, d) film transfer on top of the substrate, e) membrane removal and f) film transfer from the membrane to the substrate.

1.6.5 Spray-coating

Spray deposition of materials onto a wide selection of substrates is obtained by air-assisted guns (Figure 1.13). The dispersion is pushed out of the nozzle in the form of droplets by a carrier gas (i.e. nitrogen). Subsequently, the slow evaporation of the droplets on the substrates allows the formation of uniform coating. As for the other methods, film thickness is controlled by volume or concentration of the dispersion. Spray-coating is a scalable and versatile deposition technique. Indeed, films can be coated on large area substrates, both rigid and flexible, and the morphology controlled by pressure of the carrier gas.

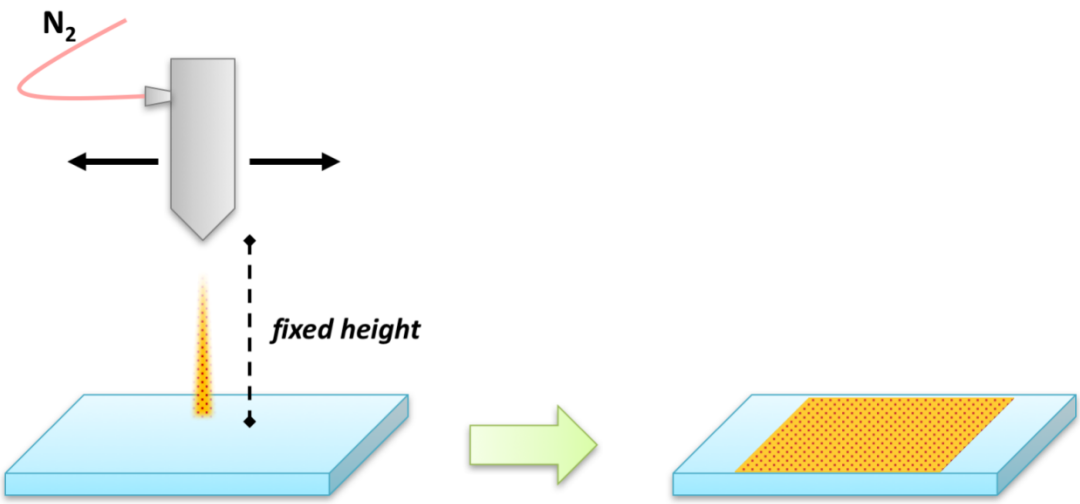

Figure 1.13 Schematic illustration of spray-coating.

1.7 Motivation and Objective

As illustrated in the previous paragraphs, the field of organic optoelectronic has drawn considerable attention in the recent decades. Cost effectiveness, abundancy of materials and ease of processing are just some of the advantages. Recently, highly performant organic devices like OLEDs have successfully entered the consumer market. Others, such as OSCs, although the initial lower performances compared to the inorganic counterparts, have recently undergone to a rapid ascent in terms of efficiency and stability, which give them the potential to be competitive.

Organic optoelectronic devices require a transparent electrode to allow absorption and emission of light, as for OSCs and OLEDs, respectively. This electrode necessitates having high transmittance, low series resistance and, for the latest commercial needs, high degree of flexibility. ITO is the most commonly used TCE in organic optoelectronics because of its outstanding performances. However, it presents many drawbacks such as high production cost, scarce reserves of Indium and poor chemical/mechanical stability.[75] Therefore, seeking for an efficient alternative to ITO as TCE is of great significance. Despite different alternatives for ITO replacement have been investigated so far,[39a, 45a, 69, 76] a material able to embrace all the requests for a cost effective TCE is still missing.

In this thesis, solution-processable alternatives to ITO are discussed in Chapter 2 and Chapter 3. In Chapter 2, the use of electrochemical exfoliated graphene (EG) as TCE in OSCs has been reported. This approach enables solution-processable graphene flakes with high yield (75%), remarkable electronic properties (hole mobility of 405 $cm^2\ V^{-1}\ s^{-1}$), low defect density (I_D/I_G ratio < 0.1 in Raman spectra) and C/O ratio of 21.2.[73] Electrochemical exfoliated graphene (EG) has been successfully integrated in batteries and supercapacitors, which exhibit higher performances than other solution-processed graphene.[77] Despite this, fabrication of uniform and continuous EG films combined with low R_s, high transmittance and low surface roughness is the main challenge for the application of EG-based transparent electrodes in optoelectronic devices. Transparent film composed of thin EG sheets (90% of 1-3 layers thick) have been fabricated by spray-coating. EG transparent films display R_s as low as 0.18 $k\Omega\ sq^{-1}$ at transmittance of 55 % and low surface roughness (2.86 nm). Moreover, EG TCEs coated on flexible substrates (polyethylene naphthalate, PEN) are mechanically stable. To evaluate the performance of EG as TCE for organic optoelectronics, BHJ OCs using poly[[4,8-bis[(2-ethylhexyl)oxy]benzo[1,2-b:4,5-b']dithiophene-2,6-diyl] [3-fluoro-2-[(2-ethylhexy)carbonyl]thieno[3,4-*b*]thiophenediyl]] (PTB7) and $PC_{71}BM$ as donor and acceptor, respectively, have been fabricated. Despite the highest reported PCE value among up-to-date OSCs with solution-processed graphene as TCE, our devices exhibit PCE typically 40% lower than their ITO-based analogues. The reason of this huge gap is ascribed to the trade-off between transmittance and R_s of EG. To obtain lower R_s values, the thickness of EG film has to be increased. This leads to lower film transparency with consequent reduced photons absorption.

Hence, in order to enhance performances of the devices, keeping a feasible approach, the combination of other solution-processed highly conductive materials with EG is a rational strategy. Following this pathway, in Chapter 3, we present a mixed-dimensional (1D-2D) structure using silver NWs (AgNWs) and EG as components. Spray-coating of large area EG allows a complete coverage of the underlying AgNW-network. As result, hybrid AgNWs-EG TCEs, compared with pristine AgNWs, exhibit a decrease of R_s from 78 to 13.7 $\Omega\ sq^{-1}$ (optical transparency of 89%) and the surface roughness is reduced from 16.4 to 4.6 nm. Moreover their mechanical and chemical stability is enhanced. When used as a bottom electrode in OSCs and polymer LEDs (PLEDs), the devices exhibit a power

conversion efficiency of 6.6% and an external quantum efficiency of 4.4%, respectively, comparable to their commercial ITO-based counterparts.

In addition to organic semiconductors, other materials are emerging in the optoelectronic field. Perovskite is an important class of materials in photovoltaic devices because of their astounding optoelectronic properties.[78] Perovskite SCs have witnessed a rapid progress in terms of efficiency in the past few years, approaching nowadays values that match the performance of industry-standard silicon.[11] Recently, perovskite materials have been used as emitting layers in LEDs due to advantages such as high charge-carrier mobility, high color purity, color tunability, and low material costs.[79] However, the light-output and efficiency of PeLEDs is limited by hole injection and high leakage current, generated by a high hole injection barrier and poor perovskite morphology, respectively. In Chapter 4, we report a feasible strategy to overcome both constraints by introducing a 2D material, black phosphorus, as hole injection layer in the PeLED stack. A continuous film made of high-quality, ultra-thin and large BP sheets on top of PEDOT:PSS simultaneously enhances the hole injection and morphology of the green-emitting inorganic $CsPbBr_3$ perovskite. Inclusion of BP significantly improves both the EQE, from 0.7% to 2.8%, and luminance, from 5000 to 20000 cd m^{-2}, of $CsPbBr_3$ based PeLEDs.

References

[1] C. K. Chiang, C. R. Fincher, Y. W. Park, A. J. Heeger, H. Shirakawa, E. J. Louis, S. C. Gau, A. G. Macdiarmid, *Phys. Rev. Lett.* **1977**, 39, 1098.

[2] O. Ostroverkhova, *Chem. Rev.* **2016**, 116, 13279.

[3] a) C. H. Oh, H. J. Shin, W. J. Nam, B. C. Ahn, S. Y. Cha, S. D. Yeo, *SID symposium digest* **2013**, 4, 4; b) X. Z. Che, Y. X. Li, Y. Qu, S. R. Forrest, *Nat. Energy* **2018**, 3, 422.

[4] a) S. H. Liao, H. J. Jhuo, Y. S. Cheng, S. A. Chen, *Adv. Mater.* **2013**, 25, 4766; b) H. Uoyama, K. Goushi, K. Shizu, H. Nomura, C. Adachi, *Nature* **2012**, 492, 234.

[5] a) M. A. Perea-Moreno, Q. Hernandez-Escobedo, A. J. Perea-Moreno, *Energies* **2018**, 11, 19; b) IEA, *IEA Global Energy and CO2 Status Report* **2018**.

[6] a) M. A. Green, Y. Hishikawa, E. D. Dunlop, D. H. Levi, J. Hohl-Ebinger, A. W. Y. Ho-Baillie, *Prog. Photovoltaics* **2018**, 26, 427; b) K. Sopian, S. L. Cheow, S. H. Zaidi, in *4th International Conference on the Advancement of Materials and Nanotechnology*, Vol. 1877 (Eds: N. Kamarulzaman, M. S. Mastuli, R. Rusdi, N. Badar), Amer Inst Physics, Melville **2017**.

[7] Z. Li, T. R. Klein, D. H. Kim, M. J. Yang, J. J. Berry, M. van Hest, K. Zhu, *Nat. Rev. Mater.* **2018**, 3, 20.

[8] J. P. Correa-Baena, M. Saliba, T. Buonassisi, M. Gratzel, A. Abate, W. Tress, A. Hagfeldt, *Science* **2017**, 358, 739.

[9] J. Q. Zhang, L. Y. Zhu, Z. X. Wei, *Small Methods* **2017**, 1, 14.

[10] L. X. Meng, Y. M. Zhang, X. J. Wan, C. X. Li, X. Zhang, Y. B. Wang, X. Ke, Z. Xiao, L. M. Ding, R. X. Xia, H. L. Yip, Y. Cao, Y. S. Chen, *Science* **2018**, 361, 1094.

[11] *NREL Efficiency Chart Rev. 07-17-2018* **2018**

[12] *ASTM G159-98, Standard Tables for Reference Solar Spectral Irradiance at Air Mass 1.5: Direct Normal and Hemispherical for a 37 Degree Tilted Surface, ASTM International, West Conshohocken, PA, 1998* **2003**.

[13] K. F. Braun, *Annalen der Physik* **1987**, 60, 552

[14] B. Geffroy, P. Le Roy, C. Prat, *Polym. Int.* **2006**, 55, 572.

[15] *OLED Market by Display Application, Panel Type, Technology, Size, Material, Lighting Application, Panel Type & Vertical and Geography - Global Forecast to 2023* **2017**.

[16] a) G. A. H. Wetzelaer, A. Najafi, R. J. P. Kist, M. Kuik, P. W. M. Blom, *Appl. Phys. Lett.* **2013**, 102, 4; b) N. B. Kotadiya, H. Lu, A. Mondal, Y. Ie, D. Andrienko, P. W. M. Blom, G. Wetzelaer, *Nat. Mater.* **2018**, 17, 329.

[17] P. de Bruyn, A. H. P. van Rest, G. A. H. Wetzelaer, D. M. de Leeuw, P. W. M. Blom, *Phys. Rev. Lett.* **2013**, 111, 5.

[18] M. G. Helander, Z. B. Wang, J. Qiu, M. T. Greiner, D. P. Puzzo, Z. W. Liu, Z. H. Lu, *Science* **2011**, 332, 944.

[19] a) S. D. Stranks, H. J. Snaith, *Nat. Nanotechnol.* **2015**, 10, 391; b) J. Liang, C. Wang, Y. Wang, Z. Xu, Z. Lu, Y. Ma, H. Zhu, Y. Hu, C. Xiao, X. Yi, G. Zhu, H. Lv, L. Ma, T. Chen, Z. Tie, Z. Jin, J. Liu, *J. Am. Chem. Soc.* **2016**, 138, 15829.

[20] G. E. Eperon, S. D. Stranks, C. Menelaou, M. B. Johnston, L. M. Herz, H. J. Snaith, *Energy Environ. Sci.* **2014**, 7, 982.

[21] S. D. Stranks, G. E. Eperon, G. Grancini, C. Menelaou, M. J. P. Alcocer, T. Leijtens, L. M. Herz, A. Petrozza, H. J. Snaith, *Science* **2013**, 342, 341.

[22] S. De Wolf, J. Holovsky, S. J. Moon, P. Loper, B. Niesen, M. Ledinsky, F. J. Haug, J. H. Yum, C. Ballif, *J. Phys. Chem. Lett.* **2014**, 5, 1035.

[23] T. Leijtens, S. D. Stranks, G. E. Eperon, R. Lindblad, E. M. J. Johansson, I. J. McPherson, H. Rensmo, J. M. Ball, M. M. Lee, H. J. Snaith, *ACS Nano* **2014**, 8, 7147.

[24] Z. K. Tan, R. S. Moghaddam, M. L. Lai, P. Docampo, R. Higler, F. Deschler, M. Price, A. Sadhanala, L. M. Pazos, D. Credgington, F. Hanusch, T. Bein, H. J. Snaith, R. H. Friend, *Nat. Nanotechnol.* **2014**, 9, 687.

[25] J. W. Choi, H. C. Woo, X. Huang, W. G. Jung, B. J. Kim, S. W. Jeon, S. Y. Yim, J. S. Lee, C. L. Lee, *Nanoscale* **2018**, 10, 13356.

[26] Q. Le, H. W. Jang, S. Y. Kim, *Small Methods* **2018**, 0, 1700419.

[27] Y. T. Zou, M. Y. Ban, Y. G. Yang, S. Bai, C. Wu, Y. J. Han, T. Wu, Y. S. Tan, Q. Huang, X. Y. Gao, T. Song, Q. Zhang, B. Q. Sun, *ACS Appl. Mater. Interfaces* **2018**, 10, 24320.

[28] F. Yan, J. Xing, G. C. Xing, L. Quan, S. T. Tan, J. X. Zhao, R. Su, L. L. Zhang, S. Chen, Y. W. Zhao, A. Huan, E. H. Sargent, Q. H. Xiong, H. V. Demir, *Nano Lett.* **2018**, 18, 3157.

[29] C. Wu, Y. T. Zou, T. Wu, M. Y. Ban, V. Pecunia, Y. J. Han, Q. P. Liu, T. Song, S. Duhm, B. Q. Sun, *Adv. Funct. Mater.* **2017**, 27, 7.

[30] a) H. C. Cho, S. H. Jeong, M. H. Park, Y. H. Kim, C. Wolf, C. L. Lee, J. H. Heo, A. Sadhanala, N. Myoung, S. Yoo, S. H. Im, R. H. Friend, T. W. Lee, *Science* **2015**, 350, 1222; b) J. Xing, F. Yan, Y. W. Zhao, S. Chen, H. K. Yu, Q. Zhang, R. G. Zeng, H. V. Demir, X. W. Sun, A. Huan, Q. H. Xiong, *ACS Nano* **2016**, 10, 6623.

[31] a) L. Q. Zhang, X. L. Yang, Q. Jiang, P. Y. Wang, Z. G. Yin, X. W. Zhang, H. R. Tan, Y. Yang, M. Y. Wei, B. R. Sutherland, E. H. Sargent, J. B. You, *Nat. Commun.* **2017**, 8, 8; b) P. Z. Liu, W. Chen, W. G. Wang, B. Xu, D. Wu, J. J. Hao, W. Y. Cao, F. Fang, Y. Li, Y. Y. Zeng, R. K. Pan, S. M. Chen, W. Q. Cao, X. W. Sun, K. Wane, *Chem. Mater.* **2017**, 29, 5168.

[32] D. S. Ginley, C. Bright, *MRS Bull.* **2000**, 25, 15.

[33] T. Minami, H. Sonohara, T. Kakumu, S. Takata, *Thin Solid Films* **1995**, 270, 37.

[34] H. Bisht, H. T. Eun, A. Mehrtens, M. A. Aegerter, *Thin Solid Films* **1999**, 351, 109.

[35] L. L. Hench, J. K. West, *Chem. Rev.* **1990**, 90, 33.

[36] H. Kim, C. M. Gilmore, A. Pique, J. S. Horwitz, H. Mattoussi, H. Murata, Z. H. Kafafi, D. B. Chrisey, *J. Appl. Phys.* **1999**, 86, 6451.

[37] T. D. Kelly, G. R. Matos, *Historical Statistics for Mineral and Material Commodities in the United States, U.S. Geological Survey Data Series 140* **2014**.

[38] *Metal Bulletin's price assessment for Chinese domestic indium* **2017**.

[39] a) Y. Wang, S. W. Tong, X. F. Xu, B. Ozyilmaz, K. P. Loh, *Adv. Mater.* **2011**, 23, 1514; b) J. Kalowekamo, E. Baker, *Sol. Energy* **2009**, 83, 1224.

[40] *DuPont Teijin Films Data Sheets*.

[41] a) Y. Yang, Q. L. Huang, A. W. Metz, J. Ni, S. Jin, T. J. Marks, M. E. Madsen, A. DiVenere, S. T. Ho, *Adv. Mater.* **2004**, 16, 321; b) M. H. Ahn, E. S. Cho, S. J. Kwon, *Vacuum* **2014**, 101, 221.

[42] J. Lewis, *Mater. Today* **2006**, 9, 38.

[43] Z. Chen, B. Cotterell, W. Wang, E. Guenther, S. J. Chua, *Thin Solid Films* **2001**, 394, 201.

[44] K. Ghaffarzadeh, R. Das, *IDTechEX: Transparent Conductive Films and Materials 2018-2028: Forecasts, Technologies, Players* **2018**.

[45] a) J. Krantz, M. Richter, S. Spallek, E. Spiecker, C. J. Brabec, *Adv. Funct. Mater.* **2011**, 21, 4784; b) B. Sciacca, J. van de Groep, A. Polman, E. C. Garnett, *Adv. Mater.* **2016**, 28, 905.

[46] S. Han, S. Hong, J. Ham, J. Yeo, J. Lee, B. Kang, P. Lee, J. Kwon, S. S. Lee, M. Y. Yang, S. H. Ko, *Adv. Mater.* **2014**, 26, 5808.

[47] W. W. Xiong, H. L. Liu, Y. Z. Chen, M. L. Zheng, Y. Y. Zhao, X. B. Kong, Y. Wang, X. Q. Zhang, X. Y. Kong, P. F. Wang, L. Jiang, *Adv. Mater.* **2016**, 28, 7167.

[48] D. P. Langley, M. Lagrange, G. Giusti, C. Jimenez, Y. Brechet, N. D. Nguyen, D. Bellet, *Nanoscale* **2014**, 6, 13535.

[49] a) A. R. Madaria, A. Kumar, F. N. Ishikawa, C. W. Zhou, *Nano Res.* **2010**, 3, 564; b) T. Tokuno, M. Nogi, M. Karakawa, J. T. Jiu, T. T. Nge, Y. Aso, K. Suganuma, *Nano Res.* **2011**, 4, 1215.

[50] a) Q. Nian, M. Saei, Y. Xu, G. L. Sabyasachi, B. W. Deng, Y. P. Chen, G. J. Cheng, *ACS Nano* **2015**, 9, 10018; b) J. H. Park, G. T. Hwang, S. Kim, J. Seo, H. J. Park, K. Yu, T. S. Kim, K. J. Lee, *Adv. Mater.* **2017**, 29.

[51] W. Gaynor, G. F. Burkhard, M. D. McGehee, P. Peumans, *Adv. Mater.* **2011**, 23, 2905.

[52] L. Li, Z. B. Yu, W. L. Hu, C. H. Chang, Q. Chen, Q. B. Pei, *Adv. Mater.* **2011**, 23, 5563.

[53] S. Z. Butler, S. M. Hollen, L. Y. Cao, Y. Cui, J. A. Gupta, H. R. Gutierrez, T. F. Heinz, S. S. Hong, J. X. Huang, A. F. Ismach, E. Johnston-Halperin, M. Kuno, V. V. Plashnitsa, R. D. Robinson, R. S. Ruoff, S. Salahuddin, J. Shan, L. Shi, M. G. Spencer, M. Terrones, W. Windl, J. E. Goldberger, *ACS Nano* **2013**, 7, 2898.

[54] D. H. Deng, K. S. Novoselov, Q. Fu, N. F. Zheng, Z. Q. Tian, X. H. Bao, *Nat. Nanotechnol.* **2016**, 11, 218.

[55] K. S. Chen, I. Balla, N. S. Luu, M. C. Hersam, *ACS Energy Lett.* **2017**, 2, 2026.

[56] X. Peng, L. L. Peng, C. Z. Wu, Y. Xie, *Chem. Soc. Rev.* **2014**, 43, 3303.

[57] a) C. Anichini, W. Czepa, D. Pakulski, A. Aliprandi, A. Ciesielski, P. Samori, *Chem. Soc. Rev.* **2018**, 47, 4860; b) Y. S. Rim, S. H. Bae, H. J. Chen, N. De Marco, Y. Yang, *Adv. Mater.* **2016**, 28, 4415.

[58] K. P. Loh, S. W. Tong, J. S. Wu, *J. Am. Chem. Soc.* **2016**, 138, 1095.

[59] a) Z. K. Liu, J. H. Li, F. Yan, *Adv. Mater.* **2013**, 25, 4296; b) J. B. Wu, M. Agrawal, H. A. Becerril, Z. N. Bao, Z. F. Liu, Y. S. Chen, P. Peumans, *ACS Nano* **2010**, 4, 43.

[60] A. K. Geim, K. S. Novoselov, *Nat. Mater.* **2007**, 6, 183.

[61] K. S. Novoselov, V. I. Fal'ko, L. Colombo, P. R. Gellert, M. G. Schwab, K. Kim, *Nature* **2012**, 490, 192.

[62] J. H. Chen, C. Jang, S. D. Xiao, M. Ishigami, M. S. Fuhrer, *Nat. Nanotechnol.* **2008**, 3, 206.

[63] A. A. Balandin, S. Ghosh, W. Z. Bao, I. Calizo, D. Teweldebrhan, F. Miao, C. N. Lau, *Nano Lett.* **2008**, 8, 902.

[64] M. D. Stoller, S. J. Park, Y. W. Zhu, J. H. An, R. S. Ruoff, *Nano Lett.* **2008**, 8, 3498.

[65] C. Lee, X. D. Wei, J. W. Kysar, J. Hone, *Science* **2008**, 321, 385.

[66] a) K. S. Kim, Y. Zhao, H. Jang, S. Y. Lee, J. M. Kim, K. S. Kim, J. H. Ahn, P. Kim, J. Y. Choi, B. H. Hong, *Nature* **2009**, 457, 706; b) S. Bae, H. Kim, Y. Lee, X. Xu, J.-S. Park, Y. Zheng, J. Balakrishnan, T. Lei, H. R. Kim, Y. I. Song, Y.-J. Kim, K. S. Kim, B. Özyilmaz, J.-H. Ahn, B. H. Hong, S. Iijima, *Nat. Nanotechnol.* **2010**, 5, 574; c) Z. Y. Yin, J. X. Zhu, Q. Y. He, X. H. Cao, C. L. Tan, H. Y. Chen, Q. Y. Yan, H. Zhang, *Adv. Energy Mater.* **2014**, 4, 19.

[67] H. Park, S. Chang, X. Zhou, J. Kong, T. Palacios, S. Gradecak, *Nano Lett.* **2014**, 14, 5148.

[68] C. K. Chua, M. Pumera, *Chem. Soc. Rev.* **2014**, 43, 291.

[69] D. Konios, C. Petridis, G. Kakavelakis, M. Sygletou, K. Savva, E. Stratakis, E. Kymakis, *Adv. Funct. Mater.* **2015**, 25, 2213.

[70] T. C. Niu, M. Zhou, J. L. Zhang, Y. P. Feng, W. Chen, *J. Am. Chem. Soc.* **2013**, 135, 8409.

[71] Y. Hernandez, V. Nicolosi, M. Lotya, F. M. Blighe, Z. Y. Sun, S. De, I. T. McGovern, B. Holland, M. Byrne, Y. K. Gun'ko, J. J. Boland, P. Niraj, G.

Duesberg, S. Krishnamurthy, R. Goodhue, J. Hutchison, V. Scardaci, A. C. Ferrari, J. N. Coleman, *Nat. Nanotechnol.* **2008**, 3, 563.

[72] a) K. Parvez, Z. S. Wu, R. J. Li, X. J. Liu, R. Graf, X. L. Feng, K. Mullen, *J. Am. Chem. Soc.* **2014**, 136, 6083; b) S. Yang, S. Bruller, Z. S. Wu, Z. Y. Liu, K. Parvez, R. H. Dong, F. Richard, P. Samori, X. L. Feng, K. Mullen, *J. Am. Chem. Soc.* **2015**, 137, 13927.

[73] S. Yang, A. G. Ricciardulli, S. Liu, R. Dong, M. R. Lohe, A. Becker, M. A. Squillaci, P. Samori, K. Mullen, X. Feng, *Angew. Chem. Int. Ed.* **2017**, 56, 6669.

[74] S. Yang, K. Zhang, A. G. Ricciardulli, P. P. Zhang, Z. Q. Liao, M. R. Lohe, E. Zschech, P. W. M. Blom, W. Pisula, K. Mullen, X. L. Feng, *Angew. Chem. Int. Ed.* **2018**, 57, 4677.

[75] Hecht D. S., Hu L., Irvin G., *Adv. Mater.* **2011**, 23, 1482.

[76] I. Jeon, K. Cui, T. Chiba, A. Anisimov, A. G. Nasibulin, E. I. Kauppinen, S. Maruyama, Y. Matsuo, *J. Am. Chem. Soc.* **2015**, 137, 7982.

[77] a) W. Wei, G. Wang, S. Yang, X. L. Feng, K. Mullen, *J. Am. Chem. Soc.* **2015**, 137, 5576; b) Z. Y. Liu, Z. S. Wu, S. Yang, R. H. Dong, X. L. Feng, K. Mullen, *Adv. Mater.* **2016**, 28, 2217.

[78] N. G. Park, *Mater. Today* **2015**, 18, 65.

[79] S. A. Veldhuis, P. P. Boix, N. Yantara, M. J. Li, T. C. Sum, N. Mathews, S. G. Mhaisalkar, *Adv. Mater.* **2016**, 28, 6804.

Chapter 2 Solution-Processable High-Quality Graphene for Organic Solar Cells

2.1 Introduction

As described in Chapter 1, the widely used transparent conductive electrode (TCE) in organic optoelectronic devices, such as organic light-emitting diodes (OLEDs) and organic solar cells (OSCs), is Indium Tin Oxide (ITO), which suffers from limited chemical stability, mechanical vulnerability and, more importantly, dwindling price due to the insufficient availability of Indium on earth.[1] Therefore, seeking for an efficient alternative to ITO as TCE is of great significance.

In the carbon family, graphene, which features a unique two-dimensional structure, exceptional thermal, mechanical, electrical and optical properties, is a suitable candidate for TCEs.[2] For example, graphene made from chemical vapor deposition (CVD) delivers a promising power conversion efficiency (PCE) of 2.5% using poly(3-hexylthiophene-2,5-diyl) (P3HT) and [6,6]-phenyl-C_{61}-butyric acid methyl ester ($PC_{61}BM$), as donor and acceptor, respectively.[3] However, as discussed in Chapter 1, CVD scalability is hindered by the high production cost and troublesome process. In contrast, even though reduction of graphene oxide is a potential scalable process,[4] reduced graphene oxide (rGO) has poor electrical properties. Alternatively, electrochemical exfoliation of graphite enables solution-processable graphene flakes with remarkable properties (C/O ratio 21.2), high yield (75%) and, especially, low cost.[5] Exfoliated graphene (EG) has been widely used for a wide range of applications (e.g. batteries, supercapacitors), and the results have outperformed the ones obtained by rGO.[6] Despite this, uniform and continuous coverage of EG on substrates combined with a low sheet resistance, high transparency and low surface roughness are the main challenges for application of EG-based transparent electrodes in optoelectronic devices.

In this chapter, we demonstrate the first example of organic solar cells with a solution-processed transparent electrode based on electrochemical exfoliated graphene. A uniform and smooth electrode is obtained by spray-coating of a high-quality EG dispersion on both glass and flexible polyethylene naphtalate (PEN) substrates. The resulting graphene

transparent electrodes show low sheet resistance, R_s, (ranging from 0.52 kΩ sq^{-1} at 70 T% to 0.18 kΩ sq^{-1} at 55 T%) and high PCE values (4.23%) for OSCs compared to other solution-processable graphene TCEs. This study will pave the way to a wide survey of flexible and light-weighted electronic devices.

2.2 Results and Discussion

High-quality graphene was obtained according to the electrochemical exfoliation of graphite (Figure 2.1a and 2.1b) outlined in our previous works,[5, 7] in which graphite foil and platinum have been used, respectively, as working and counter electrode. An aqueous solution of ammonium sulfate was used as electrolyte. Graphene was easily formed upon the application of a 10 V bias and subsequently collected at the top of the electrolyte. Graphene sheets were filtered, washed several times with water/ethanol and finally dispersed in *N,N'*-dimethylformamide (DMF) via mild sonication. Based on the mass ratio of dried graphene powder from dispersion and the starting graphite electrode, a high exfoliation yield of 78% has been achieved. Since re-stacking of the flakes occurs due to π-π interactions of high quality graphene and graphitic aggregations could be present in the dispersion, being detrimental for the solar cells, the EG dispersion in DMF was centrifuged at 6000 rpm twice in order to get rid of these aggregates and particles. Only 8% of yield loss, as precipitate after centrifugation, has been observed. The slight yield decrease is attributed to the small fraction of multiple-layered EG flakes in the dispersion.

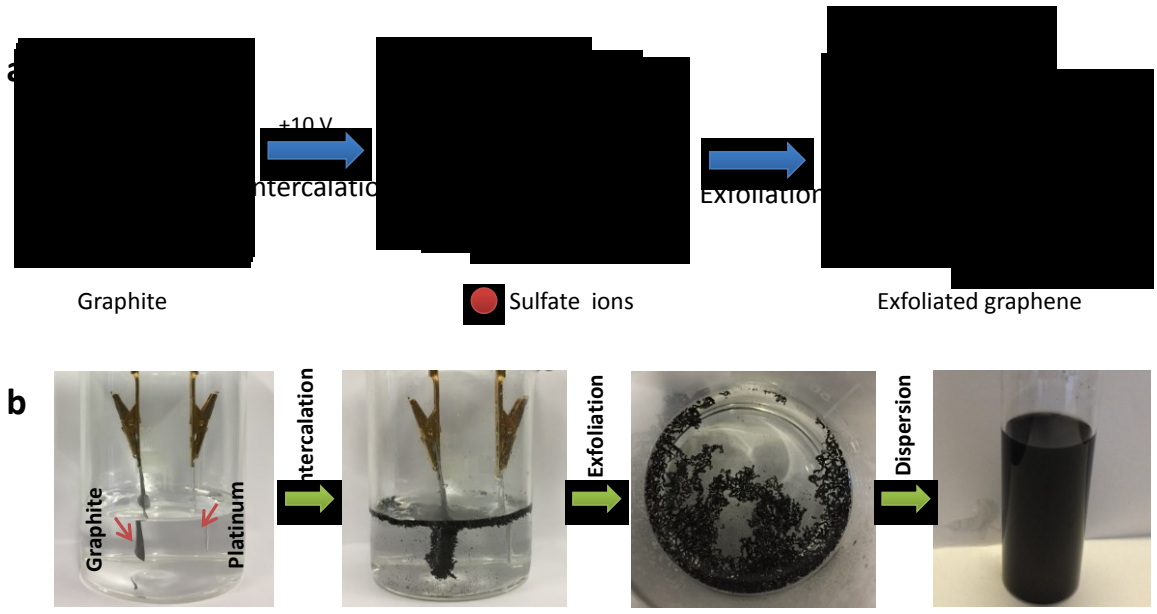

Figure 2.1 a) Schematic illustration of the electrochemical exfoliation of graphite. b) Optical images of the exfoliation process.

Atomic force microscopy (AFM) on the as-synthesized exfoliated graphene demonstrates the two-dimensional (2D) feature of the nanosheets (Figure 2.2a). The typical cross-section of a single graphene sheet shows a thickness of 0.80 nm, being a sign of a single-layer graphene flake.[8] The thickness distribution on 100 graphene sheets (Figure 2.2b and 2.2c) obtained by cross-sectional analysis shows that approximately 90% of EG sheets are between one and three layers thick. The presence of extremely thin flakes makes EG a suitable candidate for flexible and stretchable applications.[9]

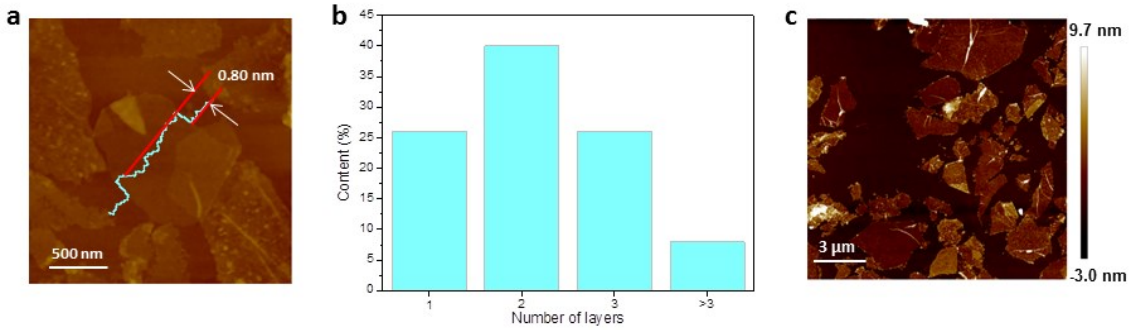

Figure 2.2 a) AFM image of single layer EG sheet on SiO_2 by Langmuir-Blodgett technique. b) Graphene sheets thickness distribution from AFM analysis on randomly selected 100 flakes. c) AFM image of a random EG sample used for distribution analysis.

Transmission electron microscopy (TEM) also confirms the presence of thin-layered graphene sheets (Figure 2.3a). Further, the selected-area electron diffraction (SAED) image (Figure 2.3b) at the central part of the graphene sheet reveals the high-quality crystalline structure as manifested by the typical 6-fold symmetry.

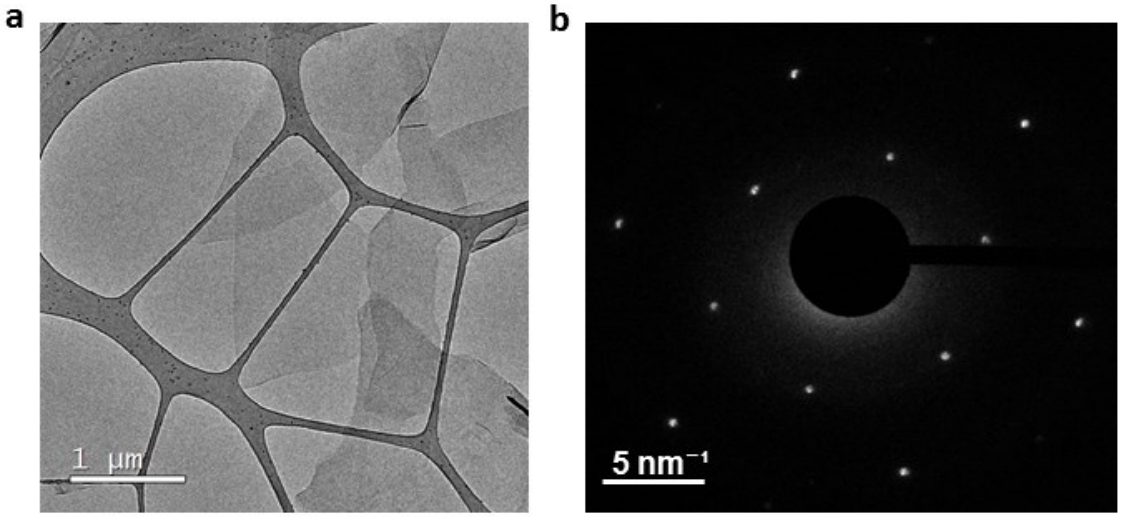

Figure 2.3 a) TEM image of EG flakes and b) the corresponding diffraction pattern.

Working optoelectronic devices rely on smooth and uniform coatings, indeed the best coating method should be evaluated according to the nature of the material. Several techniques, such as spin coating and vacuum filtration, have been explored in order to achieve a uniform EG film. However spin coating does not yield even coatings on the substrates, since multiple spin coating steps of pristine EG dispersion should be carried out to achieve a graphene film. In contrast, vacuum filtration leads to vacancies on the film while peeling off the membrane (Figure 2.4).

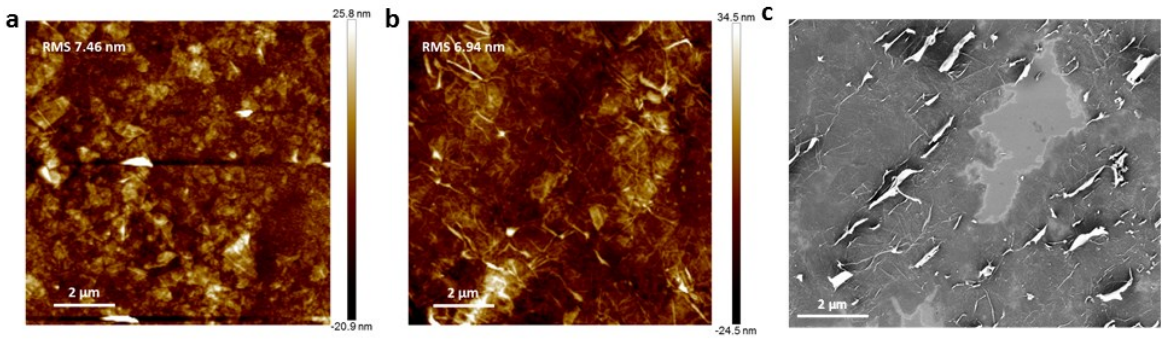

Figure 2.4 AFM images with RMS values of graphene thin-films by a) spin coating and b) vacuum filtration. Bundles can protrude up to the active layer causing short circuit. c) SEM image of graphene film by vacuum filtration: wrinkles of graphene sheets in the orientation of the membrane peeling.

Alternatively, spray coating is versatile for various substrates with desirable shape and, more importantly, can easily manipulate the film morphology through the control of spray pressure and distance between substrate and airbrush nozzle. With a shadow mask, it is possible to directly yield TCEs with the designed pattern. Therefore, a uniform and smooth EG film has been realized by spray-coating on both rigid and flexible substrates (Figure 2.5a). As proof of scalability, a 21.0 cm x 29.7 cm (standard A4 size) TCE has been manufactured on PEN (Figure 2.5b) by spray-coating.

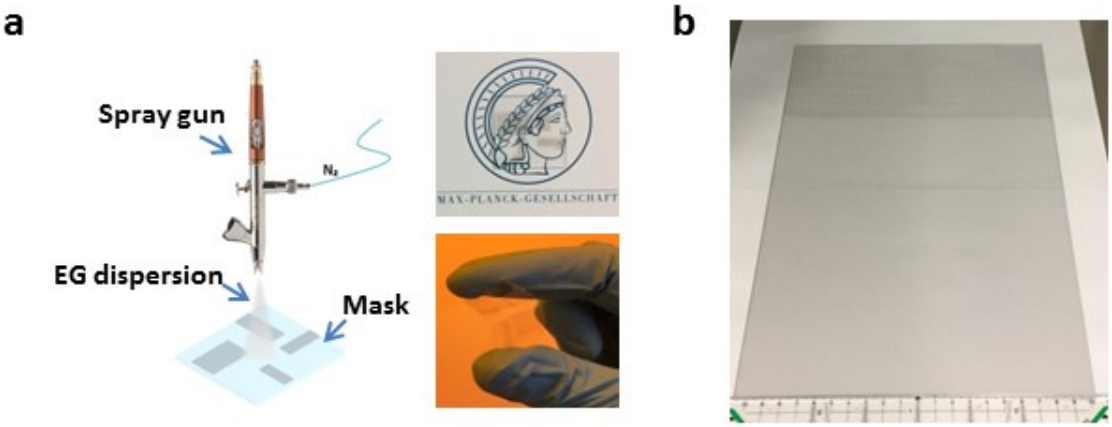

Figure 2.5 a) Schematic illustration of spray deposition of EG dispersion onto a substrate. Inset: optical images of graphene TCE on both glass and flexible PEN substrates. b) A4-sized EG transparent electrode by spray coating.

In this work, the optimized spray pressure is 2.1 bar and the substrate-to-nozzle distance fixed at 13 cm (Figure 2.6). This coating technique is fully compatible with the production of large area films.

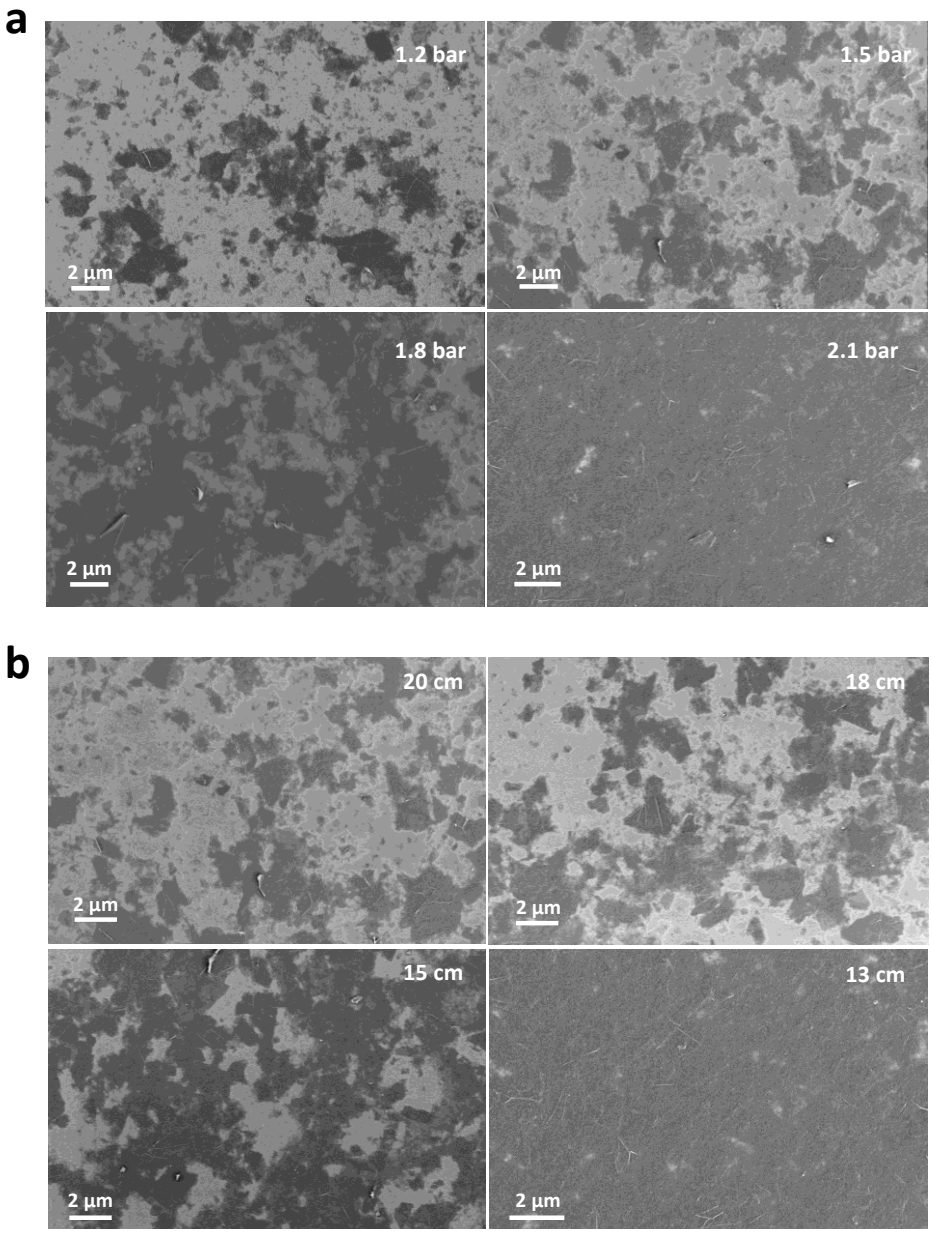

Figure 2.6 a) SEM images of EG films obtained at different spray pressures. b) SEM images of EG films obtained at various nozzle-to-substrate distances at the fixed optimized spray pressure (2.1 bar).

Structural characterization of the transparent electrode has been performed by AFM and scanning electron microscopy (SEM). As expected, the SEM (Figure 2.7a) reveals a

uniform and smooth film of 2D graphene sheets, overlapped each other, which is beneficial for the electron conduction. As shown in Figure 2.7b, the AFM image on a spray-coated EG film reveals low root-mean-square (RMS) roughness of 2.86 nm and absence of aggregates. The fine control of the morphology of solution-processable graphene is the greatest challenge for the implementation of such materials in optoelectronic devices since both low roughness and uniformity of the layers are essential requirements for a working device, preventing short circuits and alternative current paths, which lead to significant power losses.[10]

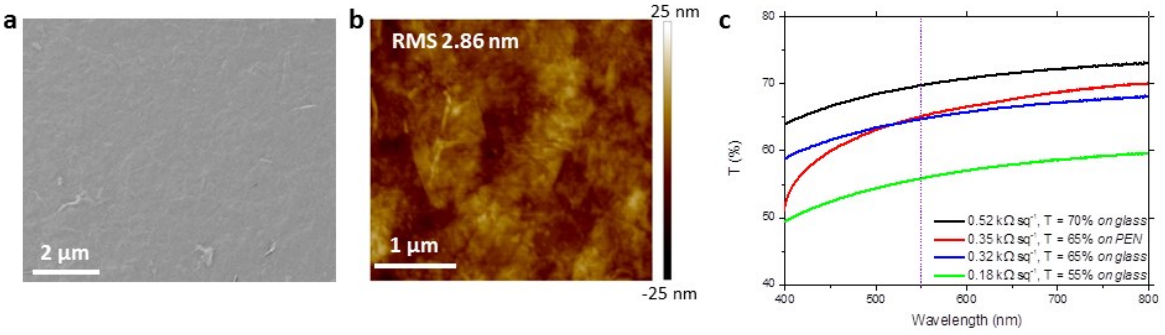

Figure 2.7 a) SEM image of a spray-coated EG film. b) AFM image of as-sprayed graphene on a glass substrate. c) UV-vis spectra of EG films on glass (black, blue and green plot) and PEN (red plot), at different Rs values.

The combination of the UV-vis spectrum (Figure 2.7c) with the sheet resistance (R_s) measurement carried out with a four points probe apparatus shows a R_s of only 0.32 kOhm sq^{-1} and 0.18 kOhm sq^{-1} for the 65% and 55% transparent film at 550 nm, respectively. The resulting homogeneous films show very low R_s values, which favorably compare to previously reported values for films based on solution-processable graphene (Table 2.1).[11]

Table 2.1 Summary of sheet resistance values of solution-processable graphene films in OSCs.

Material	Rs (kΩ sq^{-1})	T (%)	Ref.
rGO	100	85	*Appl. Phys. Lett.* 2008, *92* (26), 3
rGO	3.20	65	*ACS Nano* 2010, *4* (9), 5263-5268
rGO	17.9	69	*Carbon* 2010, *48* (11), 3308-3311
CCG[a)]	6	78	*J. Phys. Chem. C* 2010, *114* (34), 14433-14440
LrGO[b)]	1.60	70	*Adv. Funct. Mater.* 2013, *23* (21), 2742-2749
LrGOmm[c)]	0.56	59	*Adv. Funct. Mater.* 2015, *25* (15), 2213-2221
EG	0.52-0.18	70-55	This work

[a)] *chemical converted graphene patterned by photolithography;* [b)] *Laser-treated rGO;* [c)] *Laser-treated rGO micromesh*

Moreover, the EG films prepared by our method are mechanically robust. Even after variable bending angles (from 10° to 120°) and 150 bending cycles the R_s values do not show apparent changes (Figure 2.8). Remarkably, the R_s values of the EG films in our work are even lower than the reported ones which require post-treatments (e.g. laser patterning,[11f] thermal annealing[12]) to obtain higher transparencies at lower R_s.

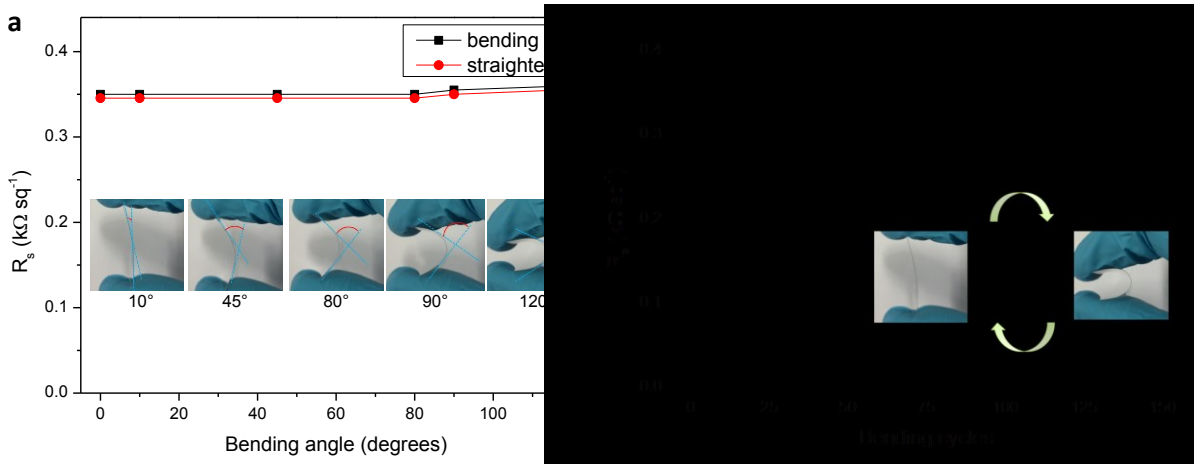

Figure 2.8 R_s values of EG film on PEN substrate at a) different bending angles and b) bending cycles.

The improved values of R_s are ascribable to the lower degree of defects of the EG. This has been verified by Raman spectra (Figure 2.9a), which have revealed that the intensity of the G peak (1581 cm^{-1}), expressing the in-plane vibrations of the graphene lattice, is almost three and a half times that of the D peak (1350 cm^{-1}), which originates from defects.[13] The derived I_D/I_G value (0.29) is much smaller than that of reduced graphene oxide, typically in the range of 1.1-1.5.[14] The surface components of the EG film have been investigated by X-ray photoelectron spectroscopy (XPS). According to the XPS survey spectrum, the oxygen content is as low as 5.3 atom % (Figure 2.9b), corresponding to a C/O ratio of 17.9. The high-resolution spectrum of C 1s peak (Figure 2.9c) exhibits three dominate bands at 284.7 eV, 285.5 eV and 287.4 eV, which are related respectively to C-C, C-O and C=O bonds.[7]

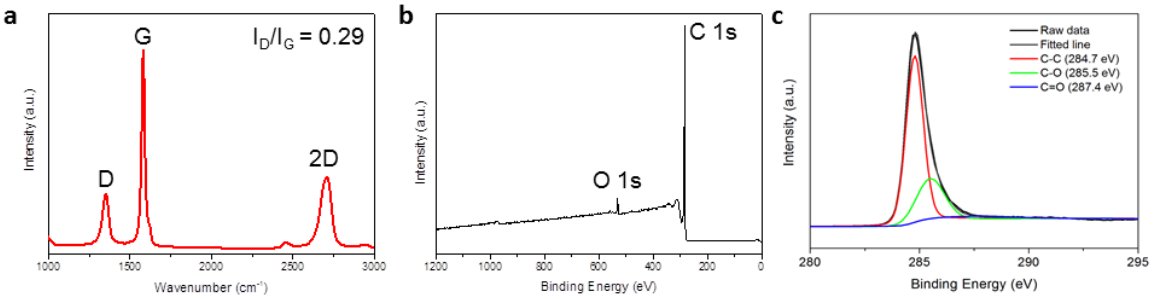

Figure 2.9 a) Raman spectrum, b) XPS survey spectrum of EG film. and c) High-resolution XPS of C 1s spectrum of EG, respectively.

To evaluate the potential application of EG as TCE, we fabricated bulk heterojunction (BHJ) OSCs (Figure 2.10a), using poly[[4,8-bis[(2-ethylhexyl)oxy]benzo[1,2-b:4,5-b']dithiophene-2,6-diyl][3-fluoro-2-[(2-ethylhexy)carbonyl]thieno[3,4-*b*]thiophenediyl]] (PTB7) and $PC_{71}BM$ as donor and acceptor material, respectively. The PTB7: $PC_{71}BM$ blend is generally used as benchmark active layer in BHJ organic photovoltaics (OPV).[15] Poly(3,4-ethylenedioxythiophene) polystyrene sulfonate (PEDOT:PSS) was used as hole transport layer (HTL). A uniform coating of hydrophilic PEDOT:PSS onto hydrophobic EG represents a challenge due to the wetting mismatch of their surface.[16] Indeed, a homogeneous PEDOT:PSS layer on EG is essential, not only for its planarization effect, but also to avoid any current leakage path and decrease the shunt resistance, harmful for a proper working device.

To tune the hydrophobic surface of EG, application of a UV-ozone or O_2 plasma could be considered. Unfortunately, these treatments result in a decrease of graphene conductance due to the disruption of aromatic rings by covalent bonding (i.e. -OH, C=O groups).[17] In order to overcome this challenge, a 0.1% of fluorosurfactant (Zonyl™) was added to the PEDOT:PSS solution to alter the wettability,[18] hence, a smooth coverage of HTL on EG was successfully achieved. At the top of the device structure, Barium (Ba) and Aluminum (Al) were evaporated as cathodes.

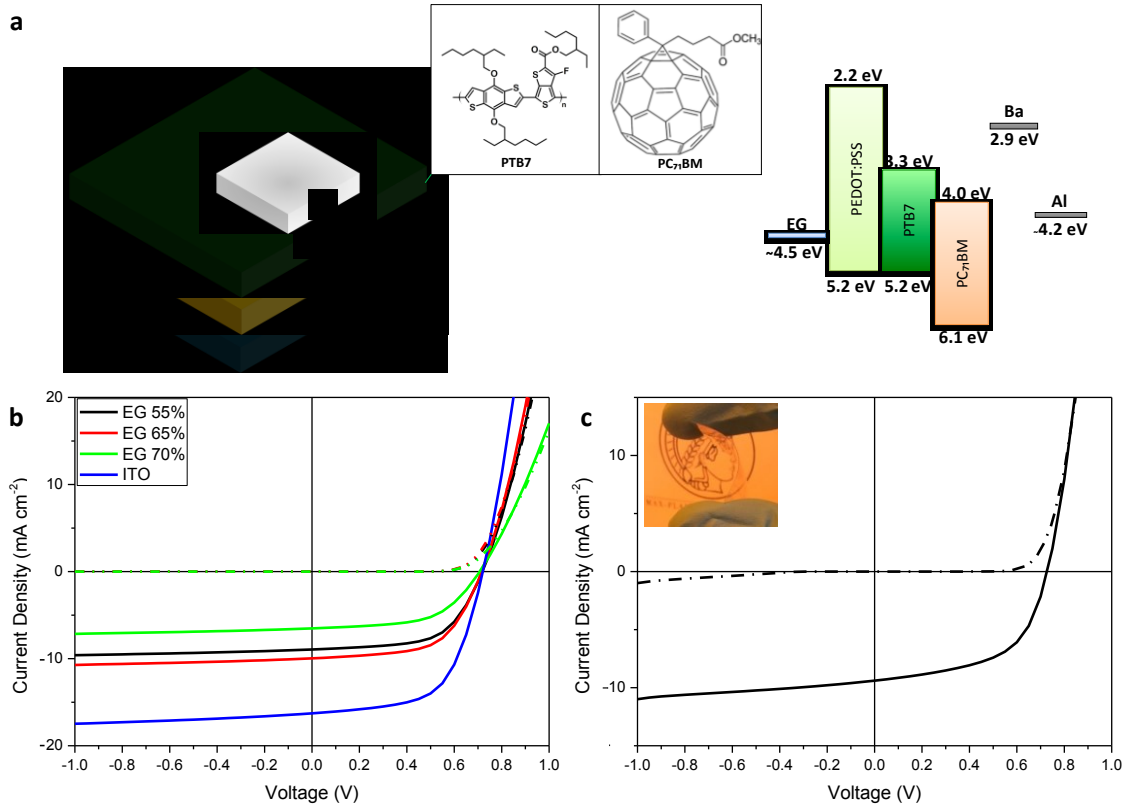

Figure 2.10 a) Schematic representation of the EG photovoltaic device structure and its energy band alignment diagram. b) *J-V* curves of EG-based OSCs at different graphene loads, under light (solid lines) and dark conditions (dashed lines), in comparison with ITO (blue line). c) *J-V* characteristics of an EG-OSC on flexible substrate under light (solid line) and dark conditions (dashed line).

The optimum performance was determined by measuring the *J-V* characteristics for devices with different EG film transparencies (Table 2.2). The device is constrained by the trade-off between transparency and series resistance. A high transparency, meaning a thin EG layer, is beneficial for light absorption and resulting photocurrent, but detrimental for the series resistance. A high series resistance will reduce the effective voltage over the solar cell and lead to a reduction of the fill factor. A thick EG layer with low resistance would lead to an enhancement of the fill factor, but the reduced absorption would limit the photocurrent generation. The as-fabricated solar cell with 65 % transparent EG anode exhibits, upon illumination under 1.5 AMG (100 mW cm^{-2}), the best performance with a short-circuit current density (J_{sc}) of 9.97 mA cm^{-2} with an open-circuit voltage (V_{oc}) of 715 mV and a fill factor (FF) of 59.3, for an overall PCE of 4.23% (Figure 2.10b). Compared to the ITO-based counterpart, the reduced J_{sc} and FF of the EG-based OSCs are mainly due to a lower transparency and higher R_s of the EG anode. Interestingly, the V_{oc} of the devices using EG as anode is similar to the ITO-based counterpart. Hence, ITO and EG extract equally the charges and this is also confirmed by the value of the work function of EG, 4.55 eV, measured by Kelvin probe. Furthermore, we have deposited EG on flexible PEN substrates. The assembled flexible solar cells demonstrate a PCE value of 3.77%, comparable to the efficiency of single-walled carbon nanotube-based flexible OPV devices.[19] The slight lower efficiency is ascribed to the reduced transmittance of the PEN, which results in a modest reduced absorption of photons (Figure 2.10c).

Table 2.2 Photovoltaic performance for the OPV devices at different graphene transparency values and for the reference ITO OSC.

Conductive Anode	V_{oc} (mV)	J_{sc} (mA cm^{-2})	FF	PCE (%)
ITO	720	16.2	60.2	7.06
$EG_{55\%}$	718	8.94	59.8	3.84
$EG_{65\%}$	715	9.97	59.3	4.23
$EG_{70\%}$	707	6.53	56.5	2.61
$EG_{65\%\ on\ PEN}$	722	8.80	59.3	3.77

Bending test has been evaluated to understand the mechanical stability of our devices (Figure 2.11). Interestingly, after 150 bending cycles there is no significant change in PCE, which remains at 99% of its original value, thanks to the flexibility and robustness of EG thin flakes.

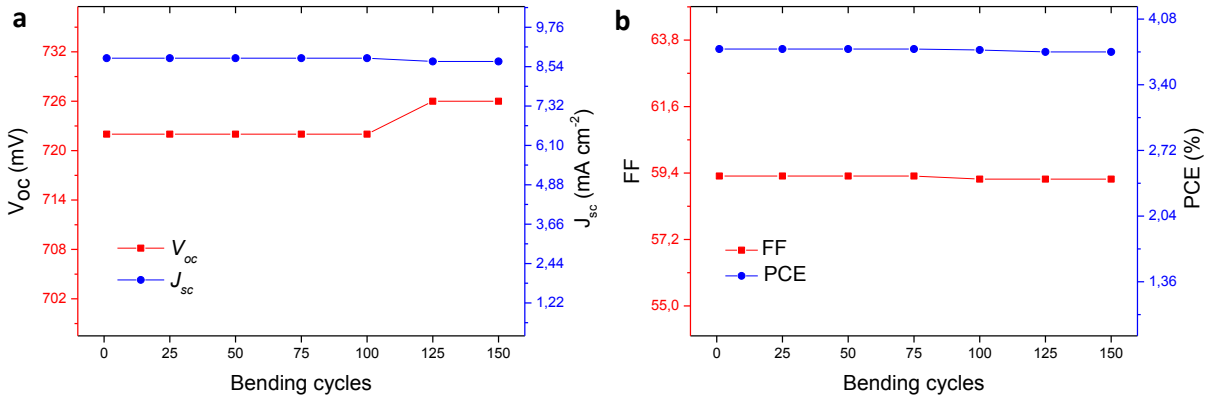

Figure 2.11 Variation of (a) V_{oc}, J_{sc} and (b) FF, PCE over 150 bending cycles of a flexible EG-based OSC.

The statistical analysis carried out over a set of 36 OSCs with EG as TCE (Figure 2.12 and Table 2.3), shows the reliability of the graphene and processes utilized in this work. Indeed, the average PCE for the solar cells with the 65% transparent EG anode is 4.16% with a standard deviation of 0.11, where all the devices work properly and the majority of them exhibit the maximum PCE value of 4.23%.

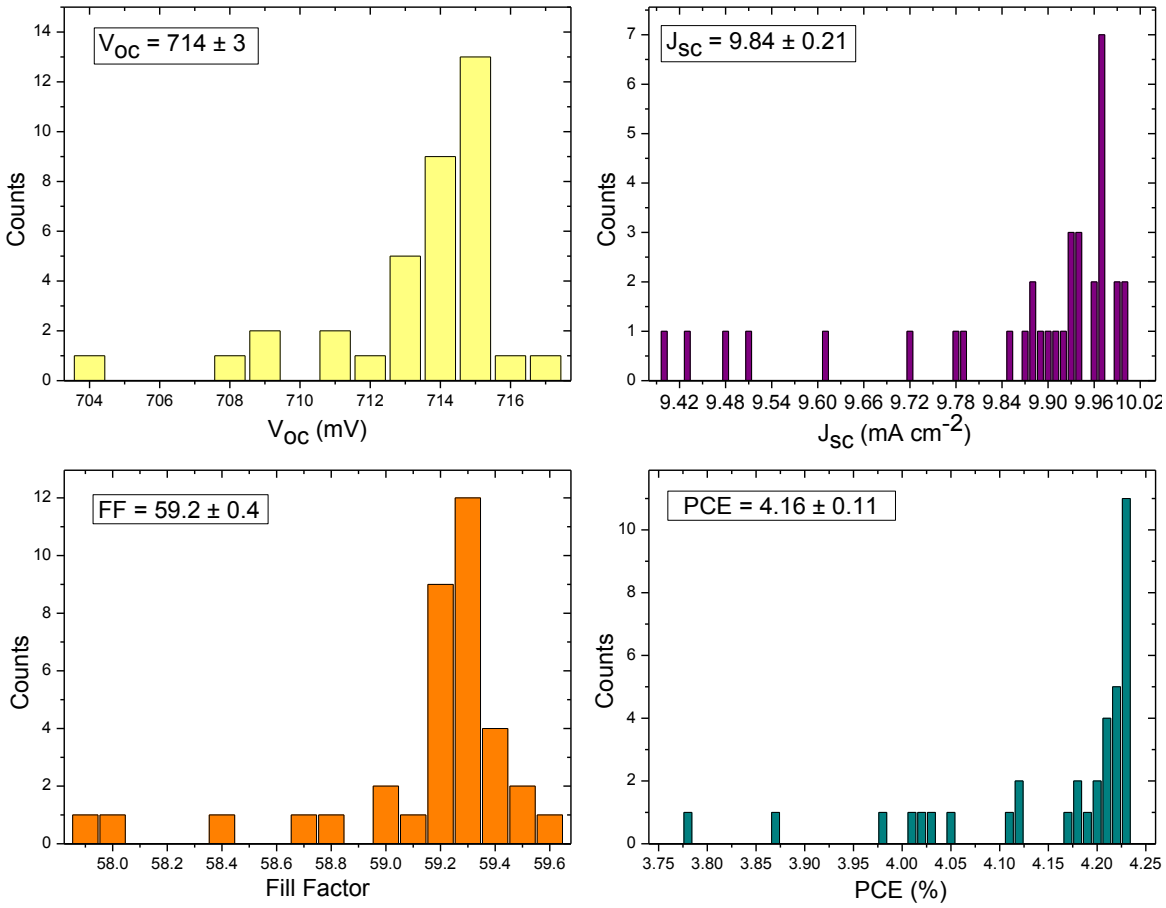

Figure 2.12 Histograms of device parameters (V_{oc}, J_{sc}, FF and PCE) for a set of 36 OSCs with 65% transparent EG as anode.

Table 2.3 Average photovoltaic parameters with the related standard deviations.

Conductive Anode	V_{oc} (mV)	J_{sc} (mA cm^{-2})	FF	PCE (%)
$EG_{55\%}$	716 ± 4	8.80 ± 0.21	59.6 ± 0.4	3.76 ± 0.11
$EG_{65\%}$	714 ± 3	9.84 ± 0.21	59.2 ± 0.4	4.16 ± 0.11
$EG_{70\%}$	702 ± 8	6.31 ± 0.40	56.1 ± 1.2	2.49 ± 0.22
$EG_{65\%\ on\ PEN}$	720 ± 3	8.56 ± 0.22	59.1 ± 0.5	3.66 ± 0.12

Additionally, the PCE values of EG-based OSCs fabricated in this work have been compared to OSCs with other solution-processed graphene based TCE reported in literature (Table 2.4 and Figure 2.13).[10-11] The quality of EG and the fine control of film morphology have a large impact on the device performance.

Table 2.4 Comparison of the PCE values of OSCs with solution-processable graphene based TCE.

Device Structure	PCE (%)	Ref.
rGO/CuPc[a)]/C_{60}[b)]/BCP[c)]/Ag[d)]	0.40	*Appl. Phys. Lett.* 2008, *92* (26), 3
rGO-CNT[e)]/ PEDOT:PSS/P3HT:PCBM/Ca/Al	0.85	*Nano Lett.,* 2009*, 9,* 1949
rGO/PEDOT:PSS/P3HT:PCBM/TiO_2[f)]/Al[g)]	0.78	*ACS Nano* 2010, *4* (9), 5263-5268
rGO/PEDOT:PSS/P3HT:PCBM/LiF[h)]/Al	0.13	*Carbon* 2010, *48* (11), 3308-3311
CCG/PEDOT:PSS/P3HT:PCBM/Al	1.01	*J. Phys. Chem. C* 2010, *114* (34), 14433-14440
LrGO/PEDOT:PSS/P3HT:PCBM/Al	1.10	*Adv. Funct. Mater.* 2013, *23* (21), 2742-2749
LrGOmm/PEDOT:PSS/PCDTBT:PCBM/TiOx/Al	3.05	*Adv. Funct. Mater.* 2015, *25* (15), 2213-2221
EG/PEDOT:PSS/PTB7:PCBM/Ba[i)]/Al	4.23	This work

[a)] *Copper(II) phthalocyanine;* [b)] *[60]fullerene* [c)] *bathocuproine;* [d)] *silver;* [e)] *carbon nanotube* [f)] *titanium oxide;* [g)] *aluminum;* [h)] *lithium fluoride;* [i)] *barium*

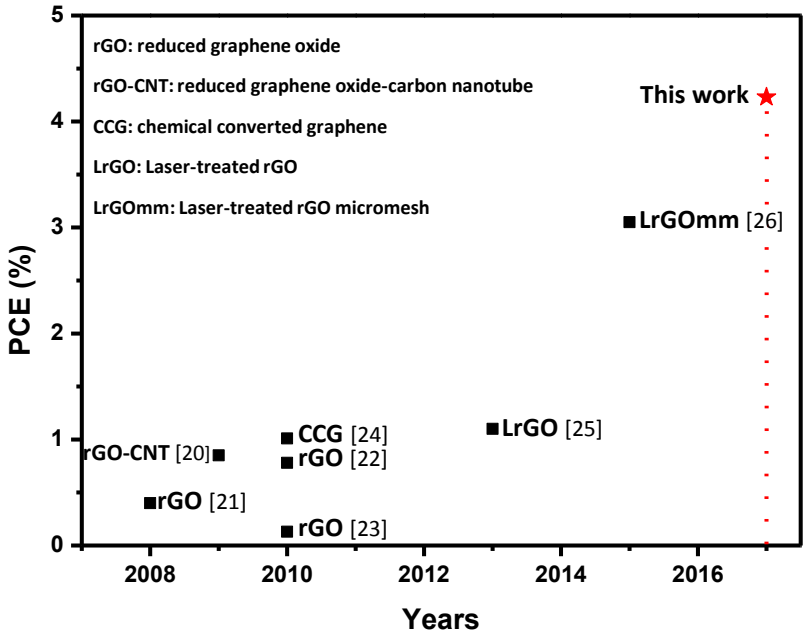

Figure 2.13 PCE values of OSCs with solution-processable graphene based TCE.

We note that the apparent progress in Figure 2.13 is not solely due to an improvement of the EG properties. In the various studies different active layers have been used which complicates a direct comparison. Therefore, Figure 2.13 is intended to show the development of reported efficiencies of OSCs with a solution-processed graphene electrode. However, for the benchmark P3HT:PCBM system we also found an increased performance of our EG based anodes as compared to earlier reported values (Table 2.5). Future options to further increase the efficiency of OSCs with EG anodes are the optimization of the electrochemical exfoliation process and employing post-techniques to achieve higher film transparency at lower sheet resistance values (i.e. laser patterning).[20]

Table 2.5 Comparison of the PCE values of P3HT:PCBM based BHJ OSCs with solution-processable graphene based TCE.

Device Structure	**PCE (%)**	**Ref.**
rGO-CNT/ PEDOT:PSS/P3HT:PCBM/Ca/Al	0.85	*Nano Lett.,* **2009***, 9,* 1949
rGO/PEDOT:PSS/P3HT:PCBM/LiF/Al	0.78	*ACS Nano* **2010**, *4* (9), 5263-5268
rGO/PEDOT:PSS/P3HT:PCBM/TiO_2/Al	0.13	*Carbon* **2010**, *48* (11), 3308-3311
rGO/PEDOT:PSS/P3HT:PCBM/Al	1.01	*J. Phys. Chem. C* **2010**, *114* (34), 14433-14440
LrGO/PEDOT:PSS/P3HT:PCBM/Al	1.10	*Adv. Funct. Mater.* **2013**, *23* (21), 2742-2749
EG/PEDOT:PSS/P3HT:PCBM/Ba/Al	1.31	This work

2.3 Conclusion

In conclusion, this chapter describes an efficient, scalable and cost-effective method for the production of high-quality graphene as TCE for OSCs. Electrochemical exfoliated graphene was employed for the first time in organic photovoltaics with a fine control of the morphology and uniformity of the film, showing improved features as compared to other solution-processable graphene-based TCEs up-to-date. A PCE value of 4.23% has been achieved for PTB7:PCBM based OPV device. Our work is a step forward towards the application of solution-processable high-quality graphene as transparent electrode in solar cells as well as other organic electronics (i.e. OLED).

Experimental Session

Graphite Exfoliation. Commercial graphite foil (Alfa Aesar) was pre-treated with liquid nitrogen for few seconds and ethanol to generate an expansion. Graphite exfoliation was performed in a two-electrode system, where graphite foils were used as working anodes and platinum foils as counter electrodes. The electrodes were placed at a distance of 2 cm. The electrolyte for the graphite exfoliation was prepared by dispersing ammonium sulfate crystals in DI water, obtaining a 0.1M solution. Subsequently, the electrodes were immersed in the electrolyte and a static potential of 10 V was applied to start the electrochemical exfoliation process. Once the exfoliation was complete, the suspended graphene sheets were collected through a 0.2 μm PTFE membrane filter (Sartorius™) and washed several times with DI water and ethanol. Then, the product was dispersed in N,N-dimethylformamide (DMF) via strong sonication in an ice bath for 15 minutes.

Purification of graphene. The graphene dispersion was centrifuged to separate out any un-exfoliated flakes and large particles. The solution was transferred in plastic tubes and centrifuged twice at 6000 rpm for 60 minutes. Afterwards, the supernatant was taken out from the suspension and sonicated for 15 minutes to ensure homogeneity.

Preparation of EG electrodes. EG films were prepared on both glass and PEN (Pütz GMBH + Co. Folien KG) by spray-coating through an Infinity CRplus airbrush (Harder & Steenbeck GmbH). The EG dispersion was sprayed onto 3x3 cm^2 pre-heated substrates under a N_2-assisted inlet pressure of 2.1 bar. The distance between the tip of the nozzle and the substrate was fixed at 13 cm. By either varying the volume or concentration of EG solution, films with different transparencies can be produced. The resulting films were heated at 110 °C overnight in a vacuum oven to remove residual solvent before use.

As control experiments spin coating and vacuum filtration were investigated. Spin-coated EG films were prepared by dispense an EG ink (DMF as solvent) each 30 seconds at a rate of 1000 rpm. The as-casted graphene TCEs were dried at 110 °C overnight in a vacuum oven. EG films by vacuum filtration were prepared by filtering the EG solutions through PTFE membranes. The EG-coated membranes were transferred on the substrates

and subsequently placed under a mechanical press to adhere to the substrates. After 30 minutes, the membranes were peeled off and the EG films dried at 110 °C in a vacuum oven.

Photovoltaic device fabrication. To obtain the required wetting of the PEDOT:PSS layer on the graphene electrode, a fluorosurfactant (Zonyl™) with a concentration of 0.1% v/v was added in an aqueous solution of PEDOT:PSS (Clevios P VP Al4083, Heraeus Precious Metals GmbH & Co.). The mixture was stirred overnight and spin-coated on top of the patterned electrodes at 1500 rpm for 50 s. The films were then heated at 130 °C for 20 minutes and transferred in a glove-box for the deposition of the PTB7:$PC_{71}BM$ photoactive layer. The PTB7:$PC_{71}BM$ blend was prepared in a mixed solvent of chlorobenzene and 1,8-diiodoctane (DIO) at a 97:3 ratio. PTB7 (10 mg) and $PC_{71}BM$ (15 mg) were initially dissolved in CB inside a glove-box (0.97 mL). The solution was left stirring overnight at 80 °C. After this period, the corresponding amount of DIO (30 μL) was added and the new solution was stirred 1 h at 70 °C. The blend solution was spin-coated on the top of PEDOT:PSS layer at 1500 rpm for 60 s. As a top electrode, Ba (5 nm) followed by Al (100 nm) was deposited by vacuum thermal evaporation.

Characterization. Current-Voltage (*J-V*) characteristics were measured by a software controlled source meter (Keithley 2400) at room temperature with a 1.5 AMG (100 mW cm^{-2}) solar simulator. Sheet resistance measurements were carried out by using a four-point probe system with a Keithley 2700 Multimeter (probe spacing: 0.635 mm, Rs= 4.5324 V/I). AFM measurements were carried out on a Digital Instruments Dimension 3100. SEM images were obtained using a field-emission scanning electron microscope (Gemini 1530 LEO). TEM and SAED were performed using a transmission electron microscope (Philips Tecnai F20). Bruker RFS 100/S spectrometer with a laser wavelength of 532 nm was used for Raman spectroscopy measurements. UV-vis spectroscopy was performed on Perkin Elmer Lambda 900 spectrometer. XPS measurements were carried out on a PHI–5000C ESCA system with a monochromatic Mg Kα X-ray source ($h\nu$ = 1253.6 eV), the C 1s value was set at 284.7 eV for charge corrections. Work function

measurements were accomplished with an Anfatec Ambient Single Point Kelvin Probe System, using highly oriented pyrolytic graphite (HOPG) as reference (work function = 4.46 eV).

References

[1] Hecht D. S., Hu L., Irvin G., *Adv. Mater.* **2011**, 23, 1482.

[2] a) K. S. Kim, Y. Zhao, H. Jang, S. Y. Lee, J. M. Kim, K. S. Kim, J. H. Ahn, P. Kim, J. Y. Choi, B. H. Hong, *Nature* **2009**, 457, 706; b) S. Bae, H. Kim, Y. Lee, X. Xu, J.-S. Park, Y. Zheng, J. Balakrishnan, T. Lei, H. R. Kim, Y. I. Song, Y.-J. Kim, K. S. Kim, B. Özyilmaz, J.-H. Ahn, B. H. Hong, S. Iijima, *Nat. Nanotechnol.* **2010**, 5, 574; c) Z. Y. Yin, J. X. Zhu, Q. Y. He, X. H. Cao, C. L. Tan, H. Y. Chen, Q. Y. Yan, H. Zhang, *Adv. Energy Mater.* **2014**, 4, 19; d) K. P. Loh, S. W. Tong, J. S. Wu, *J. Am. Chem. Soc.* **2016**, 138, 1095.

[3] Y. Wang, S. W. Tong, X. F. Xu, B. Ozyilmaz, K. P. Loh, *Adv. Mater.* **2011**, 23, 1514.

[4] C. K. Chua, M. Pumera, *Chem. Soc. Rev.* **2014**, 43, 291.

[5] S. Yang, A. G. Ricciardulli, S. Liu, R. Dong, M. R. Lohe, A. Becker, M. A. Squillaci, P. Samori, K. Mullen, X. Feng, *Angew. Chem.-Int. Edit.* **2017**, 56, 6669.

[6] a) W. Wei, G. Wang, S. Yang, X. L. Feng, K. Mullen, *J. Am. Chem. Soc.* **2015**, 137, 5576; b) Z. Y. Liu, Z. S. Wu, S. Yang, R. H. Dong, X. L. Feng, K. Mullen, *Advanced Materials* **2016**, 28, 2217.

[7] S. Yang, S. Bruller, Z. S. Wu, Z. Y. Liu, K. Parvez, R. H. Dong, F. Richard, P. Samori, X. L. Feng, K. Mullen, *J. Am. Chem. Soc.* **2015**, 137, 13927.

[8] G. Wang, M. Zhang, Y. Zhu, G. Q. Ding, D. Jiang, Q. L. Guo, S. Liu, X. M. Xie, P. K. Chu, Z. F. Di, X. Wang, *Sci Rep* **2013**, 3, 6.

[9] a) X. Peng, L. L. Peng, C. Z. Wu, Y. Xie, *Chem. Soc. Rev.* **2014**, 43, 3303; b) T. Cheng, Y. Z. Zhang, W. Y. Lai, W. Huang, *Adv. Mater.* **2015**, 27, 3349.

[10] V. C. Tung, L. M. Chen, M. J. Allen, J. K. Wassei, K. Nelson, R. B. Kaner, Y. Yang, *Nano Lett.* **2009**, 9, 1949.

[11] a) J. B. Wu, H. A. Becerril, Z. N. Bao, Z. F. Liu, Y. S. Chen, P. Peumans, *Appl. Phys. Lett.* **2008**, 92, 3; b) Z. Y. Yin, S. Y. Sun, T. Salim, S. X. Wu, X. A. Huang, Q. Y. He, Y. M. Lam, H. Zhang, *ACS Nano* **2010**, 4, 5263; c) Y. F. Xu, G. K. Long, L. Huang, Y. Huang, X. J. Wan, Y. F. Ma, Y. S. Chen, *Carbon* **2010**, 48, 3308; d) J. X. Geng, L. J. Liu, S. B. Yang, S. C. Youn, D. W. Kim, J. S. Lee, J. K. Choi, H. T. Jung, *J. Phys. Chem. C* **2010**, 114, 14433; e) E. Kymakis, K. Savva, M. M. Stylianakis, C. Fotakis, E. Stratakis, *Adv. Funct. Mater.* **2013**, 23, 2742; f)

D. Konios, C. Petridis, G. Kakavelakis, M. Sygletou, K. Savva, E. Stratakis, E. Kymakis, *Adv. Funct. Mater.* **2015**, 25, 2213.

[12] J. Z. Liu, M. Notarianni, G. Will, V. T. Tiong, H. X. Wang, N. Motta, *Langmuir* **2013**, 29, 13307.

[13] A. C. Ferrari, J. C. Meyer, V. Scardaci, C. Casiraghi, M. Lazzeri, F. Mauri, S. Piscanec, D. Jiang, K. S. Novoselov, S. Roth, A. K. Geim, *Phys. Rev. Lett.* **2006**, 97, 4.

[14] Y. X. Wang, S. L. Chou, H. K. Liu, S. X. Dou, *Carbon* **2013**, 57, 202.

[15] a) Z. K. Liu, J. H. Li, F. Yan, *Adv. Mater.* **2013**, 25, 4296; b) D. S. Leem, A. Edwards, M. Faist, J. Nelson, D. D. C. Bradley, J. C. de Mello, *Adv. Mater.* **2011**, 23, 4371.

[16] H. Park, S. Chang, X. Zhou, J. Kong, T. Palacios, S. Gradecak, *Nano Lett.* **2014**, 14, 5148.

[17] S. Huh, J. Park, Y. S. Kim, K. S. Kim, B. H. Hong, J. M. Nam, *ACS Nano* **2011**, 5, 9799.

[18] M. Vosgueritchian, D. J. Lipomi, Z. A. Bao, *Adv. Funct. Mater.* **2012**, 22, 421.

[19] I. Jeon, K. Cui, T. Chiba, A. Anisimov, A. G. Nasibulin, E. I. Kauppinen, S. Maruyama, Y. Matsuo, *J. Am. Chem. Soc.* **2015**, 137, 7982.

[20] S. Hong, J. Yeo, G. Kim, D. Kim, H. Lee, J. Kwon, H. Lee, P. Lee, S. H. Ko, *ACS Nano* **2013**, 7, 5024.

The content of this chapter has been published in:
ACS Applied Materials & Interfaces (*ACS Appl. Mater. Interfaces*, **2017**, *9*, 25412)
Solution-Processable High-Quality Graphene for Organic Solar Cells
Antonio Gaetano Ricciardulli, Sheng Yang, Xinliang Feng, Paul W. M. Blom*

Chapter 3 Hybrid Silver Nanowire and Graphene Based Solution-processed Transparent Electrode for Organic Optoelectronics

3.1 Introduction

Organic solar cells (OSCs) based on solution-processed graphene transparent conducting electrodes (TCE), described in Chapter 2, exhibit lower efficiency as compared to their ITO-based counterparts. Graphene electrodes suffer from limited conductivity at higher transmittance values. To enhance their performances, we evaluate the combination of silver nanowires (AgNWs) with electrochemical exfoliated graphene (EG) in this chapter.

As discussed in Chapter 1, one-dimensional (1D) materials, like AgNWs, have recently emerged as potential candidates for TCEs because of promising optical and electrical properties.[1] However the metal NWs films exhibit several drawbacks concerning large contact resistance[2] and high surface roughness,[3] detrimental for optoelectronic applications. To overcome these limitations, an approach is the use of two-dimensional (2D) materials into a NW network. The challenge here is to simultaneously reduce sheet resistance (R_s) and surface roughness of NWs and additionally improve its mechanical/chemical stability. In particular, graphene materials have been adopted as additional functional material for hybrid structures, either by using chemical vapor deposited (CVD) graphene[4] or reduced graphene oxide (rGO).[5] However, CVD graphene is not readily scalable and the troublesome transfer process can harm the underlying network.[6] Apart from the harsh production conditions and low electrical properties, rGO sheets are not effective in reducing resistance and roughness of the bottom layer without excessively sacrificing the transparency of the film.[7]

In this chapter, we demonstrate a mixed-dimensional structure (1D-2D) using AgNWs and electrochemical exfoliated graphene (EG) as components. EG has excellent solution-processability, large lateral dimensions, and remarkable electronic properties,[8] which are ideal to eliminate the limitations of AgNWs network. After the addition of EG, R_s of

AgNWs dramatically decreases by 83%, and the roughness (RMS) reduces from 16.4 to 4.6 nm. In addition, EG layer renders AgNWs-network stable under mechanical stress and prevents it from oxygen degradation. To demonstrate the feasibility of our work, we have implemented our developed transparent conductor as anode in OSCs and polymer LEDs (PLEDs). OSCs based on our TCE output remarkable power conversion efficiency (PCE) of 6.57%, using PTB7:PCBM blend as active material, and PLEDs yield great external quantum efficiency (EQE) of 4.4%, using 87 nm of Super Yellow PPV as emissive layer, similar to the commercial ITO-based counterparts.

3.2 Results and Discussion

AgNWs dispersion with purity of 99.5% was purchased from ACS Materials. The diameter of the AgNWs is 40 nm and the length between 20 and 30 µm (Figure 3.1a). High-quality graphene was synthesized by electrochemical exfoliation of graphite (Figure 3.1b) which was described in our previous study.[9] In brief, to conduct the exfoliation process, alternating currents (±10 V, 0.1 Hz) were applied between two graphite electrodes inside an aqueous solution of ammonium sulfate (0.1 M).

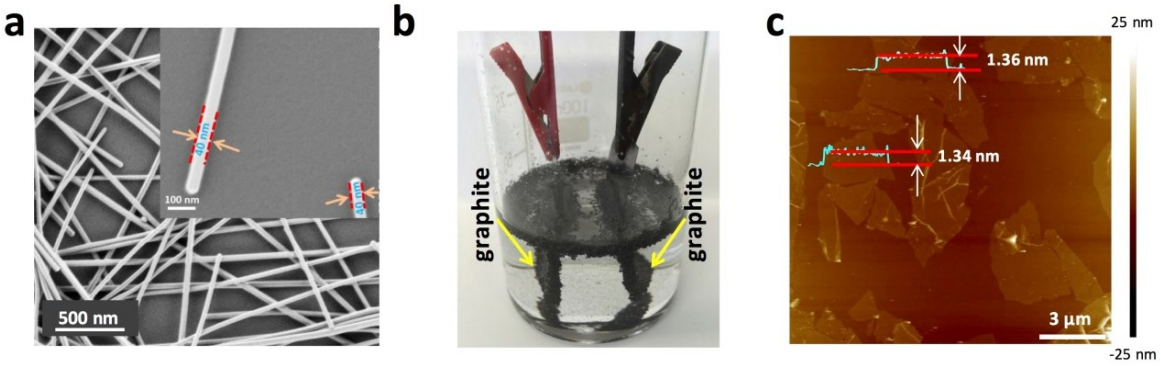

Figure 3.1 a) SEM image of AgNWs on SiO_2 substrate. The inset shows the NW diameter of 40 nm b) optical image of electrochemical exfoliation of graphite c) AFM image of exfoliated graphene on SiO_2.

The as-synthesized EG was transferred on SiO_2 substrates by Langmuir-Blodgett technique to carry out atomic force microscopy (AFM) on the 2D nanosheets (Figure 3.1c). The topographical profile revealed an average thickness of 1.34 nm for an EG sheet, consistent with the thickness of a double-layer graphene flake on Si/SiO_2 wafer.[10] The thickness distribution on 100 EG flakes obtained by cross-sectional analysis shows that 85% of graphene sheets are between one and three layers thick. (Figure 3.2a). Moreover, based on the analysis of 100 EG sheets, approximately 88% of the lateral dimensions are between 1 and 10 μm (Figures 3.2b and 3.2c).

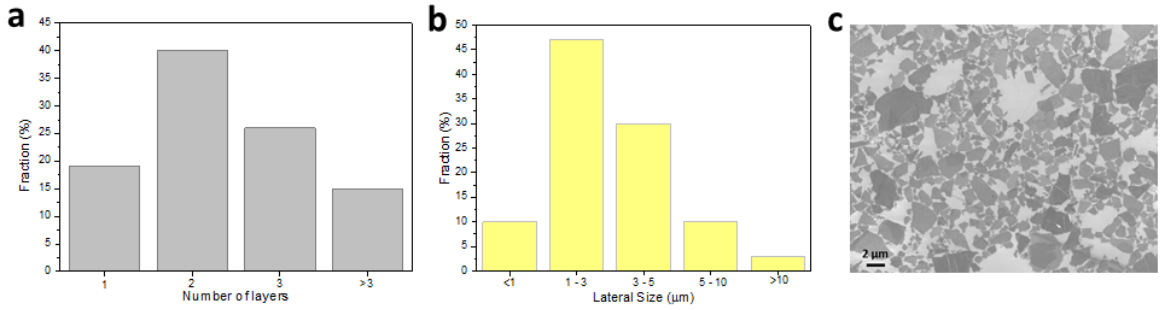

Figure 3.2 a) Thickness distribution of EG flakes from AFM analysis on randomly selected 100 flakes. b) Statistical analysis of EG flake sizes from c) SEM image.

Selected-area electron diffraction (SAED) pattern from transmission electron microscopy (TEM) image exhibits typical 6-fold symmetry (Figure 3.3a), as an evidence of high crystallinity.[11] Raman spectroscopy on EG sheets (Figure 3.3b) revealed that the intensity of the G band (1586 cm^{-1}) is about three times higher than the D band (1360 cm^{-1}).[12] The derived I_D/I_G value, 0.35, is much lower than that of rGO, typically in the range of 1.1-1.5.[13] As a further support of high-quality of EG, X-ray photoelectron spectroscopy (XPS) on EG has shown a low 4.9 atom % oxygen content (Figure 3.3c) and a high carbon to oxygen ratio (C/O) of 19.4. The high-resolution spectrum of C 1s peak (Figure 3.3d) discloses three major peaks at 284.4 eV, 285.3 eV and 287.1 eV, corresponding to the C=C, C-OH and C=O bonds, respectively.[14] For application as transparent electrode, the structural integrity is very important, since it shows direct connection to the device performances. For this reason high-quality EG graphene is selected for our work as compared to rGO.

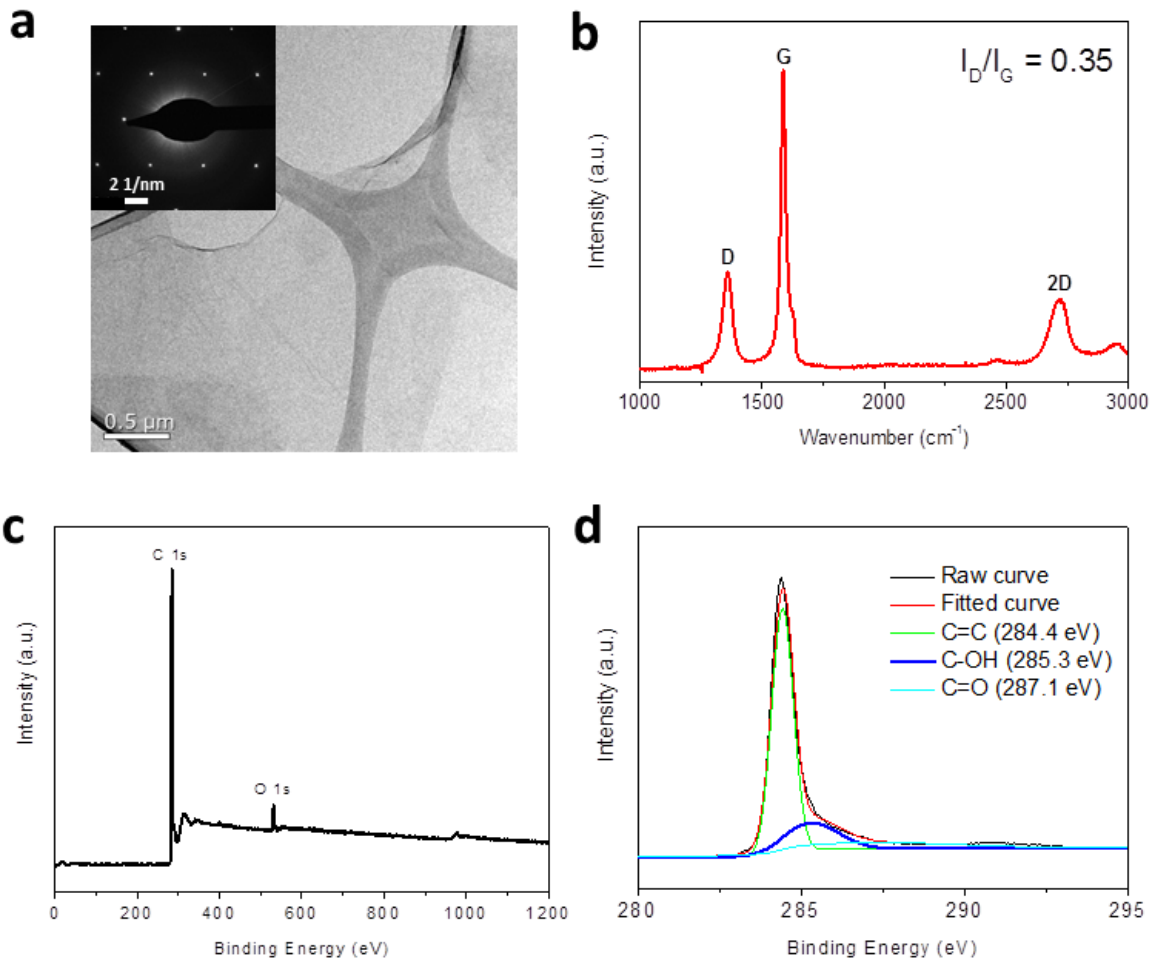

Figure 3.3 a) TEM image of graphene sheet (inset, typical SAED pattern) b) Raman spectrum of EG, c) XPS survey spectrum of EG and d) high-resolution XPS of C 1s spectrum of a thin EG film.

AgNW network was fabricated by spray coating from diluted AgNWs dispersion in 2-propanol. Both rigid (e.g. quartz) and flexible substrates (e.g. polyethylene naphtalate, PEN) were studied (Figure 3.4). Spray coating was selected over several deposition techniques because of its versatility upon a variety of substrates and good potential for scaled-up production.[15] Moreover, the morphology of films can be manipulated by fine control of parameters.[16]

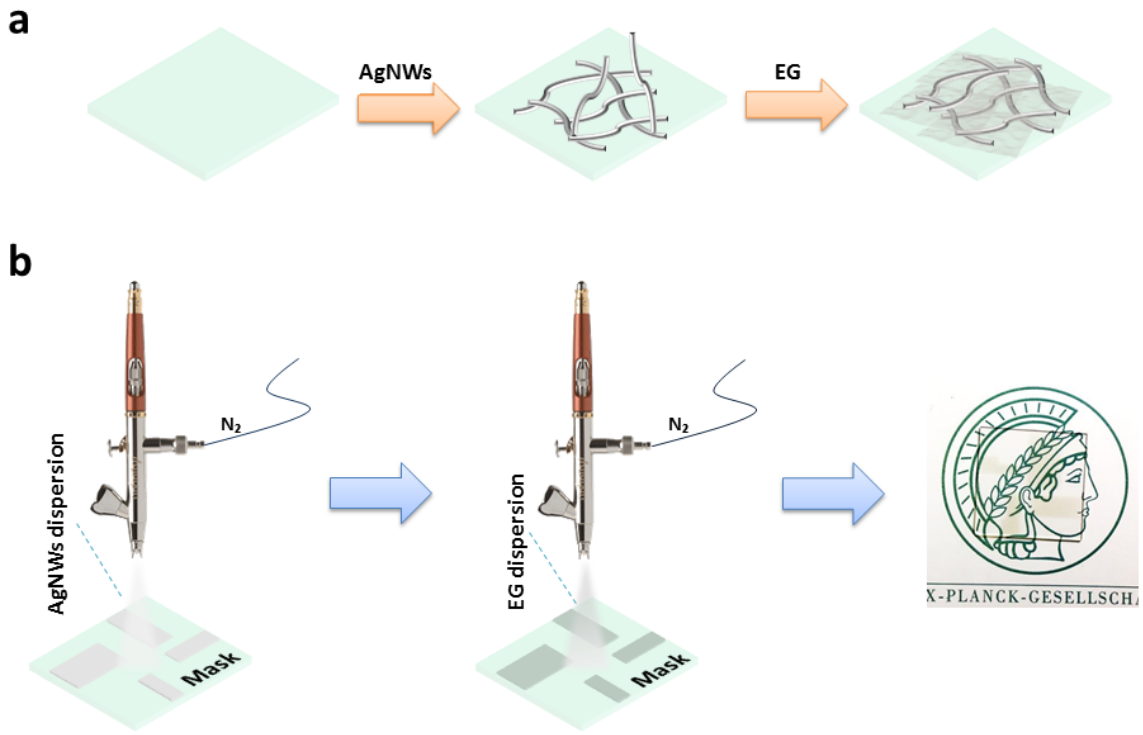

Figure 3.4 a) Schematic representation of the preparation of spray-coated electrodes. b) Schematic illustration of spray coating of AgNWs dispersion, followed by EG dispersions for the hybrid film fabrication.

To determine the optimum conditions, we fabricated films with different concentration of AgNWs dispersion (0.4-1.0 mg mL^{-1}) and spray pressure (1.5-2.8 bar) (Figure 3.5). A uniform coverage of AgNWs film was achieved with a concentration of 0.8 mg mL^{-1} and pressure of 1.8 bar. However, the overlapping AgNWs led to relatively high surface roughness (RMS = 16.4 nm), according to the AFM pictures (Figure 3.6).

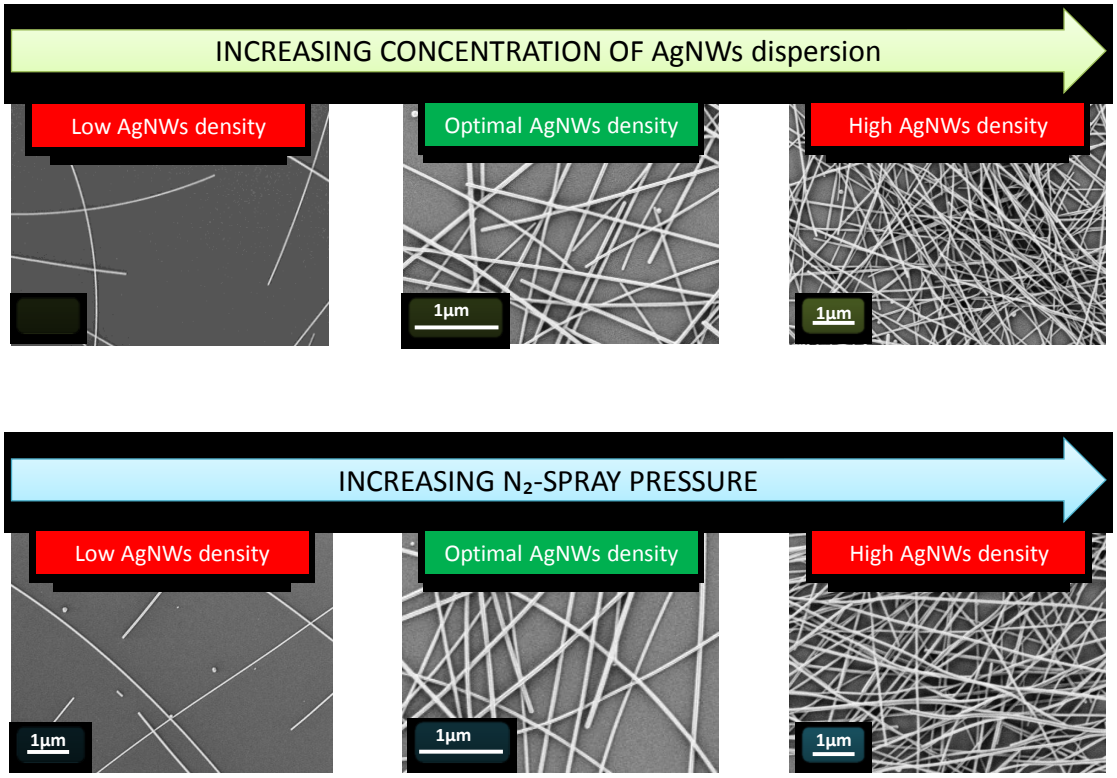

Figure 3.5 SEM images of the AgNWs films with different concentrations of the AgNWs dispersion and spray pressures at a fixed nozzle-to-substrate height of 11 cm. Even coatings have been yielded using AgNWs concentration of 0.6 mg mL^{-1} and spray pressure of 1.8 bar.

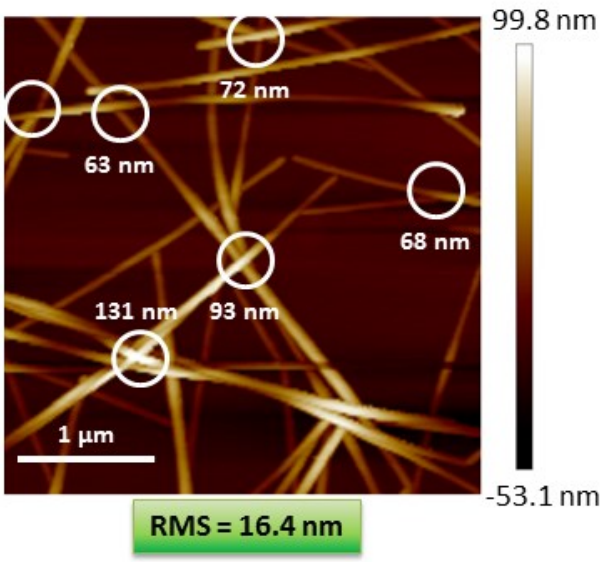

Figure 3.6 AFM image of the AgNWs film.

In order to reduce surface roughness, EG flakes were introduced by spray-coating from a diluted dispersion in *N,N*-dimethylformamide (DMF, 0.05 mg mL^{-1}). In this process, other techniques, such as spin coating and vacuum filtration, are problematic. For instance, spin coating of EG would result in randomly arranged graphene sheets on the top of the AgNWs network (Figure 3.7a), whereas vacuum filtration would leave vacancies and EG bundles, which could protrude up to the upper layers of a vertical device and result in short circuit (Figure 3.7b).

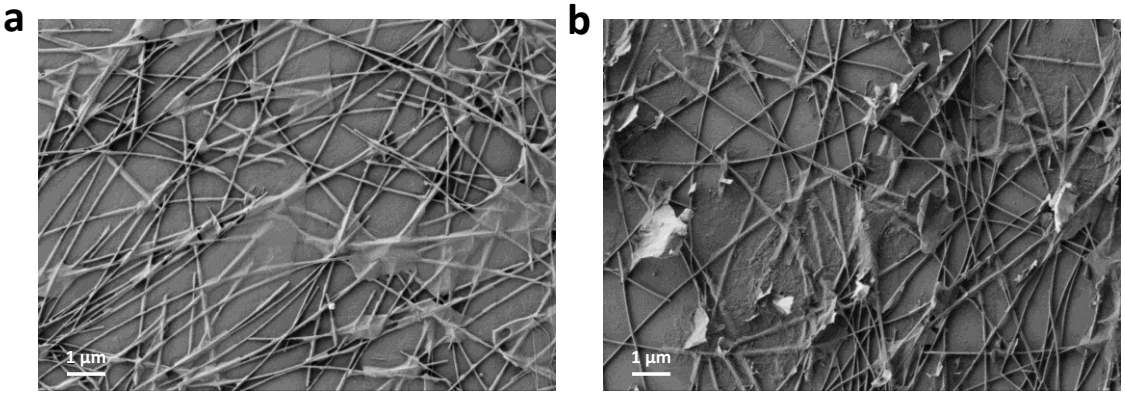

Figure 3.7 SEM images of transferred EG flakes on the top of the AgNWs network a) by spin coating and b) by vacuum filtration.

As predicted, AgNWs junctions and holes between the NWs (cross-sectional SEM images in Figure 3.8a) are completely covered by EG sheets, leading to reduction of surface roughness. AFM analysis performed on AgNWs-EG films reveals an apparent reduction in RMS, compared to bare AgNWs, and a significant decrease of the overlapped NWs height (Figure 3.8b). After coating a uniform layer of EG, the conductivity of the AgNWs network was improved, without sacrificing high transmittance (Figure 3.8c). In particular, the most relevant R_s reduction, from 78 to 13.7 Ω sq^{-1}, is recorded for the 89% transparent AgNWs film (Figure 3.8d). The TCE thickness obtained under these coating conditions of around 50 nm represents the best compromise between series resistance and transparency.

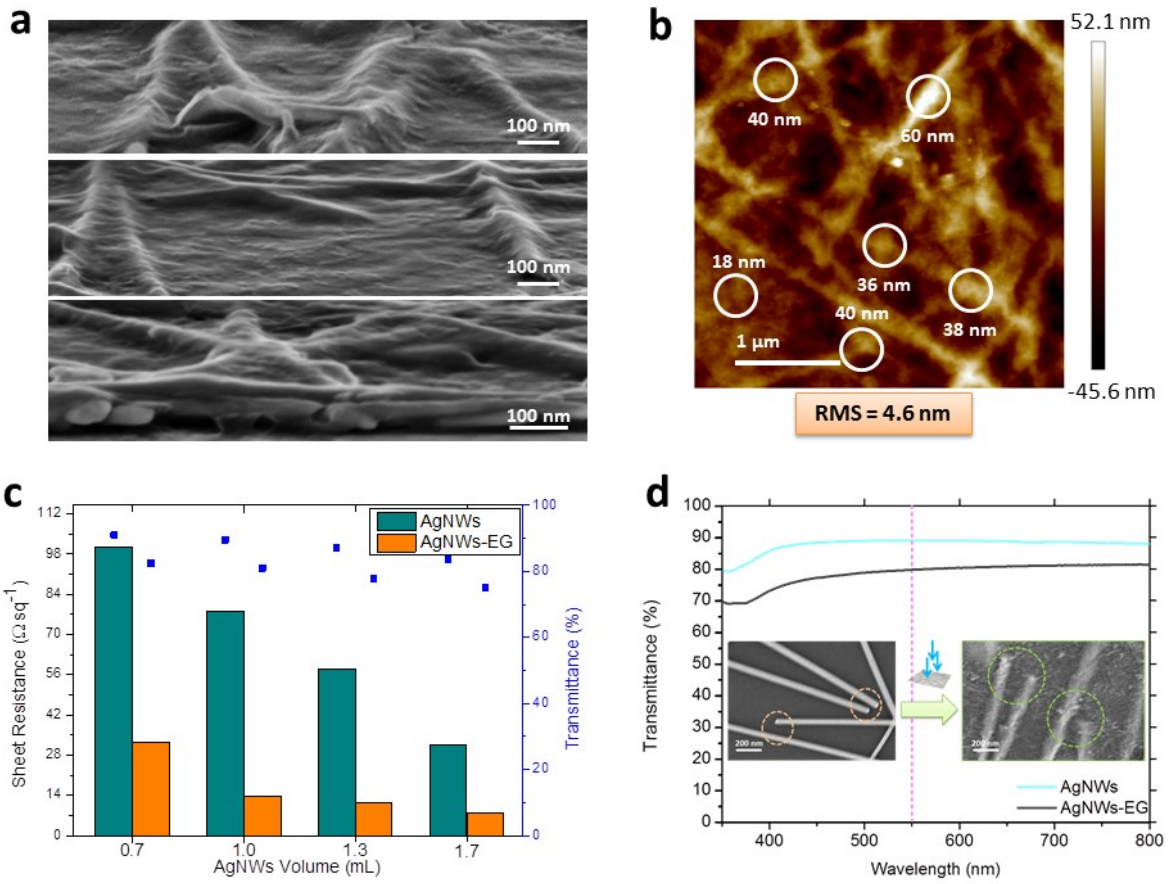

Figure 3.8 b) Cross-sectional SEM images of EG thin layer on the top of the AgNWs network c) AFM image of the AgNWs film after the application of the EG layer d) R_s and transmittance comparison between AgNWs and AgNWs-EG films at different AgNWs loads. d) UV-vis spectra comparison between AgNWs and AgNWs-EG films. As shown by the SEM images in the inset, EG flakes connect the AgNWs, which decrease the R_s of the film.

The hybrid film has strong adhesion on substrate. The adhesion of our electrode was assessed by applying and removing scotch tape over the AgNWs-EG coating on quartz. The scotch tape can not detach the film under mechanical press (Figure 3.9).

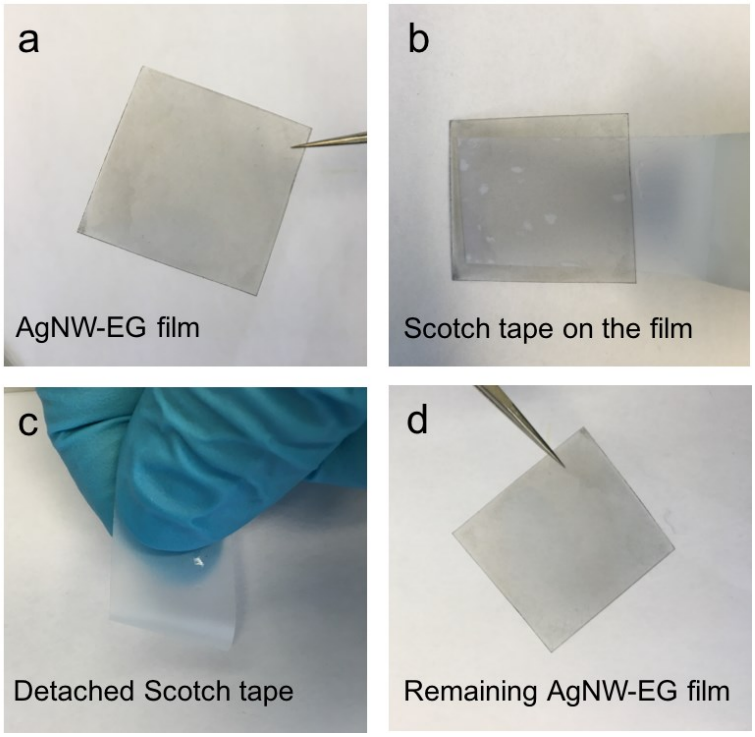

Figure 3.9 Adhesion measurements on the as-prepared hybrid film. The scotch tape is not able to detach the film from the substrate.

As additional benefits, the continuous EG layer helps to improve the mechanical flexibility and oxygen degradation resistance. To validate this, we tested our electrodes to bending stress and air exposure. The R_s of AgNWs-EG on PEN remains almost constant through the bending cycles (Figure 3.10a), with a maximum variation of 25% with respect to the mean value (i.e. 14.6 Ω sq^{-1}), and even at high curving radius (Figures 3.10b). In contrast, the R_s values of pristine AgNWs film tremendously rose from 78 to 222 Ω sq^{-1} with bending cycles and gradually increased at bending angles above 90°. To reveal the chemical stability, TCEs were exposed to air over 120 days. The R_s of the hybrid electrode exhibited negligible variation within the entire duration of air exposure (Figure 3.10c), even at high temperatures the R_s kept constant (Figure 3.10d), thanks to the EG layer that preserved AgNWs from degradation. On the contrary, R_s of the metal NW network rapidly increased after 20 days of exposure to air eventually reached 312 Ω sq^{-1} or from 78 to 129 Ω sq^{-1} after 48 hours heating at 85 °C, as a consequence of the silver oxidation.

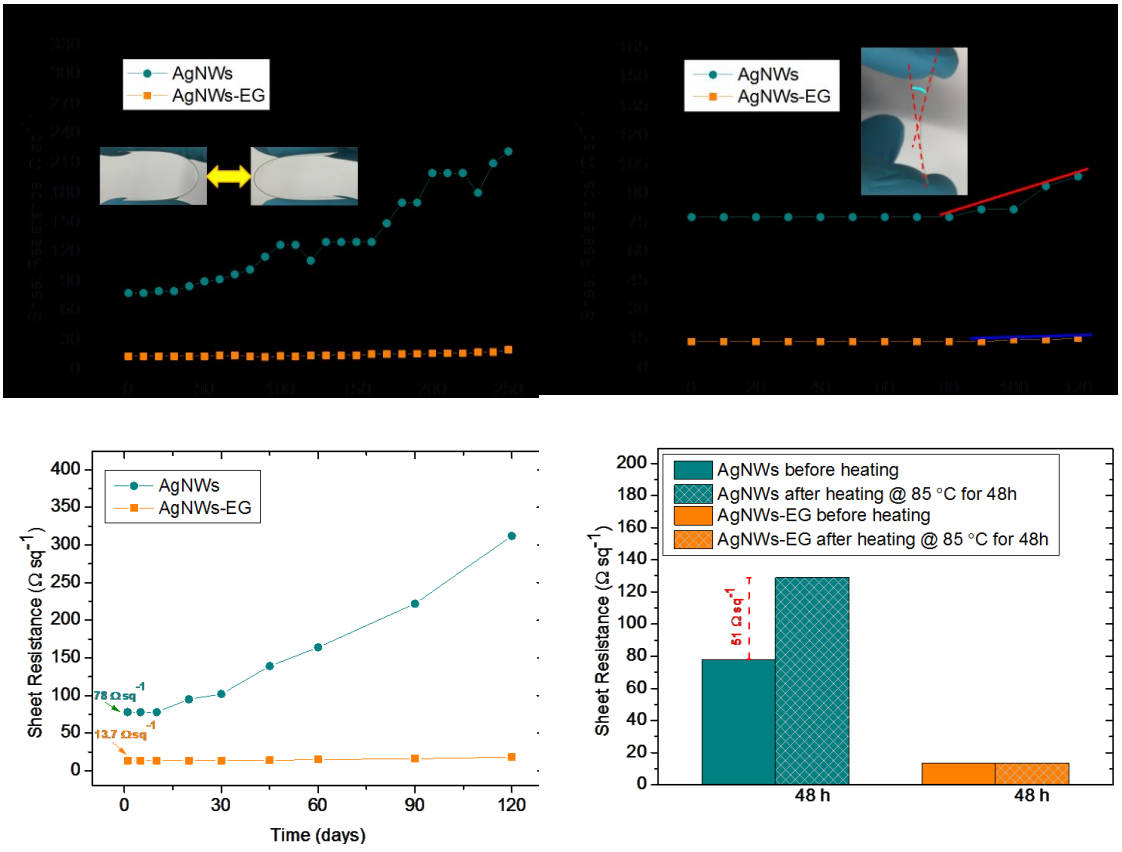

Figure 3.10 R_s response of AgNWs and AgNWs-EG films on PEN substrate to a) different bending cycles, b) bending angles, c) air exposure over a period of 120 days and d) 48 hours at 85 °C.

We evaluated the performances of AgNWs-EG TCE in optoelectronic devices by implementing the hybrid film in OSCs and PLEDs (Figure 3.11a). In both the devices Poly(3,4-ethylenedioxythiophene) polystyrene sulfonate (PEDOT:PSS) was used as hole transport layer (HTL). To ensure a solution-processable homogeneous HTL layer on the top of the hybrid film, a 0.1% of fluorosurfactant (Zonyl™) was added to the PEDOT:PSS[17] because of the mismatch between the hydrophobic and hydrophilic nature of graphene and PEDOT:PSS, respectively. PEDOT:PSS contributes with further planarization of the underlying TCE avoiding any chance of shorts or current leakage paths in the devices.[18] For the solar cell, poly[[4,8-bis[(2-ethylhexyl)oxy]benzo[1,2-b:4,5-b']dithiophene-2,6-diyl][3-fluoro-2-[(2-ethylhexy)carbonyl]thieno[3,4-*b*]thiophenediyl]] (PTB7) and [6,6]-phenyl-C_{71}-butyric acid methyl ester ($PC_{71}BM$) were used as donor and acceptor material (chemical structures in Figures 3.11b and 3.11c),

typically adopted as benchmark active layer in bulk heterojunction (BHJ) OSC.[19] At the top of the architecture, Barium (Ba) and Aluminum (Al) were deposited as cathode (energy band alignment diagram of the devices in Figure 3.12).

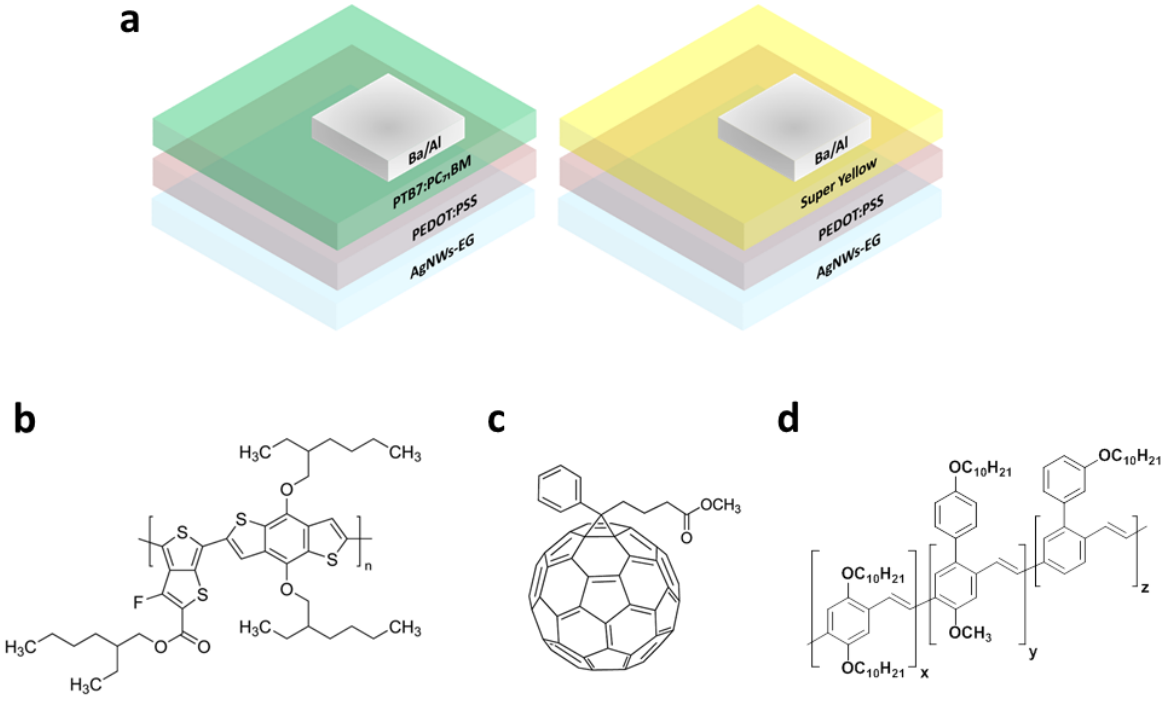

Figure 3.11 a) Schematic illustration of the device architecture for the OSC (left) and PLED (right). Chemical structures of b) PTB7, c) $PC_{71}BM$ and d) Super Yellow PPV.

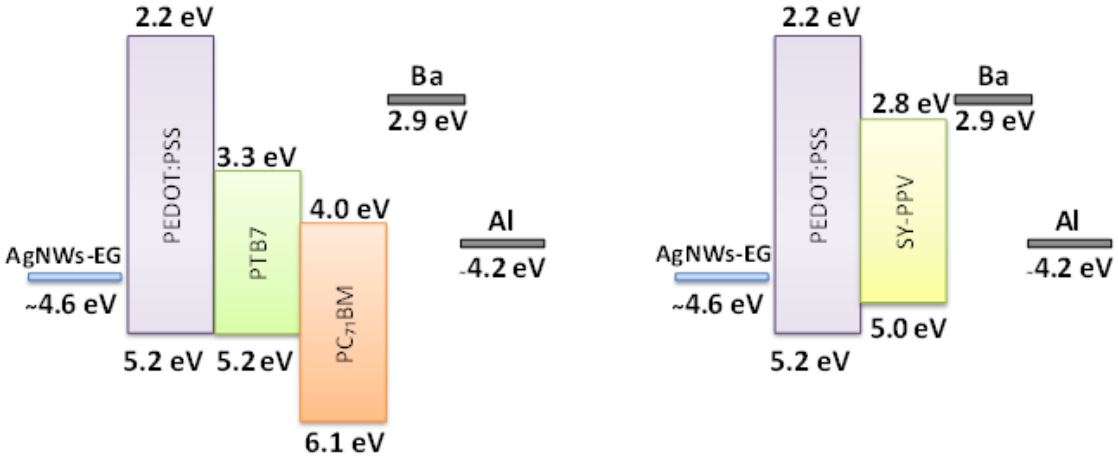

Figure 3.12 Energy band alignment diagrams of solar cells (left) and light emitting diodes (right) used in this work.

The beneficial role of EG coating on the top of AgNWs is evidenced in the performance of the device. While the pristine AgNWs-based devices are shorted, because of high surface roughness and steep heights of the NWs junctions, the OSCs built on the hybrid TCE work properly thanks to the flattening effect of the EG. The optimal AgNWs-EG based OSC measured under 1.5 AMG (100 mW cm^{-2}) conditions, exhibits a short-circuit current density (J_{sc}) of 15.5 mA cm^{-2} with an open-circuit voltage (V_{oc}) of 727 mV and a fill factor (FF) of 58.3, outputting a PCE of 6.57% (Figure 3.13). These values are in line with the results obtained by using commercial ITO TCE on quartz (Table 3.1).

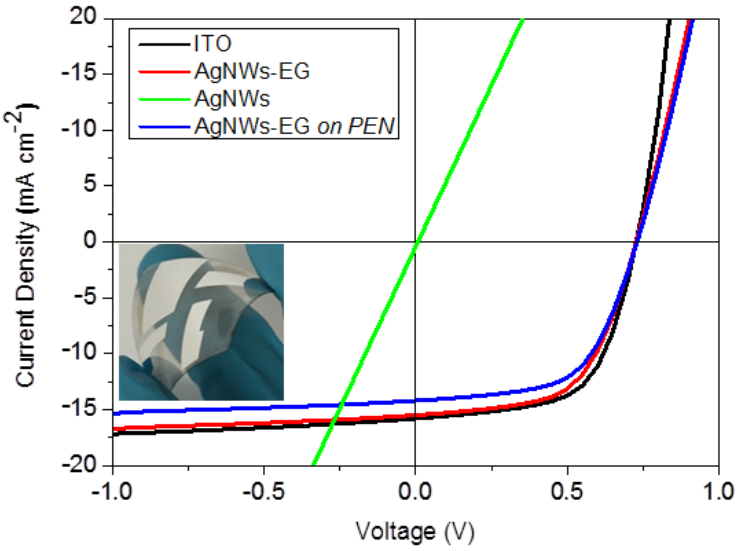

Figure 3.13 *J-V* curves of the OSC devices (inset: flexible AgNWs-EG OSC).

Table 3.1 Photovoltaic parameters of the OSCs based on the AgNWs-EG transparent electrode and ITO reference.

TCE	V_{oc} (mV)	J_{sc} (mA cm^{-2})	FF	PCE (%)
ITO	726	15.8	61.6	7.07
AgNWs-EG	727	15.5	58.3	6.57
AgNWs-EG *on PEN*	730	14.5	58.6	6.18

Notably, our solution-processed transparent conductors exhibit great reproducibility, on the basis of the statistical evaluation of the photovoltaic parameters (Table 3.2). Indeed, the entire set of our devices show almost the same behavior (Figure 3.14).

Table 3.2 Average OSCs parameters with the related standard deviations.

TCE	V_{oc} (mV)	J_{sc} (mA cm^{-2})	FF	PCE (%)
AgNWs-EG	727 ± 3	15.4 ± 0.1	58.3 ± 0.1	6.54 ± 0.04
AgNWs-EG *on PEN*	729 ± 4	14.4 ± 0.1	58.6 ± 0.1	6.11 ± 0.07

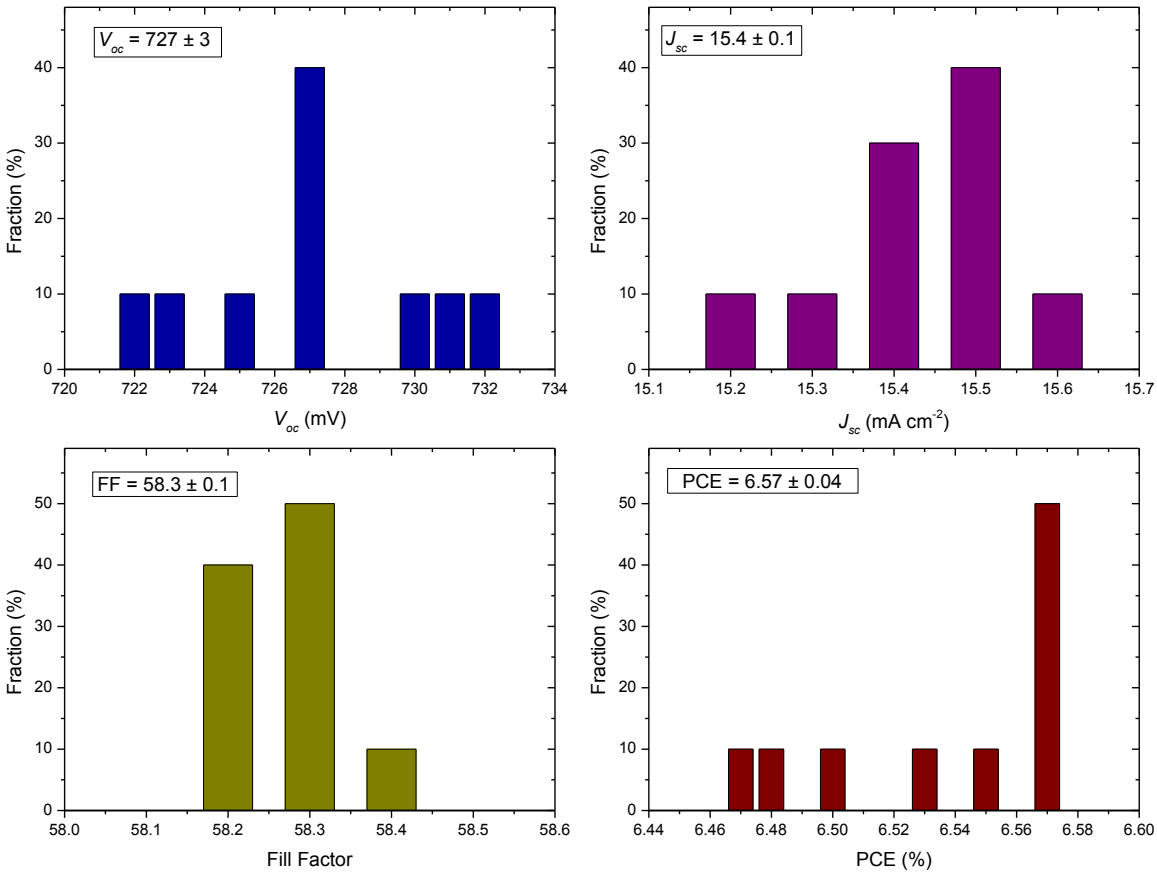

Figure 3.14 Histograms of photovoltaic parameters for AgNWs-EG based OSCs built on glass.

On the top of that, we assessed the feasibility of flexible solar cells based on our bottom electrode. The OSCs built on the flexible PEN substrates reach higher V_{oc} and FF due to the higher affinity of EG to polymeric substrates, which enables a smoother coverage of EG on the top of the AgNWs network, leading to a device with less manufacturing

defects. Hence, the lower PCE (6.18%) is attributable to the lower transparency of PEN (.i.e. 87%), which results in a reduced adsorption of photons with consequent lower photocurrent generation. As presumable from the mechanical tests of the TCEs in Figure 3.10, no changes in photovoltaic parameters are observed upon 250 bending cycles (Figure 3.15), indicating high degree of flexibility.

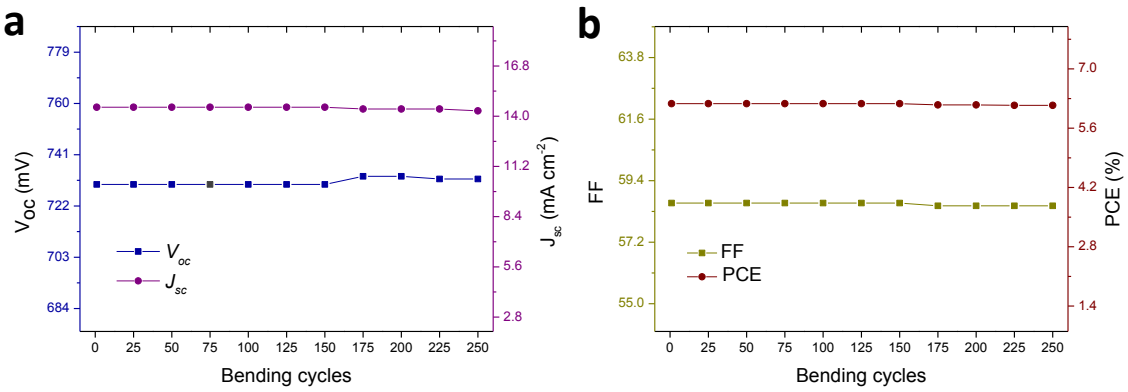

Figure 3.15 Variation of a) V_{oc}, J_{sc} and b) FF, PCE over 250 bending cycles of flexible AgNWs-EG OSCs.

Further, to prove the robustness of our composite transparent electrode, we fabricated PLEDs with AgNWs-EG bottom electrodes. PLEDs are more sensitive to short circuits since they are operated at higher voltages than solar cells, which are typically restricted to a voltage range between -1 V to 1 V. Moreover, the thinner active layer restricts the candidates for alternative TCEs because such device is more sensitive to rough surfaces than OSCs (optimal active layers requires a thickness of 100-250 nm for OSCs, 50-100 nm for PLEDs). As for the fabrication of the solar cells, PEDOT:PSS layer was uniformly spin-coated above the hybrid film on top flexible substrates. Super Yellow PPV (Figure 3.11d), a conjugated copolymer widely used as emissive layer in PLEDs,[20] was spin-coated to give a thickness of only 87 nm, prior to the evaporation of the top electrodes (Ba/Al).

As demonstrated in Figure 3.16a the measured current density and luminance were almost identical to reference PLEDs on conventional glass/ITO substrates. As a result, also the EQE is almost the same, reaching maximum values of 4.7% and 4.4% for ITO and

AgNWs-EG, respectively (Table 3.3). The small difference could be caused by the slightly reduced transmittance in the 550 nm range. The EQE remains over 4% even at high brightness above 10000 cd m^{-2} (Figure 3.16b), demonstrating the robustness and performance of the hybrid electrode. Importantly, no hysteresis is present in the current density-voltage characteristics between forward and reverse bias at high voltages, emphasizing the quality of our TCE against electrical breakdown.

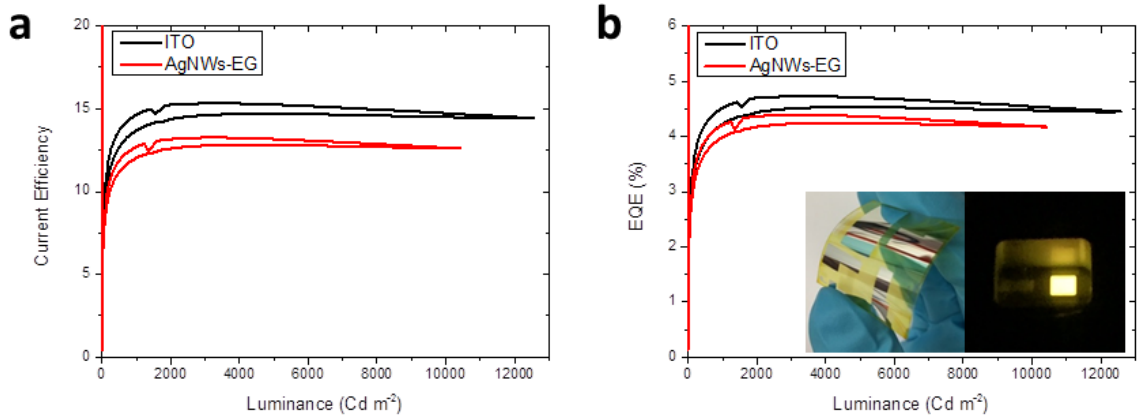

Figure 3.16 a) Current Density-Voltage-Luminance characteristics for PLEDs deposited on ITO (black) and AgNWs-EG (red). Solid and dashed lines display Current Density and Luminance, respectively b) EQE comparison between hybrid film and ITO PLEDs (inset: flexible AgNWs-EG working PLED).

Table 3.3 PLEDs key values for ITO and AgNWs-EG hybrid electrode devices.

TCE	*Current Density* (A m^{-2})	*Luminance* (cd m^{-2})	EQE (%)
ITO	1113	12569	4.7
AgNWs-EG	1057	10425	4.4

These data clearly indicate that our 1D-2D electrode is endowed with all the features of a successful TCE. Moreover, it is important to outline that the transmittance of the AgNWs-

EG electrodes can be further improved by laser patterning techniques[21], which indicates the opportunities for higher performances of the optoelectronic devices.

3.3 Conclusion

In this chapter, we have demonstrated a solution-processable transparent anode for flexible optoelectronic devices based on the integration of 1D and 2D material. The synergy of silver nanowires and electrochemical exfoliated high-quality graphene leads to a transparent conductor with smooth surface and excellent mechanical, chemical and electrical features, which overcomes simultaneously all the limitations of AgNWs-based TCEs. Remarkably, OSC and PLED built on our electrodes exhibit similar behavior to the commercial ITO-based counterparts. We believe that this study provides an exciting and solid platform for the future of ubiquitous optoelectronic applications.

Experimental Session

Graphite Exfoliation. Graphite exfoliation was carried out in a two-electrode system, where commercial graphite (Alfa Aesar) foils were used as working anode and counter electrode. The electrodes were placed in parallel at a distance of 1.5 cm. The electrolyte for the exfoliation was obtained by dispersing ammonium sulfate crystals in DI water, affording a 0.1 M solution. Hence, the electrodes were immersed in the electrolyte and an alternating current (±10 V, 0.1 Hz) was applied to trigger the electrochemical exfoliation. To avoid over-heating, the entire process was kept in an ice bath. Once the exfoliation was finished, the suspended graphene sheets were collected with a 0.2 μm PTFE membrane filter (Sartorius™) and washed three times by DI water and ethanol to remove any residue. Then, the wet graphene was dispersed in *N,N*-dimethylformamide (DMF) via mild sonication in an ice bath for 15 minutes.

Purification of graphene. The graphene dispersion was centrifuged to separate out any un-exfoliated flakes and large particles. The solution was transferred in plastic tubes and centrifuged twice at 5000 rpm for 45 minutes. Afterwards, the supernatant was taken out from the suspension and sonicated for 15 minutes to ensure homogeneity.

Preparation of AgNWs-EG transparent electrodes. Hybrid films were prepared on both glass and PEN (Pütz GMBH + Co. Folien KG) by spray-coating through an Infinity CRplus airbrush (Harder & Steenbeck GmbH). AgNWs solution in IPA (ACS Materials) was diluted and sprayed onto 3x3 cm^2 pre-heated substrates under a N_2-assisted inlet pressure of 1.8 bar. The distance between the nozzle and the substrate was fixed at 11 cm. Subsequently, EG dispersion was sprayed on the top of the NWs network under a N_2 pressure of 2.1 bar and at a noozle-to-substrate distance of 13 cm, to ensure a uniform coverage. The as-coated hybrid films were heated at 90 °C overnight in a vacuum oven to remove residual solvent before use.

Photovoltaic device fabrication. Zonyl™ fluorosurfactant with a concentration of 0.1% v/v was added in an aqueous solution of PEDOT:PSS (Clevios P VP Al4083, Heraeus Precious Metals GmbH & Co.) to obtain proper wetting which matches the AgNWs-EG hydrophobic surface nature. The mixture was stirred overnight and spin-coated on top of the patterned electrodes at 2000 rpm for 60 s. The films were then heated at 140 °C for 5 minutes and transferred in a glove-box for the coating of the PTB7:$PC_{71}BM$ photoactive layer. The PTB7:$PC_{71}BM$ blend was prepared in a mixed solvent of chlorobenzene and 1,8-diiodoctane (DIO) at a 97:3 ratio. PTB7 (10 mg) and $PC_{71}BM$ (15 mg) were initially dissolved in CB (0.97 mL). The solution was left stirring overnight at 80 °C. Aftewards, DIO (30 μL) was added and the solution stirred 30 minutes at 70 °C. The blend solution was then spin-coated on the top of PEDOT:PSS layer at 1500 rpm for 60 s. Ba (5 nm) and Al (100 nm) were used as top electrodes, which were deposited by vacuum thermal evaporation.

Organic light-emitting diode fabrication. Super Yellow PPV (PDY-132, Merck) was used as emissive layer for the OLED. A 5 mg mL^{-1} solution of Super Yellow in toluene was left stirring overnight at 60 °C in the glove-box and filtered with a PTFE filter before the deposition on the top of the PEDOT:PSS layer. The spin-coating of Super Yellow was carried out through two step (100 rpm for 3 s followed by 1000 rpm for 60 s) to output a uniform thickness of 87 nm. PEDOT:PSS layer and top electrodes were processed as previously described for the OSC.

Characterizations. Current-Voltage (*J-V*) characteristics were measured by a software controlled source meter (Keithley 2400) at room temperature with a 1.5 AMG (100 mW/cm^2) solar simulator. OLED performances were tested with an in-house photodiode and a software controlled source meter (Keithley 2400). Sheet resistance measurements were performed by using a four-point probe system with a Keithley 2700 Multimeter (probe spacing: 0.635 mm, Rs= 4.5324 V/I). AFM measurements were carried out on a Digital Instruments Dimension 3100. SEM images were obtained using a field-emission scanning electron microscope (Gemini 1530 LEO). TEM and SAED were carried out using a transmission electron microscope (Philips Tecnai F20). Raman spectroscopy

measurments were performed with a Bruker RFS 100/S spectrometer (laser wavelength of 532 nm). UV-vis spectroscopy was executed on Perkin Elmer Lambda 900 spectrometer with diffusive mode. XPS analysis was carried out on a PHI–5000C ESCA system with a monochromatic Mg Kα X-ray source ($h\nu$ = 1253.6 eV), the C 1s value was set at 284.7 eV for charge corrections.

References

[1] a) J. Krantz, M. Richter, S. Spallek, E. Spiecker, C. J. Brabec, *Advanced Functional Materials* **2011**, 21, 4784; b) B. Sciacca, J. van de Groep, A. Polman, E. C. Garnett, *Advanced Materials* **2016**, 28, 905.

[2] S. Han, S. Hong, J. Ham, J. Yeo, J. Lee, B. Kang, P. Lee, J. Kwon, S. S. Lee, M. Y. Yang, S. H. Ko, *Advanced Materials* **2014**, 26, 5808.

[3] W. W. Xiong, H. L. Liu, Y. Z. Chen, M. L. Zheng, Y. Y. Zhao, X. B. Kong, Y. Wang, X. Q. Zhang, X. Y. Kong, P. F. Wang, L. Jiang, *Advanced Materials* **2016**, 28, 7167.

[4] a) Y. Liu, Q. H. Chang, L. Huang, *Journal of Materials Chemistry C* **2013**, 1, 2970; b) R. Y. Chen, S. R. Das, C. Jeong, M. R. Khan, D. B. Janes, M. A. Alam, *Advanced Functional Materials* **2013**, 23, 5150; c) T. H. Seo, S. Lee, K. H. Min, S. Chandramohan, A. H. Park, G. H. Lee, M. Park, E. K. Suh, M. J. Kim, *Sci Rep* **2016**, 6, 8.

[5] a) J. J. Liang, L. Li, K. Tong, Z. Ren, W. Hu, X. F. Niu, Y. S. Chen, Q. B. Pei, *ACS Nano* **2014**, 8, 1590; b) B. Hwang, M. Park, T. Kim, S. M. Han, *RSC Adv.* **2016**, 6, 67389.

[6] L. B. Gao, G. X. Ni, Y. P. Liu, B. Liu, A. H. C. Neto, K. P. Loh, *Nature* **2014**, 505, 190.

[7] Z. L. Luo, Z. P. Cai, Y. B. Wang, Y. P. Wang, B. B. Wang, *RSC Adv.* **2016**, 6, 37124.

[8] S. Yang, S. Bruller, Z. S. Wu, Z. Y. Liu, K. Parvez, R. H. Dong, F. Richard, P. Samori, X. L. Feng, K. Mullen, *J. Am. Chem. Soc.* **2015**, 137, 13927.

[9] S. Yang, A. G. Ricciardulli, S. Liu, R. Dong, M. R. Lohe, A. Becker, M. A. Squillaci, P. Samori, K. Mullen, X. Feng, *Angew. Chem.-Int. Edit.* **2017**, 56, 6669.

[10] M. Biswal, X. Zhang, D. Schilter, T. K. Lee, D. Y. Hwang, M. Saxena, S. H. Lee, S. S. Chen, S. K. Kwak, C. W. Bielawski, W. S. Bacsa, R. S. Ruoff, *J. Am. Chem. Soc.* **2017**, 139, 4202.

[11] S. Lin, L. Dong, J. J. Zhang, H. B. Lu, *Chemistry of Materials* **2016**, 28, 2138.

[12] I. A. Verzhbitskiy, M. De Corato, A. Ruini, E. Molinari, A. Narita, Y. Hu, M. G. Schwab, M. Bruna, D. Yoon, S. Milana, X. Feng, K. Mullen, A. C. Ferrari, C. Casiraghi, D. Prezzi, *Nano Lett.* **2016**, 16, 3442.

[13] S. J. Peng, X. P. Han, L. L. Li, Z. Q. Zhu, F. Y. Cheng, M. Srinivansan, S. Adams, S. Ramakrishna, *Small* **2016**, 12, 1359.

[14] Z. Y. Liu, Z. S. Wu, S. Yang, R. H. Dong, X. L. Feng, K. Mullen, *Advanced Materials* **2016**, 28, 2217.

[15] A. G. Ricciardulli, S. Yang, X. L. Feng, P. W. M. Blom, *ACS Appl. Mater. Interfaces* **2017**, 9, 25412.

[16] R. Garg, S. Elmas, T. Nann, M. R. Andersson, *Adv. Energy Mater.* **2017**, 7, 22.

[17] M. Vosgueritchian, D. J. Lipomi, Z. A. Bao, *Adv. Funct. Mater.* **2012**, 22, 421.

[18] E. L. Williams, K. Haavisto, J. Li, G. E. Jabbour, *Advanced Materials* **2007**, 19, 197.

[19] a) C. Stelling, C. R. Singh, M. Karg, T. A. F. Koenig, M. Thelakkat, M. Retsch, *Sci Rep* **2017**, 7; b) I. Jeon, K. Cui, T. Chiba, A. Anisimov, A. G. Nasibulin, E. I. Kauppinen, S. Maruyama, Y. Matsuo, *J. Am. Chem. Soc.* **2015**, 137, 7982; c) H. Park, S. Chang, X. Zhou, J. Kong, T. Palacios, S. Gradecak, *Nano Lett.* **2014**, 14, 5148.

[20] a) Y. H. Kim, T. H. Han, H. Cho, S. Y. Min, C. L. Lee, T. W. Lee, *Advanced Functional Materials* **2014**, 24, 3808; b) S. Burns, J. MacLeod, D. Thu Trang, P. Sonar, S. D. Yambem, *Sci Rep* **2017**, 7.

[21] a) D. Paeng, J. H. Yoo, J. Yeo, D. Lee, E. Kim, S. H. Ko, C. P. Grigoropoulos, *Advanced Materials* **2015**, 27, 2762; b) D. Konios, C. Petridis, G. Kakavelakis, M. Sygletou, K. Savva, E. Stratakis, E. Kymakis, *Adv. Funct. Mater.* **2015**, 25, 2213.

The content of this chapter has been published in:
Advanced Functional Materials (*Adv. Funct. Mater.*, **2018**, *28*, 1706010)
Hybrid Silver Nanowire and Graphene-Based Solution-Processed Transparent Electrode for Organic Optoelectronics
Antonio Gaetano Ricciardulli, Sheng Yang, Gert-Jan A. H. Wetzelaer, Xinliang Feng, Paul W. M. Blom*

Chapter 4 Improved Hole Injection into Perovskite Light-Emitting Diode Using a Black Phosphorus Interlayer

4.1 Introduction

All-inorganic perovskite, such as cesium lead trihalide ($CsPbX_3$, where X = Cl, Br, I), has gained much attention in a variety of optoelectronic devices,[1] including light-emitting diodes (LEDs).[2] $CsPbX_3$ is considered a promising light-emitting material due to its facile solution processability, cost effectiveness, thermal stability and high photoluminescence quantum efficiency (>90%) with narrow spectral width.[3] However, the reported external quantum efficiency (EQE) of perovskite based light-emitting diodes (PeLEDs) have been relatively modest, ranging from 0.008% to 1.37% for devices using pristine polycrystalline $CsPbX_3$ as emissive layer.[2a, 4] Improvements have been made due to the progress of metal halide synthetic routes with formation of perovskite nanocrystals[5] and post-treatment techniques on the perovskite film (i.e. vapor annealing, crosslinking)[6].

A remaining fundamental problem is that inorganic semiconducting perovskites as the green-emitting $CsPbBr_3$ have a large ionization potential, with the valence band (VB) typically located at 5.6 eV below vacuum. In solution-processed optoelectronic devices poly(3,4-ethylenedioxythiophene) polystyrene sulfonate (PEDOT:PSS) is used as the conventional hole-injecting layer (HIL). Since PEDOT:PSS has a work function (WF) only close to 5.0 eV,[7] large hole injection barriers exist in LEDs based on active materials with deeper energy levels as $CsPbBr_3$.[8] Since the magnitude of the injected current exponentially depends on the injection barrier,[9] the performance of $CsPbBr_3$-based LEDs with a PEDOT:PSS anode are radically affected by the huge mismatch (~0.6 eV) between the WF of PEDOT:PSS and VB of $CsPbBr_3$.[4] To overcome this challenge many strategies have been explored, including the use of a self-organized buffer HIL[4, 5b] or a complex inverted structure.[10] However, the materials used in these methods, like perfluorinated ionomers (PFI) or metal oxides, can easily form aggregates and yield to wettability problems with the subsequent deposited perovskite layer, leading to electrical

shorts and power losses. Summarizing, PeLED performance is in general hindered by limited hole injection and non-radiative losses, resulting from shunt paths in uneven and discontinuous perovskite films.

An alternative approach would be the application of two-dimensional (2D) materials, including graphene oxide and transition metal dichalcogenides as hole injecting layer. 2D materials have been demonstrated as suitable solution-processable interlayers for organic optoelectronic devices.[11] Among them, black phosphorus (BP), a newly emerged 2D layered semiconductor with high charge-carrier mobility[12] and exceptional optical/phonon properties[13], represents a suitable candidate for lowering the injection barrier between PEDOT:PSS and $CsPbBr_3$. Thin-layered BP has a HOMO level of 5.32 eV,[14] which would lower the injection barrier by 0.3 eV. Recently, BP has been adopted as an interlayer in both organic and perovskite solar cells (SCs),[15] delivering a slight enhancement (10-15%) of their power conversion efficiencies. However, the BP sheets used in these works have limited lateral sizes (< 200 nm) and abundancy of defects, due to the harsh and prolonged liquid-phase sonication.[16] This inevitably leads to a scarce coverage of BP with inferior electronic properties, thereby limiting the beneficial effects.

In this work, large and ultra-thin BP flakes with fewer defects are synthesized by electrochemical exfoliation of bulk BP. Based on a facile suction filtration, continuous and uniform 2D layers have been successfully fabricated and integrated as HIL in $CsPbBr_3$-based PeLEDs. The uniformity of the BP layer resulted in a homogeneous growth of pin-holes free perovskite, without the necessity of further treatment steps (i.e. vapor annealing, crosslinking). Electrical characterization confirms that the hole injection barrier is decreased, and an EQE of 2.8% at 20000 cd m^{-2} was achieved for $CsPbBr_3$-based PeLEDs.

4.2 Results and Discussion

High-quality BP was synthesized by electrochemical delamination of bulk BP (Figure 4.1), which was outlined in our previous work.[17] Briefly, BP sheets were formed upon the application of a bias (-8.0 V) between bulk BP and platinum foil, working and counter

electrode, respectively. The two-electrode system was placed into a propylene carbonate solution of tetra-*n*-butyl-ammonium bisulfate (0.1 M), which served as electrolyte.

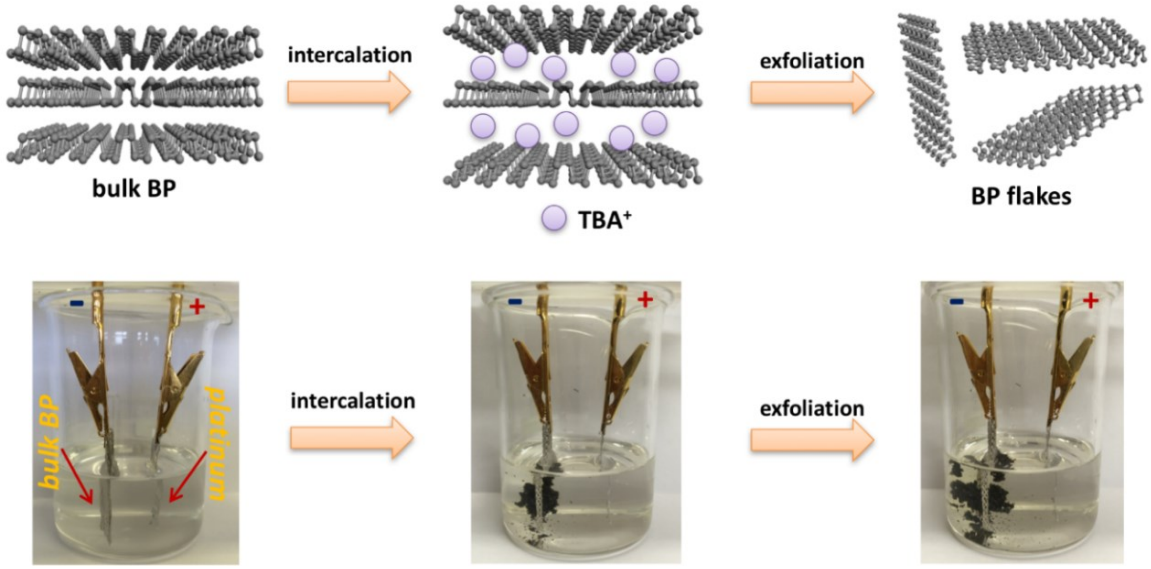

Figure 4.1 Schematic illustration (top) and optical images (bottom) of BP delamination process.

As-synthesized BP flakes were dispersed in propan-2-ol (IPA), resulting in a stable dispersion, which showed a broad absorption across the ultraviolet (UV) to near-infrared (NIR) regions (Figure 4.2a). Atomic force microscopy (AFM) revealed the ultra-thin morphology of the BP sheets (Figure 4.2b). The thickness distribution on randomly selected BP flakes obtained by cross-sectional analysis suggests that the BP sheets are mainly thinner than 4 layers (Figure 4.2c). The morphology of the sheets was further investigated by scanning electron microscopy (SEM) and transmission electron microscopy (TEM). Figure 4.2d and 4.2e displayed, respectively, the typical SEM and TEM images of BP flakes with large lateral sizes. The statistical calculation from SEM analysis (Figure 4.2f) reveals a broad distribution of BP sheets with wide lateral sizes (75% between 1 and 10 μm), which constitutes a crucial prerequisite for film formation.

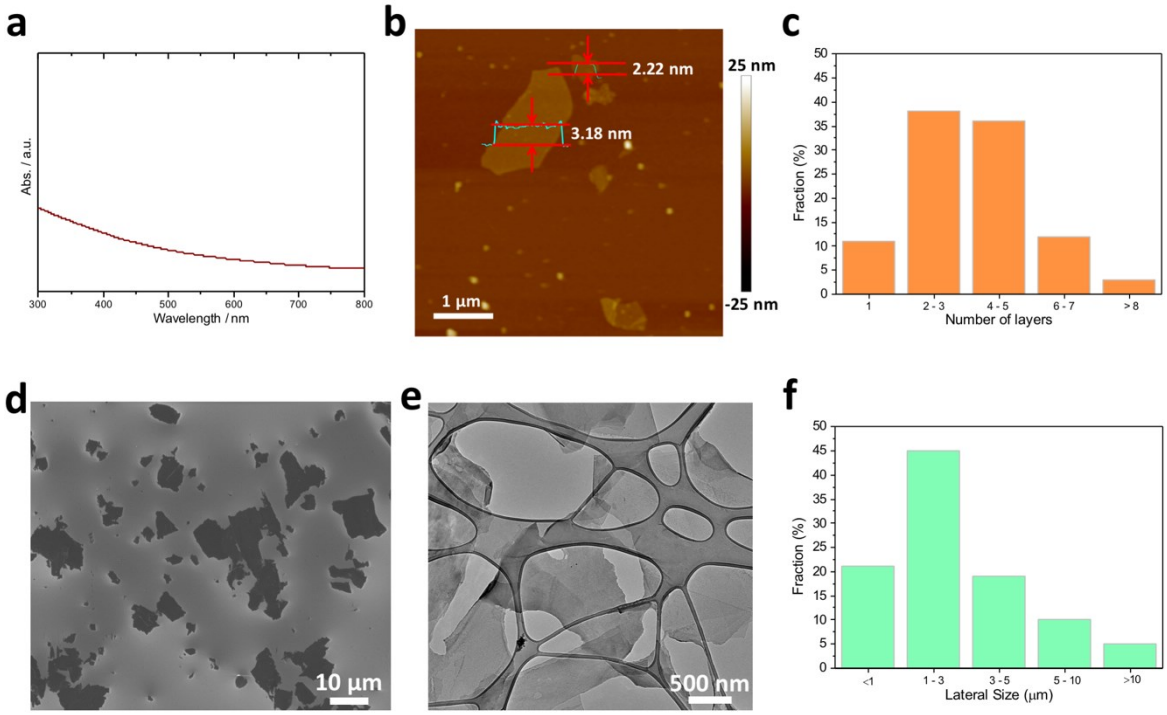

Figure 4.2 a) Absorption spectrum of BP dispersion in IPA. b) AFM image of delaminated BP on Si/SiO_2. c) Thickness distribution of BP sheets from AFM analysis on randomly selected flakes. c) SEM image of delaminated BP on Si/SiO_2. d) TEM image of thin BP sheets on lacey carbon grid. f) Statistical calculation of BP flakes from SEM analysis.

Thin BP films were fabricated by suction filtration as illustrated in Figure 4.3. First *N,N*-Dimethylformamide (DMF) was added to the dispersion to allow ambient condition processing and preserve BP film from oxidation. By using a high boiling point solvent, like DMF, the protection of the film is ensured by the solvation shell remaining even after solvent removal.[18] Additionally, to further decrease the probability of BP deterioration, a hydrophobic polytetrafluorethylene (PTFE) membrane was employed for suction filtration. Unlike hydrophilic filters, PTFE is not wetted by air humidity. The BP film was formed on the top of PTFE by filtrating the BP dispersion through the membrane. Afterwards, the film was transferred onto the substrate by a mechanical press. It is worth noting that the use of a high boiling solvent does not only preserve the BP dispersion from degradation but it forms also a wet passivating shield for the as-fabricated film,[19] which makes further treatments in ambient conditions possible.

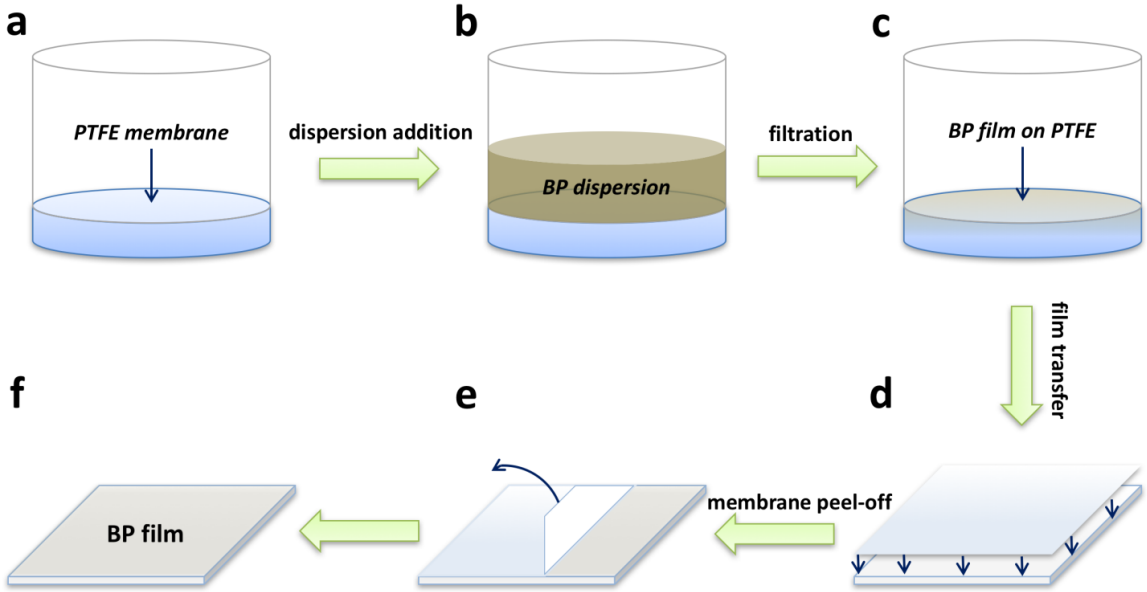

Figure 4.3 Schematic illustration of the fabrication of BP film. The fabrication process includes a) addition of BP dispersion on the top of a PTFE membrane, b) vacuum-assisted filtration c) formation of BP film onto PTFE membrane, d) film transfer on top of the substrate, e) membrane removal and f) BP film transfer from PTFE to the substrate.

Moreover, the transmittance of the BP film is tunable on the basis of the volume/concentration of the BP dispersion (Figure 4.4).

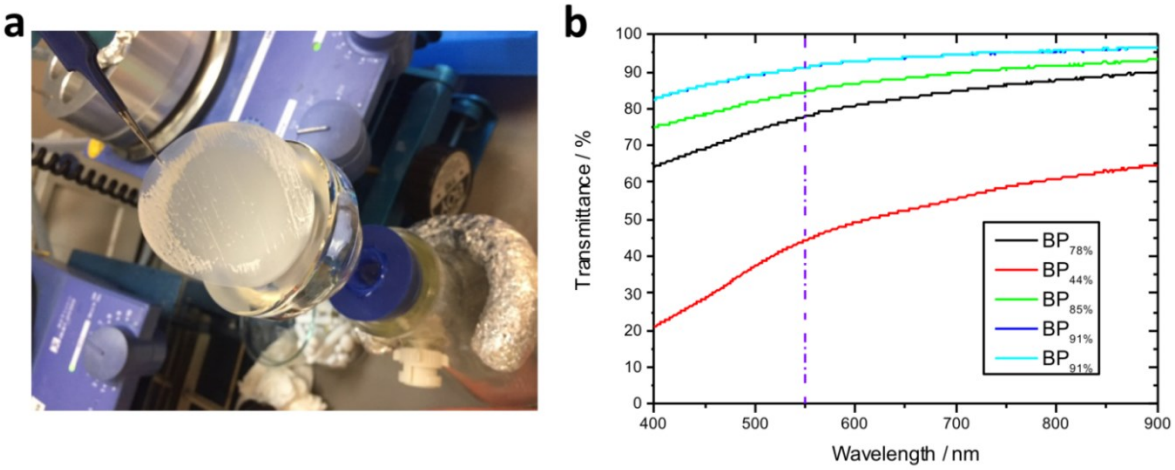

Figure 4.4. a) Optical image of BP film on top of PTFE membrane b) UV-vis spectra of BP films at different transmittance values. Transparency can be easily tuned by changing BP dispersion load.

Raman spectrum of BP film (Figure 4.5a) displayed three typical phonon modes observed at 363 cm^{-1} (A_g^1), 440 cm^{-1} (B_{2g}) and 468 cm^{-1} (A_g^2).[20] To determine phosphorene degradation caused by oxygen, derived A_g^1/ A_g^2 values are calculated, for instance, higher than 0.20 are typical for low oxidized BP sheets.[21] Pristine films produced with our method exhibited A_g^1/ A_g^2 ratio of 0.86, revealing very limited amount of oxygen degradation. To further verify the structural integrity of BP, X-ray photoelectron spectroscopy (XPS) was carried out. XPS (Figure 4.5b) showed a strong peak at 130 eV, attributed to P 2p of highly crystalline phosphorene,[18] and the weak oxidized phosphorus peak, suggesting the structural integrity of BP.[22]. Hence, the purity of as-synthesized high crystalline BP, as evidenced by high-resolution TEM (HR-TEM) and selected area electron diffraction (SAED) (Figure 4.5c), are preserved during the film formation.

To evaluate the effect of a high-quality BP layer in a PeLED we implemented the 2D thin film as HIL on top of PEDOT:PSS. As mentioned above, thin-layered BP has a reported HOMO level of 5.32 eV,[14] and is therefore expected to reduce the hole injection barrier between PEDOT:PSS and $CsPbBr_3$. The surface topography of the PEDOT:PSS/BP film was examined by AFM and SEM measurements. AFM analysis (Figure 4.5d) revealed a surface roughness (RMS) of ~8.0 nm for the BP layer. SEM showed that single BP sheets were readily transformed into large-area and well-connected BP film (Figure 4.5e). The

smooth, uniform and continuous BP films are expected to be beneficial for the ease of processing of the perovskite layer. As a confirmation the nature of the $CsPbBr_3$ polycrystalline film, obtained by a single step spin-coating process, was investigated by SEM. As shown in Figure 4.5f, the perovskite film coated onto PEDOT:PSS exhibited a high density of pin-holes. In contrast, the film directly deposited on the top of the BP interlayer displayed a full coverage with low density of pin-holes, which will considerably reduce current leakage paths in the light-emitting device.[23] Contact angle measurements of dimethyl sulfoxide (DMSO), solvent used for the CsPbBr3 solution, on top of BP and PEDOT:PSS films revealed angles of 16° and 23°, respectively (Figure 4.6). Hence, the full coverage of CsPbBr3 is ascribed to the better wettability of DMSO on the BP film.

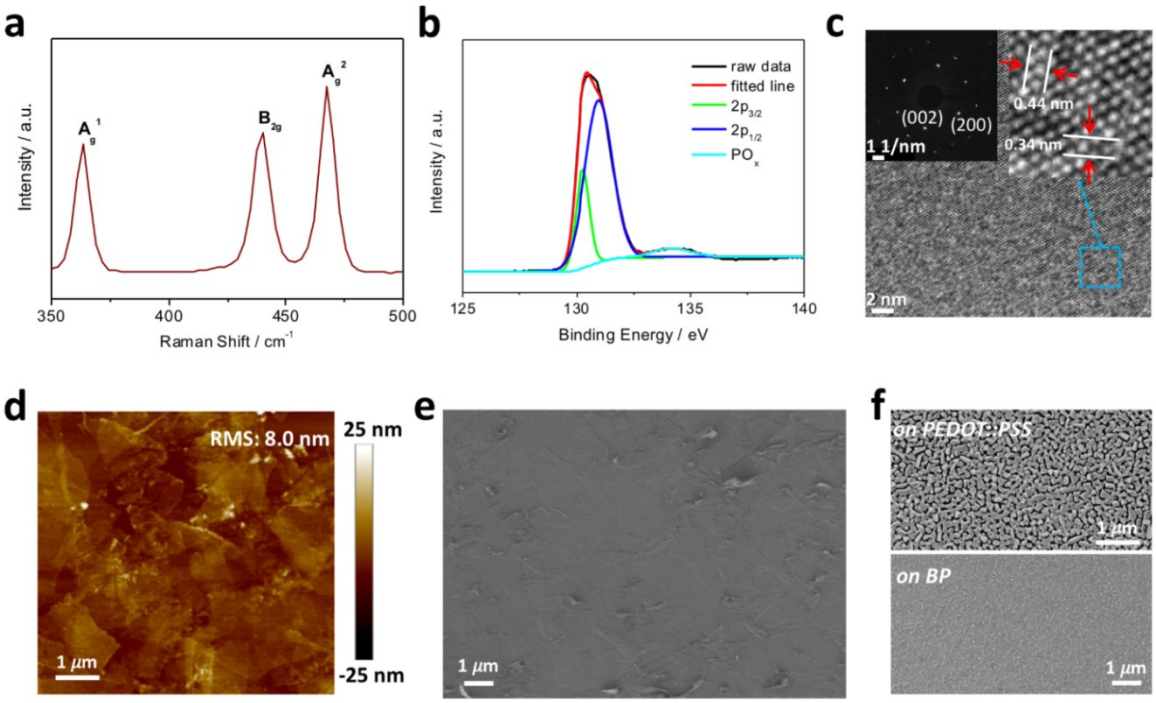

Figure 4.5 a) Raman spectrum and b) high-resolution P2p XPS spectrum of as-fabricated BP film, c) HR-TEM of BP thin flake and the related SAED pattern (inset). d) AFM and e) SEM images of a BP film. f) Morphology comparison by SEM of $CsPbBr_3$ crystalline film on top of PEDOT:PSS (top) and BP (bottom).

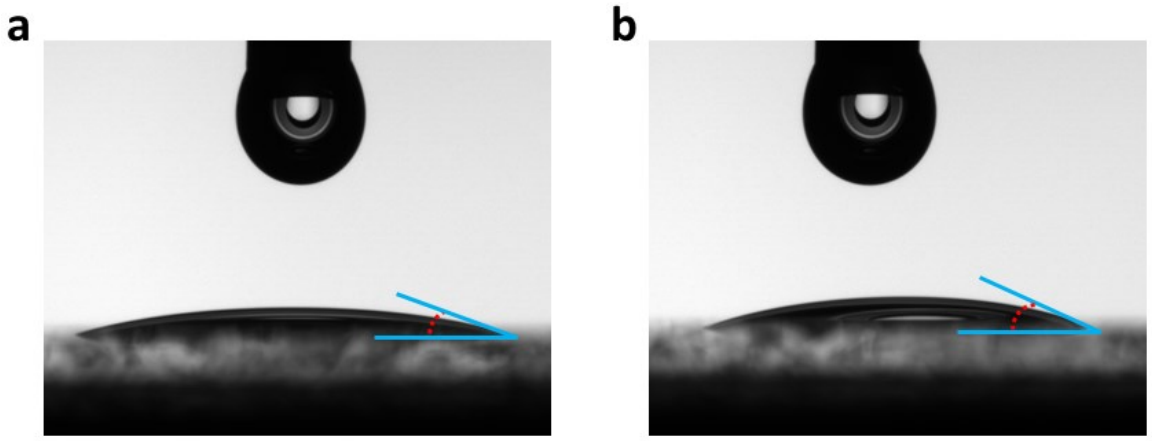

Figure 4.6 Contact angle measurement of a DMSO drop on top of a) BP and b) PEDOT:PSS.

PeLEDs were fabricated on top of a glass/indium tin oxide (ITO) substrate with further configuation PEDOT:PSS/BP/$CsPbBr_3$/1,3,5-tris(1-phenyl-1H-benzimidazol-2-yl)benzene (TPBi)/lithium fluoride (LiF)/aluminum (Al) (Figure 4.7a). The energy band diagram, based on experimental data, is schematically indicated in Figure 4.7b. In such device structure, electrons are transferred from the lowest unoccupied molecular orbital (LUMO) of the hole-blocking/electron transporting material TPBi into the conduction band (CB) of $CsPbBr_3$, while holes are injected from the HOMO of PEDOT:PSS or BP into the VB of $CsPbBr_3$. The radiative recombination between holes and electrons inside the perovskite layer will lead to the emission of green light (Figure 4.7c).

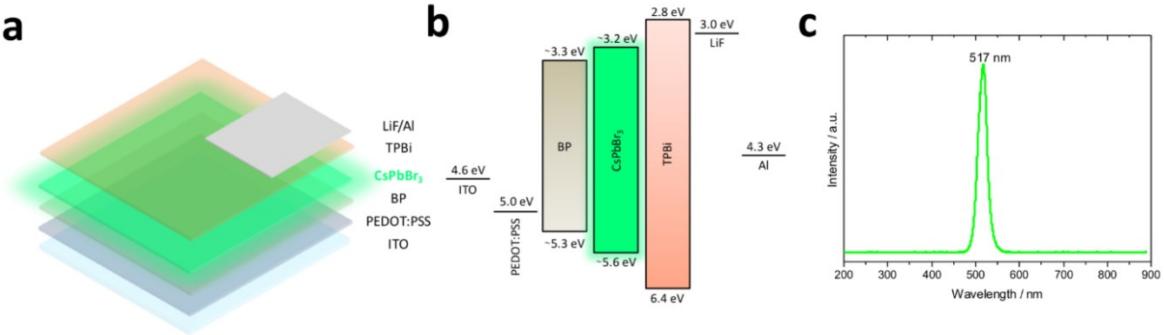

Figure 4.7 a) Schematic illustration of the device architecture and b) the related energy band alignment diagram. c) Electroluminescence spectrum of $CsPbBr_3$ at 6 V.

As demonstrated in Figure 4.8a, the current density-voltage (*J-V*) characteristics of the PeLED without and with BP as HIL are shifted along the voltage axis of 0.3 V, which indicates that the inclusion of BP leads to an enhancement of the built-in voltage as a result of a reduced injection barrier at the anode side. Furthermore, the implementation of BP leads to a significant increase in light output, typically 4.5 times higher than the device without using BP (Figure 4.8b, Table 4.1).

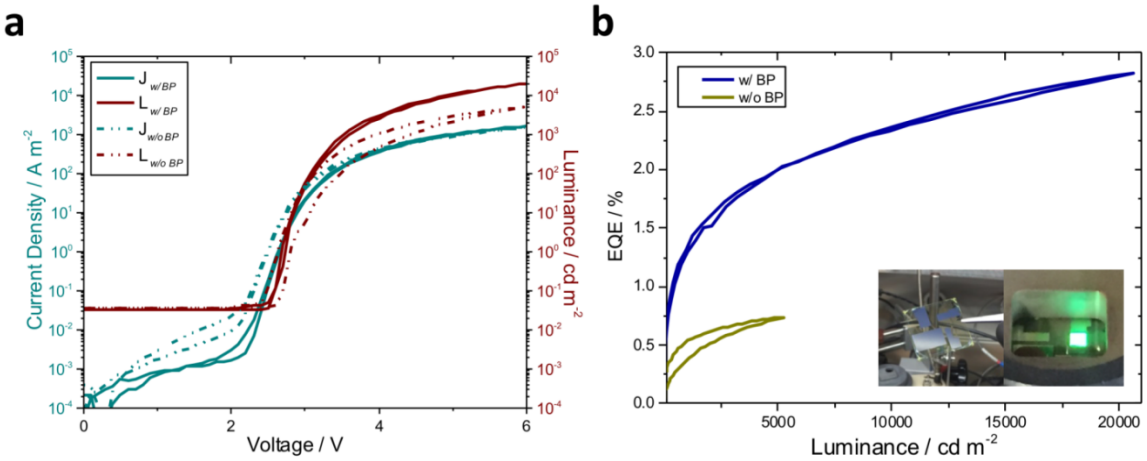

Figure 4.8 a) Current density-voltage-luminance characteristics of PeLEDs with and without BP, b) EQE comparison between PeLEDs with and without BP (the inset show the working BP-incorporated device).

Table 4.1. PeLEDs key parameters for devices without and with BP.

PeLED	$Luminance_{max}$ [cd m^{-2}]	$Luminance_{average}$ [cd m^{-2}]	EQE_{max} [%]	$EQE_{average}$ [%]
w/o BP	5281	5070 ± 187	0.7	0.6 ± 0.1
w/ BP	20636	20041 ± 544	2.8	2.5 ± 0.2

Furthermore, incorporation of BP also enhances the EQE of the PeLED from 0.7 % to 2.8 % (voltage dependence of EQE in Figure 4.9), which is a significant improvement

compared to earlier reported EQEs ranging from 0.008% to 1.37% using polycrystalline $CsPbBr_3$ as emissive layer.

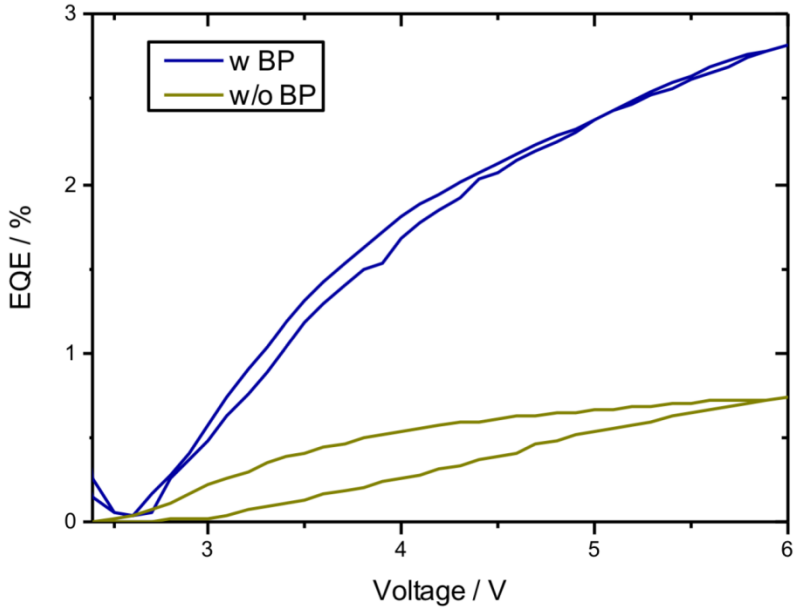

Figure 4.9 Voltage dependence of EQE for the PeLEDs with and without BP.

Moreover, to evaluate the advantages of using high-quality and large area BP flakes, we tested PeLEDs with small and air-exposed BP sheets. Long time sonication of BP dispersion yielded flakes with small lateral size (< 1 μm), which resulted in randomly arranged flakes during film formation. As result of scarce coverage, no apparent improvement for the final device was observed (Figure 4.10a and 4.10b). To deliberately induce degradation, BP was exposed to air throughout the whole film process without the aid of DMF. The reduced quality of BP had a negative impact on the PeLED behavior, which did not emit light (Figures 4.10c and 4.10d).

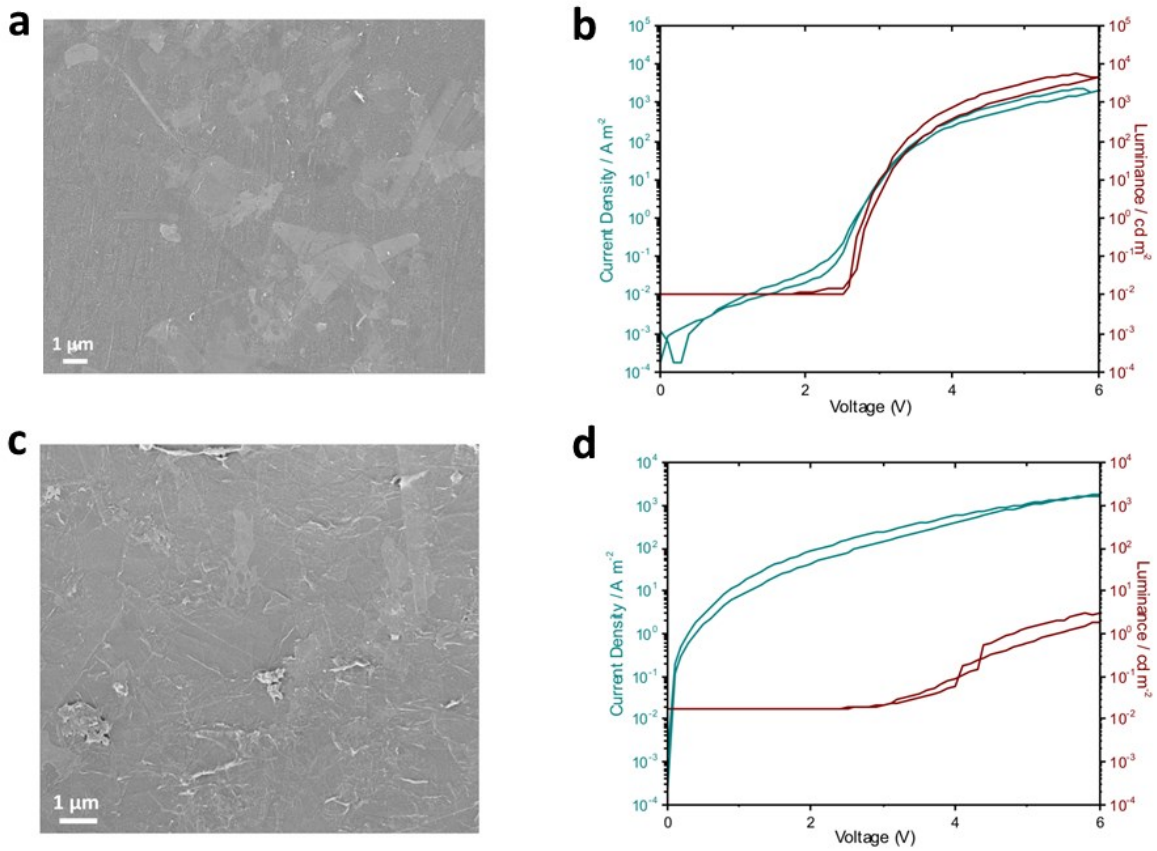

Figure 4.10 a) SEM image of small-size BP flakes randomly coated on top of PEDOT:PSS b) Current density-voltage-luminance characteristics of PeLEDs with few BP sheets. c) SEM image of degraded BP film on top of PEDOT:PSS d) Current density-voltage-luminance characteristics of PeLEDs with degraded BP.

To further quantify the improvement in hole injection upon the use of BP film in $CsPbBr_3$ LEDs, we built hole-only devices. In such a device, the emissive layer is sandwiched between two HILs in order to drive exclusively holes, preventing electron injection. Hence, upon the application of a voltage across the device, the measured current is entirely carried by holes (Figure 4.11).

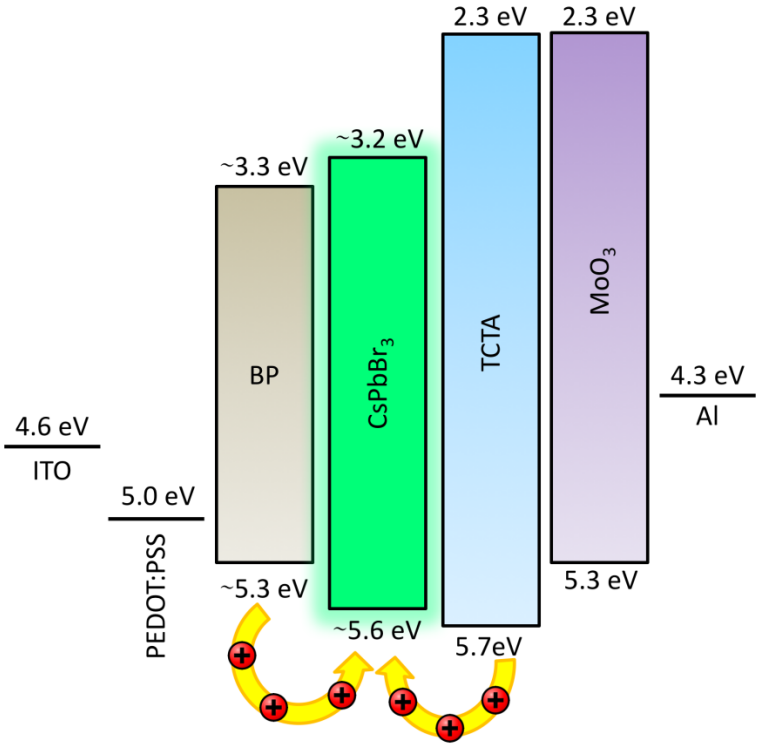

Figure 4.11 Energy band alignment diagram of hole-only device.

The perovskite layer was sandwiched between ITO/PEDOT:PSS/BP and tris(4-carbazoyl-9-ylphenyl)amine (TCTA)/molybdenum oxide (MoO_3). Using a 5 nm TCTA interlayer in combination with MoO_3 leads to the formation of an Ohmic hole contact, even on semiconductors with a deep valence band.[24] At negative bias the holes are injected from the Ohmic TCTA/MoO_3 contact, which enables us to determine hole mobility of $CsPbBr_3$ from the resulting space-charge-limited current (Figure 4.12a).

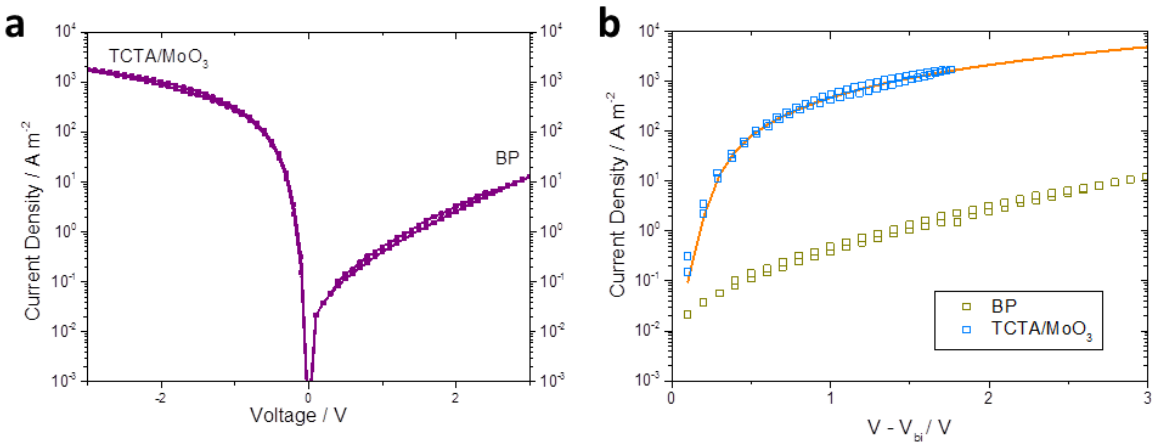

Figure 4.12 a) Current density-voltage characteristics of hole-only devices. Negative bias corresponds to hole injection from MoO_3, positive bias to hole injection from BP b) Current density plotted against voltage (V), corrected for the built-in voltage (V_{bi}). The orange solid line represents the fit with the analytical drift-diffusion model, from which the hole mobility is extracted.

Using a drift-diffusion solver[25], the current injected from the TCTA/MoO_3 electrode could be modeled with a mobility of 8 x 10^{-10} m^2/Vs (Figure 4.12b), using a dielectric constant of 41.[26] Due to the asymmetric work functions of the contacts, a built-in voltage was observed. This built-in voltage could be reproduced in the simulation by using a barrier of 0.4 eV at the counter electrode, which is BP in this case. This gives an indication of the injection barrier for hole injection from the BP electrode. The hole current injected from BP at positive bias is three orders of magnitude lower than the hole current injected from the TCTA/MoO_3 contact at negative bias. The magnitude of an injection-limited current scales with the effective injection barrier φ_b-b according to[27]

$$J_{inj} \propto \exp\left[\frac{-(\varphi_b - b)}{kT}\right], \qquad (1)$$

with k Boltzmann's constant and T the temperature, φ_b the injection barrier and b describing the band bending at an Ohmic contact.[27] For $\varphi_b \leq b$ the current is no longer injection limited and the contact essentially becomes Ohmic. The parameter b was

calculated to be 0.20 eV in this case. From Eq. (1) the three-orders of magnitude difference in injected current compared to the Ohmic counter electrode then equates to an injection barrier φ_b of 0.38 eV. This barrier corresponds well to the barrier of 0.4 eV determined from the numerical simulations. Furthermore, this barrier is within the experimental accuracy of the estimated difference between the reported HOMO of BP (-5.32 eV) and the valence band of $CsPbBr_3$ (-5.6 eV).

Future studies will focus on a further reduction of the hole injection barrier without disruption of the perovskite morphology.

4.3 Conclusion

In summary, we have developed an effective strategy to improve hole injection into perovskite based LEDs using solution-processed high-quality phosphorene. The integration of BP film, constituted of large lateral sized and ultra-thin flakes, into PeLEDs decreases the hole injection barrier and gives rise to uniform growth of the perovskite. This leads to a higher injected hole current and lower leakage current and non-radiative losses, respectively. As a result, the EQE and luminance of the PeLEDs are significantly enhanced. Incorporation of BP to enhance the hole injection from PEDOT:PSS might also be of interest to increase the open-circuit voltage of organic solar cells of which the donor has a deeper HOMO level.

Experimental Session

Delamination of black phosphorus. Black phosphorus (BP) crystals were purchased from Smart Elements (99.998% pure). The delamination process was carried out using a two-electrode system, in which BP crystal and platinum foil were respectively used as cathode and anode. The electrodes were set in parallel with a constant distance of 2.0 cm into a 0.1 M deoxygenated propylene carbonate solution of tetra-n-butyl-ammonium bisulfate ($TBA{\cdot}HSO_4$). A constant potential of -8.0V was applied to trigger the delamination. The whole process was performed into a glove box under inert conditions. Once delamination was completed, the exfoliated BP sheets along with the electrolyte were transferred into sealed conical centrifuge tube. After centrifuged at 3000 rpm for 10 minutes, the electrolyte was discarded and the delaminated BP was washed three times by anhydrous propylene carbonate and isopropyl alcohol (IPA) using centrifuge method (4500 rpm, 10 minutes). Subsequently, BP flakes were dispersed into anhydrous IPA and sonicated for 15 minutes to ensure homogeneity. The as-prepared BP dispersion was centrifuged for the last time at 3000 rpm for 10 minutes to separate out un-exfoliated and thick flakes.

Preparation of BP film. DMF was added into BP dispersion to get a 1:3 DMF:IPA ratio. The dispersion was vacuum-filtered through PTFE membranes with 0.2 μm pore size (Sartorius Stedim Biotech GmbH). BP-coated membranes were transferred on the substrates and subsequently placed under a mechanical press to adhere to the substrates. After 30 min, the membranes were peeled off and BP films dried at 120 ˚C on a heating plate into a glove box.

PeLEDs fabrication. The glass/ITO substrates were cleaned inside a cleanroom facility. Substrates were sequentially washed by detergent, water, acetone and IPA. After drying, ITO substrates underwent to UV-ozone treatment for 20 minutes. An aqueous solution of PEDOT:PSS (Clevios P VP Al4083, Heraeus Precious Metals GmbH & Co.) was spin-coated onto ITO substrates with a two-step procedure (1500 rpm for 10 seconds followed by 4000 rpm for 40 seconds) and annealed at 140 ˚C for 10 minutes. BP film was transferred on the top of PEDOT:PSS through the above mentioned process. $CsPbBr_3$

solutions (11.5 wt%) were obtained by mixing CsBr (99.999% Alfa Aesar) and $PbBr_2$ (99.999%, Puratronic®) as previously reported.[4] Perovskite precursor (CsBr:$PbBr_2$ with molar ratio of 1.5:1) was spin-coated onto PEDOT:PSS and BP at 2000 rpm for 1 minute and then annealed at 90 ˚C for 30 minutes. Afterwards, the devices were transferred into a vacuum chamber for TPBi (40 nm), LiF (1 nm) and Al (100 nm) deposition.

Hole-only device fabrication. TCTA (5 nm), MoO_3 (10 nm) and Al (100 nm) were deposited by vacuum thermal evaporation on the top of ITO/PEDOT:PSS w/ or w/o BP/$CsPbBr_3$ architectures.

Characterization. PeLEDs and hole-only devices were tested with an in-house photodiode and a software controlled source meter (Keithley 2400). AFM measurements were performed on a Digital Instruments Dimension IS. SEM images were obtained using a field-emission scanning electron microscope (Gemini 1530 LEO). TEM and SAED were carried out using a transmission electron microscope (Philips Tecnai F20). XPS analysis was carried out using an AXIS Ultra DLD X-ray photoelectron spectrometer with an Al X-ray source ($h\nu$ = 1486.7 eV). UV-vis and absortion spectra were measured on a Perkin Elmer Lambda 900 spectrometer. Raman spectroscopy measurements were performed with a Bruker RFS 100/S spectrometer (laser wavelength of 633 nm). WF values for ITO, PEDOT:PSS, LiF and Al were measured by Kelvin probe. BP HOMO and CsPbBr3 VB were determined by experimental study on PeLEDs and hole-only devices.

References

[1] a) S. Yakunin, L. Protesescu, F. Krieg, M. I. Bodnarchuk, G. Nedelcu, M. Humer, G. De Luca, M. Fiebig, W. Heiss, M. V. Kovalenko, *Nat. Commun.* **2015**, 6, 8; b) R. J. Sutton, G. E. Eperon, L. Miranda, E. S. Parrott, B. A. Kamino, J. B. Patel, M. T. Horantner, M. B. Johnston, A. A. Haghighirad, D. T. Moore, H. J. Snaith, *Adv. Energy Mater.* **2016**, 6, 6; c) J. Liang, C. Wang, Y. Wang, Z. Xu, Z. Lu, Y. Ma, H. Zhu, Y. Hu, C. Xiao, X. Yi, G. Zhu, H. Lv, L. Ma, T. Chen, Z. Tie, Z. Jin, J. Liu, *J. Am. Chem. Soc.* **2016**, 138, 15829; d) Y. H. He, L. Matei, H. J. Jung, K. M. McCall, M. Chen, C. C. Stoumpos, Z. F. Liu, J. A. Peters, D. Y. Chung, B. W. Wessels, M. R. Wasielewski, V. P. Dravid, A. Burger, M. G. Kanatzidis, *Nat. Commun.* **2018**, 9, 8; e) C. Liu, W. Li, C. Zhang, Y. Ma, J. Fan, Y. Mai, *J. Am. Chem. Soc.* **2018**, 140, 3825.

[2] a) N. Yantara, S. Bhaumik, F. Yan, D. Sabba, H. A. Dewi, N. Mathews, P. P. Boix, H. V. Demir, S. Mhaisalkar, *The Journal of Physical Chemistry Letters* **2015**, 6, 4360; b) P. Z. Liu, W. Chen, W. G. Wang, B. Xu, D. Wu, J. J. Hao, W. Y. Cao, F. Fang, Y. Li, Y. Y. Zeng, R. K. Pan, S. M. Chen, W. Q. Cao, X. W. Sun, K. Wane, *Chemistry of Materials* **2017**, 29, 5168.

[3] a) A. Swarnkar, R. Chulliyil, V. K. Ravi, M. Irfanullah, A. Chowdhury, A. Nag, *Angew. Chem.-Int. Edit.* **2015**, 54, 15424; b) S. A. Veldhuis, P. P. Boix, N. Yantara, M. J. Li, T. C. Sum, N. Mathews, S. G. Mhaisalkar, *Advanced Materials* **2016**, 28, 6804; c) J. Pan, Y. Q. Shang, J. Yin, M. De Bastiani, W. Peng, I. Dursun, L. Sinatra, A. M. El-Zohry, M. N. Hedhili, A. H. Emwas, O. F. Mohammed, Z. J. Ning, O. M. Bakr, *J. Am. Chem. Soc.* **2018**, 140, 562.

[4] H. Cho, C. Wolf, J. S. Kim, H. J. Yun, J. S. Bae, H. Kim, J. M. Heo, S. Ahn, T. W. Lee, *Advanced Materials* **2017**, 29, 8.

[5] a) X. Zhang, H. Lin, H. Huang, C. Reckmeier, Y. Zhang, W. C. H. Choy, A. L. Rogach, *Nano Lett.* **2016**, 16, 1415; b) Y.-H. Kim, C. Wolf, Y.-T. Kim, H. Cho, W. Kwon, S. Do, A. Sadhanala, C. G. Park, S.-W. Rhee, S. H. Im, R. H. Friend, T.-W. Lee, *ACS Nano* **2017**, 11, 6586.

[6] a) G. R. Li, F. W. R. Rivarola, N. Davis, S. Bai, T. C. Jellicoe, F. de la Pena, S. C. Hou, C. Ducati, F. Gao, R. H. Friend, N. C. Greenham, Z. K. Tan, *Advanced Materials* **2016**, 28, 3528; b) J. Pan, L. N. Quan, Y. B. Zhao, W. Peng, B. Murali, S. P. Sarmah, M. J. Yuan, L. Sinatra, N. M. Alyami, J. K. Liu, E. Yassitepe, Z. Y. Yang, O. Voznyy, R. Comin, M. N. Hedhili, O. F. Mohammed, Z. H. Lu, D. H. Kim, E. H. Sargent, O. M. Bakr, *Advanced Materials* **2016**, 28, 8718; c) Y. Ling, Y. Tian, X. Wang, J. C. Wang, J. M. Knox, F. Perez-Orive, Y. Du, L. Tan, K. Hanson, B. Ma, H. Gao, *Advanced Materials* **2016**, 28, 8983.

[7] M. C. Scharber, D. Wuhlbacher, M. Koppe, P. Denk, C. Waldauf, A. J. Heeger, C. L. Brabec, *Advanced Materials* **2006**, 18, 789.

[8] a) M. G. Helander, Z. B. Wang, J. Qiu, M. T. Greiner, D. P. Puzzo, Z. W. Liu, Z. H. Lu, *Science* **2011**, 332, 944; b) Y. H. Kim, H. Cho, J. H. Heo, T. S. Kim, N. Myoung, C. L. Lee, S. H. Im, T. W. Lee, *Advanced Materials* **2015**, 27, 1248.

[9] J. G. Simmons, *Phys. Rev. Lett.* **1965**, 15, 967.

[10] H. Wu, Y. Zhang, M. Lu, X. Zhang, C. Sun, T. Zhang, V. L. Colvin, W. W. Yu, *Nanoscale* **2018**, 10, 4173.

[11] a) S.-S. Li, K.-H. Tu, C.-C. Lin, C.-W. Chen, M. Chhowalla, *ACS Nano* **2010**, 4, 3169; b) X. Gu, W. Cui, H. Li, Z. W. Wu, Z. Y. Zeng, S. T. Lee, H. Zhang, B. Q. Sun, *Adv. Energy Mater.* **2013**, 3, 1262; c) J. J. Intemann, K. Yao, Y.-X. Li, H.-L. Yip, Y.-X. Xu, P.-W. Liang, C.-C. Chueh, F.-Z. Ding, X. Yang, X. Li, Y. Chen, A. K. Y. Jen, *Advanced Functional Materials* **2014**, 24, 1465; d) G. J. Choi, Q. V. Le, K. S. Choi, K. C. Kwon, H. W. Jang, J. S. Gwag, S. Y. Kim, *Advanced Materials* **2017**, 29, 8.

[12] L. K. Li, Y. J. Yu, G. J. Ye, Q. Q. Ge, X. D. Ou, H. Wu, D. L. Feng, X. H. Chen, Y. B. Zhang, *Nature Nanotechnology* **2014**, 9, 372.

[13] a) Z. Luo, J. Maassen, Y. Deng, Y. Du, R. P. Garrelts, M. S. Lundstrom, P. D. Ye, X. Xu, *Nat. Commun.* **2015**, 6; b) X. M. Wang, A. M. Jones, K. L. Seyler, V. Tran, Y. C. Jia, H. Zhao, H. Wang, L. Yang, X. D. Xu, F. N. Xia, *Nature Nanotechnology* **2015**, 10, 517.

[14] S. H. Liu, S. H. Lin, P. You, C. Surya, S. P. Lau, F. Yan, *Angew. Chem.-Int. Edit.* **2017**, 56, 13717.

[15] a) S. H. Lin, S. H. Liu, Z. B. Yang, Y. Y. Li, T. W. Ng, Z. Q. Xu, Q. L. Bao, J. H. Hao, C. S. Lee, C. Surya, F. Yan, S. P. Lau, *Advanced Functional Materials* **2016**, 26, 864; b) W. Chen, K. Li, Y. Wang, X. Feng, Z. Liao, Q. Su, X. Lin, Z. He, *The Journal of Physical Chemistry Letters* **2017**, 8, 591.

[16] M. Batmunkh, M. Bat-Erdene, J. G. Shapter, *Adv. Energy Mater.* **2018**, 8.

[17] S. Yang, K. Zhang, A. G. Ricciardulli, P. P. Zhang, Z. Q. Liao, M. R. Lohe, E. Zschech, P. W. M. Blom, W. Pisula, K. Mullen, X. L. Feng, *Angew. Chem.-Int. Edit.* **2018**, 57, 4677.

[18] D. Hanlon, C. Backes, E. Doherty, C. S. Cucinotta, N. C. Berner, C. Boland, K. Lee, A. Harvey, P. Lynch, Z. Gholamvand, S. Zhang, K. Wang, G. Moynihan, A. Pokle, Q. M. Ramasse, N. McEvoy, W. J. Blau, J. Wang, G. Abellan, F. Hauke, A. Hirsch, S. Sanvito, D. D. O'Regan, G. S. Duesberg, V. Nicolosi, J. N. Coleman, *Nat. Commun.* **2015**, 6.

[19] D. Hanlon, C. Backes, E. Doherty, C. S. Cucinotta, N. C. Berner, C. Boland, K. Lee, A. Harvey, P. Lynch, Z. Gholamvand, S. Zhang, K. Wang, G. Moynihan, A. Pokle, Q. M. Ramasse, N. McEvoy, W. J. Blau, J. Wang, G. Abellan, F. Hauke, A. Hirsch, S. Sanvito, D. D. O'Regan, G. S. Duesberg, V. Nicolosi, J. N. Coleman, *Nat. Commun.* **2015**, 6, 8563.

[20] H. B. Ribeiro, C. E. P. Villegas, D. A. Bahamon, D. Muraca, A. H. C. Neto, E. A. T. de Souza, A. R. Rocha, M. A. Pimenta, C. J. S. de Matos, *Nat. Commun.* **2016**, 7.

[21] A. Favron, F. A. Goudreault, V. Gosselin, J. Groulx, M. Côté, R. Leonelli, J.-F. Germain, A.-L. Phaneuf-L'Heureux, S. Francoeur, R. Martel, *Nano Lett.* **2018**, 18, 1018.

[22] J. D. Wood, S. A. Wells, D. Jariwala, K.-S. Chen, E. Cho, V. K. Sangwan, X. Liu, L. J. Lauhon, T. J. Marks, M. C. Hersam, *Nano Lett.* **2014**, 14, 6964.

[23] a) W. Zhang, M. Saliba, D. T. Moore, S. K. Pathak, M. T. Horantner, T. Stergiopoulos, S. D. Stranks, G. E. Eperon, J. A. Alexander-Webber, A. Abate, A. Sadhanala, S. H. Yao, Y. L. Chen, R. H. Friend, L. A. Estroff, U. Wiesner, H. J. Snaith,

Nat. Commun. **2015**, 6, 10; b) Q. A. Akkerman, M. Gandini, F. Di Stasio, P. Rastogi, F. Palazon, G. Bertoni, J. M. Ball, M. Prato, A. Petrozza, L. Manna, *Nat. Energy* **2017**, 2, 7.

[24] N. B. Kotadiya, H. Lu, A. Mondal, Y. Ie, D. Andrienko, P. W. M. Blom, G. Wetzelaer, *Nat. Mater.* **2018**, 17, 329.

[25] L. J. A. Koster, E. C. P. Smits, V. D. Mihailetchi, P. W. M. Blom, *Phys. Rev. B* **2005**, 72, 9.

[26] Y. Rakita, N. Kedem, S. Gupta, A. Sadhanala, V. Kalchenko, M. L. Bohm, M. Kulbak, R. H. Friend, D. Cahen, G. Hodes, *Cryst. Growth Des.* **2016**, 16, 5717.

[27] P. de Bruyn, A. H. P. van Rest, G. A. H. Wetzelaer, D. M. de Leeuw, P. W. M. Blom, *Phys. Rev. Lett.* **2013**, 111, 5.

Chapter 5 Conclusion and Outlook

5.1 Conclusion

In short, this thesis focuses on the application of solution-processed 2D materials into emerging optoelectronic devices, graphene as transparent conductive electrode and phosphorene as hole injection layer.

ITO has been widely used as transparent electrode in optoelectronics because of its high optical transparency and remarkable electrical conductivity. However, high production costs, dwindling supplies and poor mechanical flexibility strongly hinder its practical use. To date, despite significant research progress on alternative TCEs has been achieved using 1D materials, 2D materials and polymers, a transparent conductor able to replace commercial ITO is still missing.

Electrochemical exfoliation of graphite enables production of thin layered EG with excellent solution-processability, large lateral dimensions, and remarkable electronic properties. In Chapter 2, EG was successfully coated on top of both rigid and flexible large-area substrates (A4 size), quartz and PEN, respectively, through spray coating. Spray coating was selected over several deposition techniques because of its versatility, ease of processing and potential for scaled-up production. Uniform and mechanically stable EG films with low surface roughness (~2 nm) exhibited the lowest R_s values among all the solution-processed graphene-based TCEs, which are in the range of 0.52 kΩ sq^{-1} at 70 T% to 0.18 kΩ sq^{-1} at 55 T%. To determine the most performant TCE, we carried out an analysis on the *J-V* characteristics of OPV devices with different EG film transparencies. Devices were constrained by the trade-off between transparency and series resistance. The best PTB7:$PC_{71}BM$ OSC based on EG (65 T%) exhibited a PCE that is 40% lower than its ITO analogues. This gap is due to the low conductivity at high transmittance values of EG film.

As described in Chapter 3, to increase the conductivity without sacrificing the transmittance of our films, AgNWs were introduced in the 2D system. Despite low R_s and high transparency of bare AgNWs TCEs, the rough surface of the network (RMS = 16.4

nm) and the NWs sticking out of the plane systematically caused electrical shorts when integrated into the OSCs. The application of EG through spray-coating led to reduction of RMS (4.6 nm). Indeed, large EG flakes completely covered the AgNWs junctions and holes between the NWs. Moreover, the conductivity of the AgNWs network was improved. In particular, the most relevant R_s reduction, from 78 to 13.7 Ω sq^{-1}, was achieved for the 89 T% TCE. These values are in line with the typical ones of commercial ITO. As additional benefits, the continuous EG layer improved the mechanical flexibility and oxygen degradation resistance of the AgNWs network. To evaluate the performances of our hybrid TCEs, we implemented the hybrid film in both rigid and flexible organic optoelectronic devices (OSCs and PLEDs). The devices built on our solution-processed TCEs exhibited performances similar to their commercial ITO-based counterparts. The synergy of AgNWs and EG led to an electrode endowed with all the features required by the next-generation TCEs: cost-effectiveness, high conductivity, high transparency, durability and mechanical flexibility.

In Chapter 4, we discussed the problem of large hole injection barriers in emerging LEDs based on perovskite. Inorganic perovskite semiconductors, like the green-emitting $CsPbBr_3$, have a VB located at 5.6 eV below vacuum. PEDOT:PSS, which is the conventional HIL in PeLEDs, has a WF of 5.0 eV. Thus, typical CsPbBr3-based LEDs suffer from large hole injection barriers driven by the huge mismatch between the WF of PEDOT:PSS and VB of $CsPbBr_3$ (~0.6 eV). Moreover, PEDOT:PSS does not constitute a suitable stage for a proper growth of $CsPbBr_3$ crystals. As result, PeLEDs are governed by shunt paths in uneven and discontinuous perovskite films. To overcome both limitations, we used a solution-processed approach by including a BP layer between PEDOT:PSS and $CsPbBr_3$. BP is a 2D material with high charge-carrier mobility that features a thickness-dependent bandgap. For instance, thin-layered BP has a reported HOMO level of 5.32, which would lower the injection barrier by 0.3 eV. Electrochemical-exfoliated BP was implemented on top of PEDOT:PSS by suction filtration. The choice of this technique relied on the ability to preserve the morphology and electrical properties of BP, which easily degrades with moisture. To estimate the improvement by using BP, we analyzed PeLEDs with and without BP. First, the polycrystalline $CsPbBr_3$ film directly deposited on the top of the BP interlayer showed a uniform coating with low density of pin-holes. Second, the inclusion of BP led to significant increase of both EQE and light output, over 4 times higher than devices with PEDOT:PSS only. Device analysis indicated that

integration of BP enhanced the built-in voltage as a result of a reduced injection barrier at the anode side. The results of this study might be of relevance also in the field of organic optoelectronic devices where donors have deep HOMO level.

5.2 Outlook

The majority of organic and perovskite optoelectronic devices rely on low costs and properties tailoring of abundant materials to switch from emerging to well-established technology. The studies present in this thesis constitute a step forward in cost-effective and solution-processed materials for emerging optoelectronics. However, further efforts towards higher performance of the materials, through the improvement of synthetic methods, and large-scale production should be carried out in future. To enhance the efficacy of 2D films, optimization of electrochemical exfoliation is necessary. 2D sheets with larger size and uniform thickness distribution would generate more stable and efficient electrical and morphological properties. Further improvements involve the use of patterning techniques for increasing the transmittance of the films. Moreover, surface functionalization with other species can be used to tailor the properties of the materials. From a device fabrication point of view, deeper investigation of suitable large-scale production methods, such as ink-jet and roll-to-roll printing, and the related ink formulations can be performed.

List of Publications

1. **A. G. Ricciardulli**, S. Yang, N. B. Kotadiya, G. A. H. Wetzelaer, X. Feng, P. W. M. Blom*, Improved Hole Injection into Perovskite Light-Emitting Diode Using A Black Phosphorus Interlayer, *submitted*.

2. **A. G. Ricciardulli**, S. Yang, G. A. H. Wetzelaer, X. Feng, P. W. M. Blom*, Hybrid Silver Nanowire and Graphene based Solution-processed Transparent Electrode for Organic Optoelectronics *Adv. Funct. Mater.*, **2018**, 28, 1706010.

3. **A. G. Ricciardulli,** S.Yang, X. Feng, P. W. M. Blom*, Solution-Processable High-Quality Graphene for Organic Solar Cells, *ACS Appl. Mater. Interfaces* **2017**, 9, 25412.

4. S. Yang, P. Zhang, F. Wang, **A. G. Ricciardulli** , M. Lohe, P. W. M. Blom, X. Feng*, Fluoride-Free Synthesis of Two-Dimensional Titanium Carbide (MXene) Using A Binary Aqueous System, *Angew. Chem. Int. Ed.*, **2018**, *accepted for publication*.

5. S. Yang**,** K. Zhang, **A. G. Ricciardulli**, P. Zhang, Z. Liao, M. Lohe, E. Zschech, W. Pisula, P. W. M. Blom, K. Müllen,* X. Feng*, A Delamination Strategy for Thinly Layered Defect-Free High-Mobility Black Phosphorus Flakes, *Angew. Chem. Int. Ed.*, **2018**, 57, 4677. (VIP paper)

6. S. Yang, **A. G. Ricciardulli**, S. Liu, R. Dong, M. R. Lohe, A. Becker, M.A. Squillaci, P. Samorì, K. Müllen,* X. Feng,*, Ultrafast Delamination of Graphite into High-quality Graphene using Alternating Currents, *Angew. Chem. Int. Ed.*, **2017**, 56, 1. (Hot paper)

7. S. Yang, **A. G. Ricciardulli**, S. Liu, R. Dong, M. R. Lohe, A. Becker, M.A. Squillaci, P. Samorì, K. Müllen,* X. Feng*, Ultraschnelle Schichtablösung von Graphit zu qualitativ hochwertigem Graphen durch Nutzung von Wechselstrom, *Angew. Chem.*, **2017**, 1, 6669. (Hot paper)

8. S. Solak, **A. G. Ricciardulli**, T. Lenz, N. I. Crăciun, P. W. M. Blom, G. A. H. Wetzelaer*, Open-circuit voltage loss in annealed P3HT:perylene diimide bulk heterojunction solar cells, *Appl. Phys. Lett.*, **2017**, 110, 163301.

9. A. Keerthi, C. An, M. Li, T. Marszalek, **A. G. Ricciardulli**, B. Radha, F. D. Alsewailem, K. Müllen,* M. Baumgarten*, Dithieno[2,3-*d*;2′,3′-*d*]benzo[2,1-*b*;3,4-

b']dithiophene: a novel building-block for a planar copolymer, *Polym. Chem.*, **2016**, 7, 1545.

10. C. Tedesco, A. Meli, E. Macedi, V. Iuliano, **A. G. Ricciardulli**, F. De Riccardis, G. B. M. Vaughan, V. J. Smith, L. J. Barbour, I. Izzo*, Ring size effect on the solid state assembly of propargyl substituted hexa- and octacyclic peptoids, *Cryst. Eng. Comm.*, **2016**, 18, 8838. (and Cover)

Acknowledgment

I am profoundly grateful to Prof. Dr. [redacted] for his everlasting support, continuous guidance and sharing his immense wisdom. His passion and perspective inspired me throughout my research path. I would also like to thank him for the kindness, friendliness and the efforts spent to let my research blossom. I am very glad to have him as supervisor. If I have to take a snap-shot of this journey, I would choose the friendly discussion we had while eating *Chi-Bee* in Busan, during the ICSM 2018 Conference.

My sincere thanks to Prof. Dr. [redacted] (Johannes Gutenberg University Mainz) for supporting and appraising my work.

I would like to thank Dr. [redacted] for sharing fruitful ideas, helping, trusting my capabilities and having fun in the laboratory during the toughest periods. However, it would have been better if he did not wake me up early in the morning to push me to hardly work every day (even when I was on vacation)!

My acknowledgement also extends to my colleagues in the group of Prof. [redacted] at the Max Planck Institute for Polymer Research (MPI-P). I truly appreciate Dr. [redacted] (MPI-P) for the fruitful discussions and considerable help. I would also like to thank [redacted] (MPI-P) for the kind help in introducing me to the use of some devices and instrumentation. [redacted] (MPI-P) taught me how to manage SEM and spent time in kind discussions on a wide variety of topics. [redacted] (MPI-P) and [redacted] (MPI-P) provided me good guidance on how to operate AFM. [redacted] (MPI-P) carried out HR-TEM for many samples. [redacted] (MPI-P) was always warm-hearted and helpful with all kind of issues.

I thank Prof. Dr. [redacted] (Technische Universität Dresden, TUD) for his collaboration and [redacted] (TUD) for the quick adhesion measurements.

In addition, I want to express my appreciations to all the technicians in the group of Prof. [redacted] at MPI-P for their considerable technical support.

At last, special thanks are dedicated to my parents, wife and sister for their everlasting trust, support and unconditional love. Moreover, I would like to extend my gratitude to my grandparents for teaching me the important values and feeding me with love.

[redacted]